Abstract

First Principles Studies of Photoelasticity and Two-dimensional Silica

Xin Liang

2020

The thesis presents theoretical studies of photoelasticity and Two-dimensional silica using first principles calculations. The first project in this thesis concerns the elasto-optic effect in solids. The elasto-optic effect, or photoelasticity, describes the linear change of dielectric constant with applied strain and is a universal material property for insulators and semiconductors. Though the elasto-optic responses can be directly computed using first principles (e.g., density functional perturbation theory), little insight into the governing microscopic physical principles is provided by these methods. In this work, we describe a microscopic first principles analysis of photoelasticity in real-space based on Maximally Localized Wannier Functions (MLWFs). We show that the strain-dependent change of dipole transitions between occupied and unoccupied Wannier functions is the main determinant of photoelasticity. By organizing the dipole transitions into spatially localized shells according to the distances, we find that the photoelasticity is a relatively long-ranged. We believe the long-ranged nature of photoelasticity makes it unlikely to find simple and localized models with very few parameters that can describe photoelasticity with sufficient accuracy. The second project in this thesis investigates the growth of 2D silica and silicate thin films on $\mathrm{Ni}_x\mathrm{Pd}_{1-x}(111)$ alloy substrates. In the past decade, the creation of 2D SiO_2 has added a new member to the material class of two-dimensional (2D) Van der Waals (vdW) atomically thin sheet. 2D SiO_2 is the thinnest form of silica known with the SiO_2 stoichiometry. Apart from being a 2D material, 2D SiO_2 is also of interest because of its structural similarities to zeolite catalysts. 2D bilayer SiO_2 can serve as a model system that imitates the interior surface of bulk zeolites while its 2D nature permits application of surface microscopy techniques that reach atomic scale resolution. We employ density functional theory (DFT) to study the 2D SiO_2 on various metal substrates and demonstrate that epitaxial strain

plays an important role in engineering the 2D SiO_2 overlayer's struture. We also focus on the structural competition between crystalline hexagonal 2D SiO_2 in commensurate and incommensurate relation to the substrate when epitaxial strain cannot be realized in experiments. The recent creation of Ni_xPd_{1-x} random alloy in experiments is intended to study the strain effect on the morphology of the 2D SiO_2 overlayer through the alloy's tunable lattice constant. However, the application is hindered due to its ability to form silicate overlayer through chemical reaction with the deposited SiO_2. We propose a thermodynamically stable Ni silicate structure as a theoretical model for the silicate thin film on the $Ni_xPd_{1-x}(111)$ surface and use DFT to characterize its structural and electronic properties. The next thrust in this effort has been to understand the phase competition between 2D silica and silicate phases on Ni_xPd_{1-x} alloy substrate. First principles calculations suggest that by decreasing the oxygen pressure and increasing Si supply, the 2D SiO_2 will become the favorable phase. Experiments show that a decreased oxygen and restricted annealing temperature and time enable the growth of 2D SiO_2.

First Principles Studies of Photoelasticity and Two-dimensional Silica

A Dissertation
Presented to the Faculty of the Graduate School
of
Yale University
in Candidacy for the Degree of
Doctor of Philosophy

by
Xin Liang

Dissertation Director: Sohrab Ismail-Beigi

December, 2019

Contents

Acknowledgment **xxii**

1 Introduction **1**

2 Methods **5**

2.1 Density functional theory 5

2.1.1 Hohenberg-Kohn Theorems and Kohn-Sham equations 6

2.1.2 Exchange-correlation energy functional 9

2.1.3 Planewave basis and pseudopotentials 10

2.1.4 Hellman-Feynman theorem 11

2.2 Density functional perturbation theory 13

2.3 Maximally Localized Wannier Functions 16

2.4 Van der Waals corrections 20

3 Degree of locality of elasto-optic response in solids **22**

3.1 Introduction 22

3.2 Physical insight and bond-orbital models 25

3.3 Computational Methods 26

3.4 DFPT 30

3.5 Silicon 32

3.5.1 RPA 32

3.5.2 Wannier analysis & unexpected convergence behavior 35

3.6 Diamond 42

3.7 NaCl 47

3.8 MgO 54

3.9 Summary and Outlook 59

3.10 Appendix 61

4 First principles description of 2D SiO_2 on metal substrates 63

4.1 Introduction 63

4.2 Methods 65

4.3 Results and Discussions 68

  4.3.1 Hexagonal bilayer silica on various metal substrates 68

  4.3.2 Epitaxially strained 2D bilayer SiO_2 in different morphologies on Ru 69

  4.3.3 Approximate description of incommensurate binding 72

  4.3.4 The role of chemisorbed oxygen atoms 75

4.4 Conclusions and outlook 80

5 Structure of a two-dimensional silicate layer formed by reaction with an alloy substrate 82

5.1 Introduction 82

5.2 Methods 84

  5.2.1 Experimental 84

  5.2.2 Computational 86

5.3 Results 87

  5.3.1 Experimental 87

  5.3.2 Computational 94

5.4 Discussion 105

6 Tuning two-dimensional silica and silicate growth on $Ni_xPd_{1-x}(111)$ alloy substrates through epitaxial strain and growth conditions 107

6.1 Introduction 107

6.2 Experimental Method 111

6.3 Computational Method 112

6.3.1 First-principles atomistic thermodynamics 112
6.3.2 Chemical potentials 113
6.4 Experimental results 114
6.4.1 Impact of growth conditions 114
6.4.2 Strain effects on 2D Ni silicate formation 120
6.5 Computational results 124
6.5.1 Competition between 2D silica and silicate phases on Ni-Pd(111) . . 124
6.5.2 The phase diagram 125
6.6 Discussion 127
6.7 Summary 131

7 Outlook **133**

7.1 Photoelastic responses in solids 133
7.2 2D SiO_2 on metal substrates 134
7.3 2D Ni Silicate on the Ni_xPd_{1-x} alloy substrate 135

List of Figures

1.1 A schematic plot showing the process of SiO_2 layer deposited on Ni_xPd_{1-x} alloy surface reacts to the substrate to form Ni silicate thin film. 3

3.1 Cumulative sum of $D(\mathbf{k})$ and $\Delta D(\mathbf{k})$ with 1.0% uniaxial strain along x-axis in bulk Si. The horizontal axis is the fraction of k-points in the total $12 \times 12 \times 12 = 1728$ k-point mesh. In the upper plot of the cumulative sum of $D(\mathbf{k})$, the k-points are sorted by magnitude of $D(\mathbf{k})$ in decreasing order; in the lower plot of the cumulative sum of $\Delta D(\mathbf{k})$, which is the change in $D(\mathbf{k})$ due to the imposed 1.0% strain along x-axis, the k-points are sorted by magnitude of $\Delta D(\mathbf{k})$ in decreasing order. 33

3.2 Wannier functions in bulk Si: (a) bonding and (b) antibonding. Red and blue correspond to positive and negative value in these isosurface plots, respectively. These isosurface plots demonstrate that the bonding and antibonding Maximally Localized Wannier functions are localized in real-space about the center of a Si-Si bond. 35

3.3 Band structure of bulk Si. Black solid lines are the DFT-LDA bands; red dashed lines are the Wannier interpolated bands. Since the frozen window [27] ranges from below the valence band to a few eV above the Fermi energy, the valence and low-lying conduction bands are reproduced exactly; as shown in the text, the differences at higher energies only lead to small errors in the computed dielectric response in the Wannier basis. 36

3.4 Magnitude of the Wannier dipole matrix elements $|M|$ (Eq. 3.5) versus distance between Wannier functions. Wave vector $\mathbf{q}$ is aligned with x-axis. The distance is between the center of $W_{b,\mathbf{0}}$ (the bonding Wannier function in the home unit cell) and $W_{a,\mathbf{R}}$ (the antibonding Wannier function $\mathbf{R}$ lattice vectors away). For reference, the bond length between nearest-neighbor Si atoms is 2.35 Å. The two sets of results are for Wannier functions generated in two different supercells. 40

3.5 Convergence of ϵ_{xx} and $\Delta\epsilon_{xx}$ with 1.0% uniaxial strain along x-axis in bulk Si using the Wannier function method. 41

3.6 The three shells of dipole transitions with the largest matrix elements in Wannier basis visualized in real space. Arrows are drawn from a bonding Wannier function (the initial state) to an antibonding Wannier function (the final state) of the dipole transition matrix elements. Given that the initial state is the bonding Wannier function on bond “1”, the arrow “1” → “1” illustrates the dipole transitions to the same bond (there is only one such type of transition per chemical bond), the arrow “1” → “2” illustrates the dipole transitions to the nearest-neighbor bonds (there are six such transitions per chemical bond), and the arrow “1” → “3” illustrates the dipole transitions to the second nearest-neighbor bonds that are parallel to bond “1” (there are six such transitions per chemical bond). 43

3.7 Band structure of bulk diamond. Black solid lines are the DFT-LDA bands; red dashed lines are the Wannier interpolated bands. Both of the 4 valence and 4 lowest conduction bands form an isolated group of bands. 44

3.8 Magnitude of the bulk diamond Wannier dipole matrix elements $|M|$ (Eq. 3.5) versus distance between Wannier functions. Wave vector $\mathbf{q}$ is aligned with x-axis. The distance is between the center of $W_{b,\mathbf{0}}$ (the bonding Wannier function in the home unit cell) and $W_{a,\mathbf{R}}$ (the antibonding Wannier function $\mathbf{R}$ lattice vectors away). For reference, the bond length between nearest-neighbor C atoms is 1.55 Å. The two sets of results are for Wannier functions generated in two different supercells. 46

3.9 Convergence of ϵ_{xx} and $\Delta\epsilon_{xx}$ with 1.0% uniaxial strain along x-axis in bulk diamond using the Wannier function method. The figure adopts the same notation as Figure 3.5. 47

3.10 Wannier functions in NaCl: occupied Wannier functions (a) Cl s orbital and (b) one of Cl p orbitals, unoccupied Wannier functions (c) Na s orbital, (d) one of Na p orbitals, (e) one of Cl d orbitals. Red and blue correspond to positive and negative value in these isosurface plots, respectively. These plots illustrate the atomic centered Maximally Localized Wannier Functions. Color scheme of the atoms: Na: cyan, Cl: green. 49

3.11 Band structure of bulk rocksalt NaCl. Black solid lines are the DFT-LDA bands; red dashed lines are the Wannier interpolated bands. The valence Wannier bands are spanned by sp-like Wannier functions centered on Cl. The conduction Wannier bands are spanned by sp-like Wannier functions centered on Na and d-like Wannier functions centered on Cl. 50

3.12 Magnitude of the bulk NaCl Wannier dipole matrix elements $|M|$ versus distance between Wannier functions. The notations are the same as Figure. 3.4. For reference, the distance between the nearest Na and Cl atoms is 2.82 Å. 52

3.13 Convergence of ϵ_{xx} and $\Delta\epsilon_{xx}$ with 1.0% uniaxial strain along x-axis in bulk NaCl using the Wannier function method. The figure uses the same notations as Figure 3.5. 53

3.14 The three shells of dipole transitions in bulk NaCl with the largest matrix elements in the Wannier basis visualized in real space. Color scheme of the atoms: Na: cyan, Cl: green. Similar to Figure. 3.6, arrows are drawn from the centers of the occupied Wannier function (initial state on Cl) to the centers of the unoccupied Wannier functions (final state on either Cl or Na) of the dipole transition. Each individual atomic site corresponds to multiple occupied and unoccupied Wannier functions in NaCl (unlike in bulk Si and diamond where each chemical bond accommodates a unique pair of bonding and antibonding Wannier functions). With an initial occupied Wannier function on Cl atom "1", the arrow "1" → "1" illustrates the dipole transitions to the same atom (from the *sp* states to the *d* states of the same Cl atom), "1" → "2" illustrates the dipole transitions to the nearest-neighbor Na atoms (from the *sp* states of Cl to the *sp* states of the neighboring Na atoms), and "1" → "3" illustrates the dipole transitions to the second nearest-neighbor Cl atoms (from the *sp* states of Cl to the *d* states of its second nearest-neighbor Cl atoms). 55

3.15 Band structure of bulk rocksalt MgO. Black solid lines are the DFT-LDA bands; red dashed lines are the Wannier interpolated bands. The valence Wannier bands are spanned by *sp*-like Wannier functions centered on O. The conduction Wannier bands are spanned by *sp*-like Wannier functions centered on Mg and *d*-like Wannier functions centered on O. 56

3.16 Magnitude of the bulk MgO Wannier dipole matrix elements $|M|$ versus distance between Wannier functions. The notations are the same as Figure. 3.4. For reference, the distance between the nearest Mg and O atoms is 2.11 Å. 58

3.17 Convergence of ϵ_{xx} and $\Delta\epsilon_{xx}$ with 1.0% uniaxial strain along x-axis in bulk MgO using the Wannier function method. The figure uses the same notations as Figure 3.5. 59

4.1 Side and top views of the hexagonal bilayer SiO_2 on metal substrates. Color scheme: Si cyan, O red, M grey (M is the metal atom in the substrate). (a) side view of the bilayer SiO_2 on a metal substrate; (b) top view of the bilayer SiO_2 in registry 1 with the surface: every O atom is above a metal atom; (c) top view of the bilayer SiO_2 in registry 2 with the surface: every O atom is above a hollow site. 69

4.2 Energy difference between 2D SiO_2 in 8-6-4 structure and hexagonal structure. (a) top view of 2D hexagonal SiO_2 on Ru(0001); (b) top view of 2D 8-6-4 SiO_2 on Ru(0001); (c) energy difference between SiO_2 in 8-6-4 and hexagonal structures computed from first principles on Ru(0001) with three different vdW corrections. 71

4.3 Schematic of commensurate (left) and incommensurate (right) lattices in one dimension. Yellow squares represent the substrate's atoms and green circles represent the overlayer's atoms. Rad dashed rectangles describe the substrate unit cell. Black dashed lines indicate binding bewteen overlayer and substrate with vertical lines corresponding to optimal binding. 73

4.4 Structure of the 2D bilayer SiO_2 on "oxygen-rich" metal substrates with 1 O per (2 × 2) unit cell. Color scheme: Si cyan, O red, M grey (M is the metal atom in the substrate). (a) Top view of the 2D SiO_2 in registry 1 with the surface; (b) top view of the 2D SiO_2 in registry 2 with the surface. The positions of the chemisorbed oxygen are marked by the arrow. The registry 1 and 2 refer the same relative alignment of the thin film to the substrate as in Figure 4.1. 77

5.1 (a) Auger electron spectra recorded for: (i) bare Ni-Pd(111) substrate; (ii) after depositing enough SiO in $2{\times}10^{-6}$ Torr O_2 to form 1 MLE SiO_2; and (iii) after SiO deposition and annealing at 950 K in $2{\times}10^{-6}$ Torr O_2. Curves (i) and (ii) are normalized such that the Pd MVV peak at 330 eV has the same intensity. The same normalization factor applied to curve (ii) to match the Pd MVV intensity in curve (i) was applied to curve (iii). (b) Nickel 2p X-ray photoelectron and (c) RAIRS spectra obtained after SiO deposition and O2 annealing. 88

5.2 (a)(b) Low energy electron diffraction patterns obtained following silica deposition and annealing in oxygen. (c) Schematic representation of the moiré pattern achieved by rotating the overlayer [1 1] direction to align with the Ni-Pd[$\bar{1}$10]. The black dots denote the Ni-Pd substrate atom positions and the red hexagons represent the ring structure of corner-sharing SiO_4 tetrahedra found in 2D silica and silicates. In the inset, the integer multiple relation between the lattice constants of the overlayer and Ni-Pd substrate are highlighted. (d) Reciprocal space image generated by applying fast Fourier transforming the model in (c). The red dashed lines in (a), (b) and (d) highlight the overlayer reciprocal unit cell and the circles in (b) and (d) show the integer relationship between the overlayer and substrate. 90

5.3 (a) Large-scale STM images obtained after silica deposition and annealing in oxygen. The blue dashed circle outlines a region with a honeycomb arrangement and the red dashed line circles a hexagonal pattern. The white arrow in the lower center points to a brighter maximum and the black arrows at the right show the appearance of secondary maxima that intensify from the bottom to the top of the image. (b)-(d) Atomic-scale images of the same surface shown in (a). (b) The hexagonal ring structures in the green dashed circle show uniform contrast while within the gray dashed circle the contrast varies around the central dark spots. (c) Zoom-in of (b) which indicates a 3° offset between the long-range and short-range periodicities; i.e. the line joining the brightest spots in the long-range periodicity is rotated from the high symmetry direction of the atomic structure by 3°. The corrugation of the long-range moiré pattern ranges from 0.55 to 0.65 Å and the local corrugation of the ring structures from 0.20 to 0.25 Å. Sample biases were (a) 0.8 V (b), (c) 1.25 V (d) 0.85 V. 92

5.4 Schematic representation of the moiré pattern achieved by rotating the substrate atoms in Figure 5.2c counterclockwise by 0.3° to reproduce the rotation experimentally observed in Figure 5.3 between the moiré pattern and the high symmetry direction of the atomic structure. (a) Relative arrangement of the overlayer ring structure and substrate atoms. (b) The rotation of the moiré pattern with respect to overlayer. The arrows in the inset indicate the 3° angle between moiré [1 0] and overlayer [1 1]. (c) Reciprocal space image generated by applying fast Fourier transforming the model in (b). 93

5.5 Top and side views of the most stable structures of the Ni silicate and silica thin layers on $Ni_{0.5}Pd_{0.5}$ alloy substrate (chemical formulas are shown per $(2 \times 2\sqrt{3})$ surface unit cell): (a) Ni silicate with chemisorbed oxygens on the substrate $Ni_4Si_4O_{16}{\cdot}2O/Ni_{0.5}Pd_{0.5}$. (b) Ni silicate on the clean substrate surface $Ni_4Si_4O_{16}/Ni_{0.5}Pd_{0.5}$. (c) Bilayer silica with chemisorbed oxygens on the substrate $Si_8O_{16}{\cdot}2O/Ni_{0.5}Pd_{0.5}$. (d) Monolayer silica with chemisorbed oxygens on the substrate $Si_4O_{10}{\cdot}2O/Ni_{0.5}Pd_{0.5}$. Color scheme: Si cyan, O red, Ni (in the overlayer) black, Ni (on the substrate surface) grey, Ni-Pd VCA atom white. 96

5.6 RAIRS spectra simulated for the structures depicted in Figure 5.5. The simulated IR peaks are broadened by a 3.0 cm^{-1} Gaussian smearing with the largest peak scaled to 1 (in arbitrary unit) for each structure. 101

5.7 Simulated STM images of Ni silicate on $Ni_{0.5}Pd_{0.5}$ alloy substrates. (a) Ni silicate on $Ni_{0.5}Pd_{0.5}$ without interfacial oxygen. (b)-(e) Ni silicate with chemisorbed oxygens initialized at different sites on the surface: (b) on the hcp hollow site; (c) on the fcc hollow site; (d) on top of one substrate atom (e) on the bridge site. The color bar maps the color from the simulated images to the tip height in STM. The locations of top layer Si and O atoms are marked here relative to the metal atoms in the top layer of the alloy substrate so that the different registries of the thin film can be visually identified. Color scheme of the atoms: Si cyan; O red; top layer of the alloy substrate black. The dashed boxes highlight the computational unit cells. 103

6.1 Reflection-absorption infrared spectra recorded following SiO deposition onto $Ni_xPd_{1-x}(111)$ under different preparation conditions. (a) After annealing at 950 K in 2×10^{-6} Torr oxygen for 10 minutes with 1 MLE SiO deposited on $Ni_{0.32}Pd_{0.68}(111)$, (b) After annealing at 950 K in 2×10^{-6} Torr oxygen for 10 minutes with 2 MLE SiO deposited on $Ni_{0.32}Pd_{0.68}(111)$, (c) After annealing at 950 K in 4×10^{-8} Torr oxygen for 5 minutes with 2 MLE SiO deposited on $Ni_{0.48}Pd_{0.52}(111)$ in UHV, and (d) After further annealing the sample shown in Curve (c) at 1000 K in 4×10^{-8} Torr oxygen for 10 minutes. 115

6.2 LEED and STM taken on the sample where Ni silicate and bilayer silica coexist. (a)(b) LEED pattern taken at different electron energies. The red dashed line and green dashed line in (a) indicate the unit cells of commensurate and incommensurate Ni silicate phases in reciprocal space. The arrows show the primary directions of the substrate cells. (c)(d) STM images taken at different scales. The green and blue dashed lines in (c) enclose two crystalline regions with different orientation. The circles and numbers in (d) indicate representative 4- to 8-member silica rings. 117

6.3 LEED pattern after annealing the sample shown in Figure 6.2 at 1000 K in 4×10^{-8} Torr oxygen for 10 minutes. The red dashed line and green dashed line indicate the unit cells of commensurate and incommensurate (rotated 30° overlayer in reciprocal space. The arrows show the substrate ⟨1 0⟩ directions. 119

6.4 Comparison of RAIRS spectra for (a) SiO deposited onto $Ni_{0.07}Pd_{0.93}(111)$ and annealed at 1000 K in 2×10^{-6} Torr O_2 and (b) 2D VDW silica on Pd(111). The peak position in (a) is indicative of 2D Ni silicate formation. 120

6.5 Commensurate-incommensurate transition of Ni silicate with respect to Ni-Pd(111) composition shown by LEED results. (a)-(c) Ni silicate films with only commensurate crystalline phase. (d)-(g) Ni silicate films with the coexistence of incommensurate and commensurate crystalline phase. (h) 2D VDW silica with commensurate and incommensurate crystalline phases. In (a), (d) and (h), the red dashed line and green dashed line indicate the unit cells of non-rotated and rotated overlayer phases in reciprocal space and the arrows show the primary directions of the substrates. The region enclosed by purple dashed line in (d) is better resolved by a LEEM system and is shown in Figure 6.6. The lattice constant of Ni-Pd substrates and corresponding Pd composition is labeled on the color bar. 121

6.6 High-resolution LEED patterns corresponding to the region enclosed by purple dashed line in Figure 6.4d. The red dashed line and green dashed line indicate the unit cells of two crystalline regions. The red dashed line corresponds to the non-rotated phase. The green dashed line corresponds to the phase rotated by 30. 123

6.7 Scanning tunneling microscopy images taken on (a) commensurate crystalline Ni silicate on $\mathrm{Ni_{0.48}Pd_{0.52}}(111)$, (b) incommensurate crystalline Ni silicate on $\mathrm{Ni_{0.26}Pd_{0.74}}(111)$, and (c) incommensurate crystalline 2D VDW silica on Pd(111). 123

6.8 Atomic structures of 2D surface phases on the $Ni_{0.5}Pd_{0.5}$ alloy substrate (chemical formulae are defined per $(2 \times 2\sqrt{3})$ surface unit cell): (a) Substrate (clean surface), (b) 2O/Substrate (one chemisorbed oxygen on the hollow site), (c) Si_4O_{10}/Substrate (monolayer silica), (d) $Si_4O_{10}\cdot 2O$/Substrate (monolayer silica with one chemisorbed oxygen), (e) Si_8O_{16}/Substrate (bilayer silica), (f) $Si_8O_{16}\cdot 2O$/Substrate (bilayer silica with one chemisorbed oxygen), (g) $Ni_4Si_4O_{16}$/Substrate (Ni silicate), (h) $Ni_4Si_4O_{16}\cdot 2O$/Substrate (Ni silicate with one chemisorbed oxygen). Oxygen polyhedrons are drawn to emphasize the neighboring oxygen atoms surrounding the Si and Ni atoms in the 2D thin film. Color scheme: Si cyan, O red, Ni (in the overlayer) black, Ni (on the substrate surface) grey, $Ni_{0.5}Pd_{0.5}$ VCA atom white. Background color under each chemical formula corresponds to the color of region in the phase diagram in Figure 6.9. 126

6.9 Phase diagram for the silica/silicate 2D surface phases on the $Ni_{0.5}Pd_{0.5}$ alloy substrate. Each colored region corresponds to the thermodynamically stable surface phase based on the surface free energy as a function of the Si and O chemical potentials. Letters denoting different phases follow the same notation as Figure 6.8. The bilayer silica can be stabilized above the blue dashed line on the surface. The experimentally accessible region of the chemical potentials in this study is inside of the blue solid line. 128

List of Tables

3.1 Elasto-optic coefficients for bulk crystals (Si, diamond, NaCl, and MgO) obtained using DFPT. For Si, the results are provided for both equilibrium and strained lattices. For diamond, NaCl and MgO, the elasto-optic coefficients based on one-sided (unparenthesized) and two-sided (parenthesized) finite differences using 1% strain are tabulated. 30

3.2 Elasto-optic coefficients for bulk Si obtained using the RPA compared with DFPT. 32

3.3 Dielectric constant for bulk Si using RPA. The first and second columns are the dielectric constant at equilibrium and its change with 1% uniaxial strain along the x-axis. In the third and fourth columns, $\Delta\epsilon_{xx}$ is computed by calculating the dielectric constant at the strained configuration with either the dipole matrix elements $\left\langle \psi_{c,\mathbf{k}} \left| e^{-i\mathbf{q}\cdot\mathbf{r}} \right| \psi_{v,\mathbf{k}+\mathbf{q}} \right\rangle$ or eigenenergies $E_{n,\mathbf{k}}$ in Eq. (3.2) fixed to their equilibrium values. 34

3.4 The dielectric constant and its change with 1% uniaxial strain along x-axis (first three rows of the table) and the ϵ_{yz} component of dielectric tensor and its change with $e_{23} = 1\%$ shear strain (last two rows of the table) for Si. The results in the table are based on a $12 \times 12 \times 12$ grid and are obtained using DFPT, using the RPA with Bloch states from Eq. (3.2), and using Wannier functions from Eq. (3.4) (see Sec. 3.10 for the equations used to compute the full dielectric tensor). 37

3.5 Convergence of dielectric constant in bulk Si using the Wannier RPA method. The columns represent the size of supercell used to generate the Wannier functions. The rows represent the subset of the supercell whose dipole transition are summed up to obtain the dielectric constant. The numbers without parentheses are the dielectric constant ϵ_{xx} of bulk Si at equilibrium; the numbers in parentheses are the change of dielectric constant $\Delta\epsilon_{xx} = \epsilon_{xx}(1.0\%) - \epsilon_{xx}(0.0\%)$ of Si strained uniaxially by 1.0% along the x-axis. . . 40

3.6 Three transition dipole matrix elements $|M|$ with largest magnitude and their changes with different strain are listed in the second to fifth columns; the shell indices in the first column are those described in Figure 3.6. The wave vector $\mathbf{q}$ is along the x-axis for the calculation of the matrix elements, so that $|M|$ is the magnitude of dipole transition vector projected on the x-axis. In the last three columns, each row reports the cumulative contribution from the listed and preceding shells. 42

3.7 Bulk diamond dielectric constant and its change with 1% uniaxial strain along x-axis obtained using DFPT, RPA with Bloch basis and with Wannier basis. The methods used are the same as Table 3.4. The results in the table are based on a $12 \times 12 \times 12$ k grid. 45

3.8 Convergence of dielectric constant in bulk diamond using the Wannier RPA method. The table is in the same nomenclature as Table 3.5. 46

3.9 Three transition dipole matrix elements $|M|$ with largest magnitude and their changes with strain in bulk diamond are listed in the second to fourth column. The shells (in the first column) are indexed the same as bulk Si (see Table 3.6 and Figure 3.6). Last two columns of the table reports the cumulative contribution to $\Delta\epsilon_{xx}$ from the listed shells. The table follows the same notation as Table 3.6. 47

3.10 Bulk rocksalt NaCl dielectric constant and its change with 1% uniaxial strain along x-axis obtained using DFPT, RPA with Bloch states in a plane wave basis and with the Wannier basis. These methods are the same as those in Table 3.4 and Table 3.7. The results in the table are based on a $12 \times 12 \times 12$ k grid. 51

3.11 Convergence with supercell size of the dielectric constant and its strain dependence in bulk NaCl using the Wannier function method. This table uses the same nomenclature as Table. 3.5 and Table. 3.8. 53

3.12 The cumulative contribution to $\Delta\epsilon_{xx}$ of three shells of dipole transitions are shown in the table for NaCl. The shell indices in the first column correspond to those described in Figure 3.14. The table follows the same notation as Table. 3.6's last two columns. 54

3.13 Bulk rocksalt MgO dielectric constant and its change with 1% uniaxial strain along x-axis obtained using DFPT, RPA with Bloch states in a plane wave basis and with the Wannier basis. These methods are the same as those in Table. 3.4 and Table. 3.7. The results in the table are based on a $12 \times 12 \times 12$ k grid. 57

3.14 Convergence with supercell size of the dielectric constant and its strain dependence in bulk MgO using the Wannier function method. The "standard" convergence calculation is not performed for MgO. The results in the table are all based on the $12 \times 12 \times 12$ k grid calculation. This table uses the same nomenclature as Table. 3.5. 58

3.15 The cumulative contribution to $\Delta\epsilon_{xx}$ of three shells of dipole transitions are shown in the table for MgO. The shell indices in the first column are defined the same as those in Figure 3.14 and Table 3.12. The table follows the same notation as Table 3.12. 59

4.1 Binding energies of hexagonal bilayer SiO_2 on various metal substrate computed using the DFT-D2, DFT-vdW, and DFT-vdW^{surf} functionals. The atomic structures for registry 1 and 2 are depicted in Figure 4.1b, c, respectively. The strain is defined by the amount of lattice expansion required to epitaxially strain one unit cell SiO_2 to a (2×2) cell of the hexagonal surface. The SiO_2 overlayer-surface distance d(M-O) is measured by the distance between the bottom-most layer of oxygen atoms in 2D SiO_2 and the metal surface atoms along z direction as per Figure 4.1a. For comparison, the typical bond length between a chemisorbed oxygen atom to its bonded surface metal atom is 2.06 Å, 1.99 Å, and 1.81 Å for Ru(0001), Pd(111), and $Ni_{0.5}Pd_{0.5}$(111), respectively. It is clear that d(M-O) is too large for the formation of chemical bonds between substrate metal atoms and 2D SiO_2 overlayer oxygen atoms. The role of surface chemisorbed oxygen atoms will be disscussed below in Sec.4.3.4. 70

4.2 Energies of commensurate and incommensurate hexagonal 2D bilayer SiO_2 on metal substrates using different vdW corrections (DFT-D2, DFT-vdW, and DFT-vdW^{surf}). The zero energy is referenced by the energy of free-standing 2D SiO_2 in its relaxed lattice constant computed using DFT (5.27 Å). Ru, Pd, and $Ni_{0.5}Pd_{0.5}$ impart 3.5%, 5.8%, and 0.5% theoretical tensile strain on 2D SiO_2, respectively. 76

4.3 Binding energies and geometries of 2D SiO_2 on metal substrates with ordered structure of one adsorbed O per (2×2) surface unit cell. The registry 1 and registry 2 here are defined to have the same SiO_2 alignment with respect to the metal surface as Table 4.1 using the same nomenclature. The 2D SiO_2 overlayer-surface distance d(M-O) is defined in the same way as Table 4.1: it is measured by the vertical distance between the 2D SiO_2 bottom layer oxygens and top layer metal atoms on the surface. The structures of 2D SiO_2 on "oxygen rich" metal substrates with one adsorbed O per (2×2) unit cell are depicted in Figure 4.4. 78

4.4 Energies of commensurate and incommensurate hexagonal 2D bilayer SiO_2 on oxidized metal substrates with one adsorbed O per (2 × 2) surface unit cell using the same nomenclature as Table 4.2. The incommensurate binding energy is computed by averaging the binding energies of 2D SiO_2 (from Table 4.3) in registry 1 and 2 on oxidized metal substrates. 79

5.1 Comparison between the lattice constants of Ni-Pd alloy calculated using VCA and explicit random alloys with experimental data. For $Ni_{0.5}Pd_{0.5}$, 10 random atomic configurations were sampled in 36-atom cells; the reported numbers are the average values of the 10 runs. The lattice constant of the $Ni_{0.3}Pd_{0.7}$ alloy was not computed using explicit random alloy systems, since it is very difficult to set up a simulation cell with reasonable number of atoms with the exact same chemical composition. 95

5.2 Summaries of the key features (energy, atomic structure and simulated STM images) of different registries. The energy of Ni silicate thin film in registry (b) is set to be zero as a reference. The layer thickness is defined as the vertical distance between the top-most oxygen atoms (see Figure 5.5a) and the clean substrate surface with no silicate layer on top. The mean tip height is computed by averaging every data point for each individual registry. The image corrugation is measured by taking the difference in the tip height between highest and lowest positions in each simulated image. 103

Acknowledgment

First and foremost, my special thank goes to my Ph.D. advisor, Sohrab Ismail-Beigi, for his support and guidance throughout my Ph.D. journey. The things he taught me apply to both research and daily life: fundamental physics, programming and debugging, writing, how first principles calculations should work like a detective, how to give a good talk, and how to deal with pressure and plan ahead (just to name a few). I can still vividly remember his remarks regarding giving talks: "every talk could potentially be a job talk" and "keep it simple and stupid". Sohrab is also humorous and fun to talk to: he seems to have many Mullah jokes that he can't wait to share with us in group dinners. In summary, he is the best advisor that any Ph.D. student can ever ask for. Through his mentorship, I matured both academically and personally in the course of Ph.D. studies.

I would like to thank my thesis committee, Prof. Eric I. Altman, Prof. Peter T. Rakich, and Prof. A. Douglas Stone for offering good advices and reading my thesis. Collaboration with Eric on the 2D SiO_2 project is pleasant and has led to three papers either published or in submission. The elasto-optic effect project, which was inspired by Peter's research, is an important part of my Ph.D. thesis. In addition, I learned a lot from Doug's Solid State II class a couple years ago.

The Ismail-Beigi research group members not only are supportive, but also offer great friendships. I always felt comfortable and had some of my best memories when I traveled to conferences with the companions from our group. I would like to thank Jie Jiang, Andrei Malashevich, Arvin Kakekhani, Mehmet Dogan, Alexandru Georgescu, Minjung Kim, Subhasish Mandal, Stephen Eltinge, and Alex Lee. Arvin helped me set up the computing environment on the Yale HPC machines and taught me how to run calculations on them. Alexandru has always been a good buddy to me. We shared the hotel room for all the APS March Meeting he went to as a graduate student. The political and philosophical discussions I had with Mehmet were always delightful. Minjung has always been like an elder sister to me and offered me a lot of advice for life. Stephen shared with me his Matlab script that was used to generate the STM images in this thesis. My appreciation also goes to my experimental collaborators, Chao Zhou and Gregory S. Hutchings. Chao did a lot of heavy lifting when we wrote papers together and some figures in this thesis were refined by him.

Friends at Yale made my life colorful. I would like to thank three undergrad alumni that I came to know at Yale: Xiaohan, Donghai, and Xinyu. They became very close friends to me, and we shared a similar ideology. Our (almost) weekly dinner was wonderful. I hope the four of us can get together to play “Mahjong” again very soon. I also want to thank Luyao, Wen, Dandan, Minglei, Juyue, and Xiaochu for keeping me company, offering good advice, playing board games and pokers with me, and helping me through difficult situations.

My wife, Weiwei, has been my best friend ever since I met her two and a half years ago. She is kind and caring, and she lets me enjoy my life more thoroughly and drags me away from my procrastination habit. Her baking skills are also off the chart. I am incredibly grateful for her love and support along the way. Last but not least, I would like to thank my parents for their love and unconditional support. My mother exemplifies resilience while my father is one of the most respectable people I know. I wish I could spend more time with them.

Chapter 1

Introduction

The goal of this thesis is to use first principles to understand the physical properties of materials at a microscopic level. The main computational tool is density functional theory (DFT) as well as other tools derived from DFT. This thesis has two relatively independent threads of research projects. The first one describes a first principles method for understanding the spatial behavior of the dielectric and photoelastic responses of insulators and semiconductors. The second one concerns a joint effort of experiments and theory to characterize 2D silica and silicate thin films grown on alloy substrates.

The first project in this thesis concerns the elasto-optic effect in solids. The elasto-optic effect, or photoelasticity, describes the linear change of dielectric constant with applied strain and is a universal material property for insulators and semiconductors. Though the elasto-optic responses for solids can be computed directly from first principles (e.g., by using density functional perturbation theory) and measured experimentally, these methods do not provide significant insight into the governing microscopic physical principles of photoelasticity. In this work, we describe a microscopic first principles analysis of photoelasticity in real-space based on localized Wannier functions. We show that the strain-dependent change of dipole transitions between occupied and unoccupied Wannier functions is the main determinant of photoelasticity. By organizing the dipole transitions into spatially localized shells, we find a relatively long-ranged nature of these responses: one needs to sum up contributions of up to third neighbor shells to converge the elasto-optic coefficient with reasonable precision. In our opinion, this makes it unlikely that simple "rule-of-thumb" approaches or models with very few parameters can describe photoelasticity with sufficient accuracy for practical materials design.

The second project in this thesis investigates the growth of 2D silica and silicate thin films on $Ni_xPd_{1-x}(111)$ alloy substrates. In the past decade, the creation of 2D SiO_2 has added a new member to the material class of two-dimensional (2D) Van der Waals (vdW) atomically thin sheet. 2D SiO_2 is the thinnest form of silica known with the SiO_2 stoichiometry. The structure of 2D SiO_2 has no layered structural counterpart in bulk form, and thus it cannot be found by thinning a known bulk phase silica. Apart from being a 2D material, 2D SiO_2 is also of interest because of its structural similarities to zeolite catalysts. 2D bilayer SiO_2, whose chemical reactivity can be introduced by Al dopants to form aluminum silicate, can serve as a model system that imitates the interior surface of bulk zeolites while its 2D nature permits application of surface microscopy techniques that reach atomic scale resolution. We study the properties of 2D SiO_2 on various metal substrates as the first step to understand the chemical properties of 2D Al silicate, which can lead to a better understanding of bulk zeolite's catalytic mechanisms. We employ DFT to study the 2D SiO_2 on various metal substrates and demonstrate that epitaxial strain plays an important role in controlling the morphologies of 2D SiO_2 overlayers, agreeing with prior DFT simulations. We also focus on the structural competition between crystalline hexagonal 2D SiO_2 in commensurate and incommensurate relation to the substrate when epitaxial strain cannot be realized in experiments.

The recent creation of Ni_xPd_{1-x} random alloy (by our collaborators from Altman's group at Yale) [1] provides a substrate system with a continuously tunable lattice constant (through changing the chemical composition), enabling the study of how the substrate lattice mismatch and binding can determine the 2D SiO_2 overlayer's morphology. We are interested in how much epitaxial strain can be imparted in the overlayer before it becomes incommensurate or amorphous. However, the Ni_xPd_{1-x} alloy substrate can form a metal silicate through chemical reaction with the deposited SiO_2 and this adds another layer of complexity. The surface microscopies reveal that high temperature annealing in an oxygen-rich environment causes substrate Ni to segregate towards the surface where it can be oxidized to form a 2D crystalline layer that includes Ni–O–Si bonds. Figure 1.1 depicts

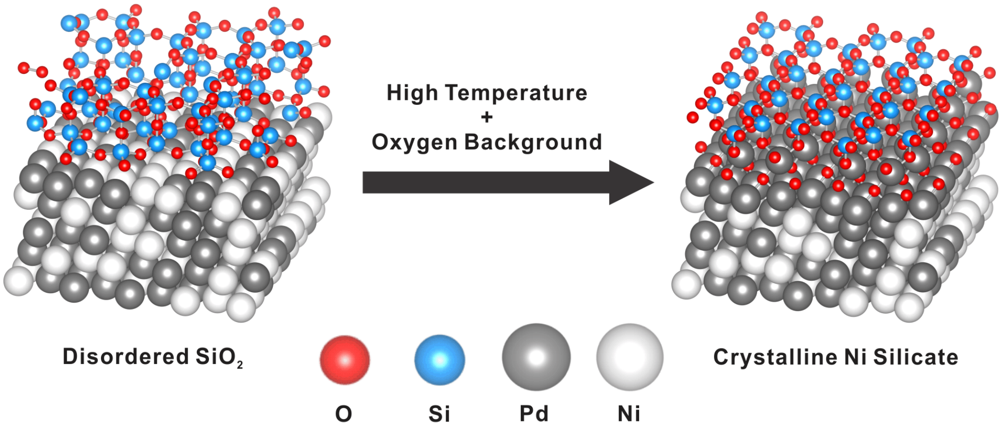

Figure 1.1: A schematic plot showing the process of SiO_2 layer deposited on Ni_xPd_{1-x} alloy surface reacts to the substrate to form Ni silicate thin film.

such a process. We propose a thermodynamically stable Ni silicate structure as a theoretical model for the thin film on the $Ni_xPd_{1-x}(111)$ surface and use DFT to characterize its structural and electronic properties.

The next thrust in this effort has been to understand the phase competition between 2D silica and silicate phases on Ni_xPd_{1-x} alloy substrate in order to avoid the formation of 2D Ni silicate phase and grow 2D SiO_2 in a controlled manner. First principles calculations suggest that by decreasing the oxygen pressure and increasing Si supply, the 2D SiO_2 will become the favorable phase. Experiments show that a decreased oxygen and restricted annealing temperature and time enable the growth of 2D SiO_2.

The structure of the thesis is as follows. In Chapter 2, we briefly review the main theoretical tool, i.e., density functional theory (DFT), throughout this thesis research and other computational tools driven by DFT. In Chapter 3, we present the first principles study of elasto-optic effect in solids, where we focus on analyzing the spatial locality of it using Wannier functions. In Chapter 4, we report the DFT calculations on 2D SiO_2 on various metal substrates, where we examine the effect of epitaxial strain on overlayer morphology and the competition between commensurate and incommensurate structures. In Chapter 5, we present our published study [2] on 2D Ni silicate thin films on Ni_xPd_{1-x} alloy substrate. In Chapter 6, we discuss the competition between 2D silica and silicate phases under different growth conditions. In Chapter 7, we summarize each project presented in this thesis and present a future outlook.

Chapter 2

Methods

2.1 Density functional theory

Electrons in their ground state moving and interacting in a solid can be described by the many-body Schrödinger equation under Born-Oppenheimer approximation:

$$H\Psi_0(\mathbf{r}_1, \mathbf{r}_2, ..., \mathbf{r}_N) = E_0\Psi_0(\mathbf{r}_1, \mathbf{r}_2, ..., \mathbf{r}_N) \tag{2.1}$$

where Ψ_0 is the ground state wave function with energy E_0, and $\mathbf{r}_i$ is the coordinate of electron number i (we suppress the spin index for simplicity). The non-relativistic many-body Hamiltonian can be decomposed into three terms as follows

$$H = T + V_{ee} + V_{ei} \tag{2.2}$$

where T is the kinetic energy (m is the bare mass of an electron)

$$T = -\frac{\hbar^2}{2m}\sum_{i=1}^{N}\nabla^2 \tag{2.3}$$

and V_{ee} is the electron-electron repulsive interactions (e is the elementary charge)

$$V_{ee} = \frac{1}{2}\sum_{i\neq j}\frac{e^2}{|\mathbf{r}_i - \mathbf{r}_j|} \tag{2.4}$$

and V_{ei} is the electron-ion attractive interactions (Z_I is the ionic charge and $\mathbf{R}_I$ is the coordinate of ions)

$$V_{ei} = \sum_i V_{ion}(\mathbf{r}_i) = -\sum_{iI} \frac{Z_I e^2}{|\mathbf{r}_i - \mathbf{R}_I|} = \sum_{i=1}^{N} v(\mathbf{r}_i) \tag{2.5}$$

Solving the many-body Schrödinger equation provides full access to the detailed correlations between all the electrons in the solid. But the many-body problem is essentially impossible to solve exactly, and full wave function Ψ_0 depends on all electronic coordinates. In addition, the problem becomes computationally unmanageable beyond a few electrons since exponentially large storage is needed to store and represent the exact Ψ_0. However, there is no need to track the detailed dynamics of all N electrons simultaneously: physical quantities of interests are typically numbers (e.g., the ground state energy E_0 or the band gap E_g) or a function of a single electronic variable (e.g. electron density $n(\mathbf{r})$), and therefore they are far less complex than the full many-body wave functions. Based on these considerations, a simplified description that delivers only these quantities based on an independent electron framework is preferable.

2.1.1 Hohenberg-Kohn Theorems and Kohn-Sham equations

The main computational tool we use throughout the thesis is density functional theory (DFT) which we will briefly outline in this section. Density functional theory (DFT) [3, 4] is one of main computational tools used in material science and chemistry to understand the electronic structure. DFT provides an, in principle exact, independent electron framework for a many-body electronic system.

There are three foundational theorems in DFT. The first Hohenberg-Kohn First theorem states that total energy of a many-electron system is a functional of its electron density. One can define the relationship through the following expression:

$$E[n] = F[n] + \int d^3\mathbf{r}\, n(\mathbf{r}) v(\mathbf{r}) \tag{2.6}$$

where the second term is the energy from an external potential acting on the electrons (usually the ionic potential caused by nuclei from Eq. (2.2) above). Main observation is that $F[n]$ takes the same form for all many-electron systems regardless of $v(\mathbf{r})$. The second Hohenberg-Kohn theorem states that this energy functional takes its minimum value when $n(\mathbf{r})$ is equal to the ground state density of the system and its minimum value is equal to exact ground state energy E_0. The first and second Hohenberg-Kohn Theorems tell us that we can find both E_0 and $n(\mathbf{r})$ by minimizing $E[n]$ with respect to density $n(\mathbf{r})$. In this way, the number of degrees of freedom needed for finding ground state energy are greatly reduced, from an N-variable many-body wave function $\Psi(\mathbf{r}_1, \mathbf{r}_2, ..., \mathbf{r}_N)$ to a single-variable electron density $n(\mathbf{r})$.

The third theorem of DFT (Kohn-Sham equations) [4] creates an independent electron representation in order to carry out the minimization. First, the N interacting electron system is mapped into an N non-interacting electron system moving in an effective potential which yields the same ground state total energy E_0 and electron density $n(\mathbf{r})$. The $\psi_i(\mathbf{r})$ $(1 \leqslant i \leqslant N)$ are the single-particle orthonormal wave functions for the non-interacting electrons satisfying the following constraints

$$\langle \psi_i \, | \psi_j \rangle = \delta_{ij} \tag{2.7}$$

$$\sum_{i=1}^{N} |\psi_i(\mathbf{r})|^2 = n(\mathbf{r}) \tag{2.8}$$

Then the universal functional $F[n(\mathbf{r})]$ is split into three terms:

$$F[n] = T_s[n] + E_H[n] + E_{xc}[n] \tag{2.9}$$

$$= -\frac{\hbar^2}{2m} \sum_{i=1}^{N} \left\langle \psi_i \left| \nabla^2 \right| \psi_i \right\rangle + \frac{1}{2} \int d^3\mathbf{r} d^3\mathbf{r}' \, \frac{n(\mathbf{r}) \cdot n(\mathbf{r}')}{|\mathbf{r} - \mathbf{r}'|} + E_{xc}[n] \tag{2.10}$$

where $T_s[n]$ is the kinetic energy of the non-interacting electrons described by the wave functions $\psi_i(\mathbf{r})$, $E_H[n]$ is the Hartree energy, and the exchange-correlation energy $E_{xc}[n]$ is defined to be whatever is left over from the other two terms. The third theorem of DFT proves that minimization of energy functional $E[n]$ from Eq. (2.6) with respect to $n(\mathbf{r})$ is equivalent to solve the following N single-particle Schrödinger equations, known as

Kohn-Sham equations:

$$\left[-\frac{\hbar^2}{2m}\nabla^2 + v_{\text{eff}}(\mathbf{r})\right]\psi_i = \epsilon_i\psi_i(\mathbf{r}), \tag{2.11}$$

$$v_{\text{eff}}(\mathbf{r}) = v(\mathbf{r}) + \int d^3\mathbf{r}'\,\frac{n(\mathbf{r}')}{|\mathbf{r}-\mathbf{r}'|} + v_{xc}(\mathbf{r}), \tag{2.12}$$

$$v_{xc}(\mathbf{r}) = \frac{\delta E_{xc}[n]}{\delta n(\mathbf{r})}, \tag{2.13}$$

$$n(\mathbf{r}) = \sum_{i=1}^{N}|\psi_i(\mathbf{r})|^2 \tag{2.14}$$

In these self-consistent single-particle Schrödinger equations, ψ_i is governed by an effective potential which consists of the ionic potential $v(\mathbf{r})$ describing the electron-nucleus attraction, the electrostatic repulsive Hartree potential (second term in v_{eff}), and the exchange-correlation potential $v_{xc}(\mathbf{r})$ which encodes all the many-body effects and correlations among electrons. The ϵ_i are the Lagrange multipliers that enforce the orthonormality constraints of the auxiliary single-particle wave functions ψ_i. We notice that $v_{\text{eff}}(\mathbf{r})$ is dependent on the wave functions $\{\psi_i\}_{1\leqslant i\leqslant N}$ through its dependence on the density $n(\mathbf{r})$, so the N single-particle Schrödinger equations are coupled to each other and need to be solved self-consistently. Once these self-consistent equations are solved and yield the optimal set of wave functions $\left\{\tilde{\psi}_i\right\}_{1\leqslant i\leqslant N}$, the ground state electron density and total energy can be computed as

$$n_0(\mathbf{r}) = \sum_{i=1}^{N}\left|\tilde{\psi}_i(\mathbf{r})\right|^2 \tag{2.15}$$

and

$$E_0 = -\frac{\hbar^2}{2m}\sum_{i=1}^{N}\left\langle\tilde{\psi}_i\left|\nabla^2\right|\tilde{\psi}_i\right\rangle + \frac{1}{2}\int d^3\mathbf{r}d^3\mathbf{r}'\,\frac{n_0(\mathbf{r})\cdot n_0(\mathbf{r}')}{|\mathbf{r}-\mathbf{r}'|} + E_{xc}[n_0] + \int d^3\mathbf{r}\,n_0(\mathbf{r})\cdot v(\mathbf{r}) \tag{2.16}$$

Now we arrive at a theoretically rigorous formula within the independent electron framework which yields exact ground state electron density $n(\mathbf{r})$ and energy E_0. Though strictly speaking the $\{\psi_i\}_{1\leqslant i\leqslant N}$ and $\{\epsilon_i\}_{1\leqslant i\leqslant N}$ in Eq. (2.11) do not necessarily have direct physical meanings (other than the fact that the highest eigenvalue ϵ_N of the highest energy occupied single-particle state ψ_N is equal to the system's Fermi energy or chemical potential [5]), in practice they are interpreted as electron states and eigenenergies to draw physical intuition and understand the system's physical properties.

2.1.2 Exchange-correlation energy functional

Though DFT is theoretically rigorous up to this point by packaging all of our ignorance about electron correlations into the exchange-correlation energy, in practice, one has to adopt some approximation to evaluate the exchange-correlation energy and potential, i.e., $E_{xc}[n]$ and $v_{xc}(\mathbf{r})$, respectively. The most frequently used approximation is the local density approximation (LDA) [6, 7] which takes the following form:

$$E_{xc}^{\mathrm{LDA}}[n(\mathbf{r})] = \int d^3\mathbf{r}\, n(\mathbf{r}) \cdot \varepsilon_{xc}(n(\mathbf{r})). \tag{2.17}$$

In this expression, $\varepsilon_{xc}(n)$ is the exchange-correlation energy per electron in a uniform electron gas with density n. The total exchange-correlation energy in this approximation is the sum of all the electrons' exchange-correlation energy as if they are all embedded in local uniform electron gases with local densities $n(\mathbf{r})$. Accurate numerical values of $\varepsilon_{xc}(n)$ have been calculated by the Quantum Monte Carlo method [8]. Overall, experience shows that LDA works reasonably well in many solids especially those not showing strong and localized electronic correlations. Empirically, LDA is quite good for computing crystal lattice constants, atomic positions and electron densities, ground state energy differences of solids in similar configurations, and is reasonable for computing cohesive and binding energies [9]. It is also widely used to compute band structures of solids though its underestimation of band gaps is a well-known problem [10, 11].

An improved approximation to the exchange-correlation functional, called the generalized gradient approximation (GGA) [12, 13], is to incorporate information on the gradient of electron density:

$$E_{xc}^{\mathrm{GGA}} = \int d^3\mathbf{r}\, n(\mathbf{r}) \cdot \varepsilon_{xc}^{\mathrm{GGA}}(n(\mathbf{r}), |\nabla n(\mathbf{r})|) \tag{2.18}$$

where $\varepsilon_{xc}^{\mathrm{GGA}}(n(\mathbf{r}), |\nabla n(\mathbf{r})|)$ is the exchange-correlation energy per electron with density $n(\mathbf{r})$

and gradient $\nabla n(\mathbf{r})$. The parameterization scheme for GGA exchange-correlation functional used in this thesis is by Perdew, Burke, and Ernzerhof (PBE-GGA) [13]. By including the information about electron density gradient, GGA functionals deals with inhomogeneous electron gas better and shows systematic improvement over LDA in computing the cohesive and binding energies when compared to experiment.

2.1.3 Planewave basis and pseudopotentials

In solid state system, a periodic supercell with Born-von Karman periodic boundary conditions is equivalent to a uniform k-point sampling of the first Brillouin zone. With the help of Bloch's theorem, the electronic eigenstate wave functions of such system can be written as $\psi_{n\mathbf{k}} = e^{i\mathbf{k}\cdot\mathbf{r}} u_{n\mathbf{k}}(\mathbf{r})$, which is a primitive cell-periodic function $u_{n\mathbf{k}}(\mathbf{r})$ modulated by a plane wave. The Bloch eigenstate can be expanded using the plane wave basis set (i.e., a Fourier series) as

$$\psi_{n\mathbf{k}}(\mathbf{r}) = \frac{e^{i\mathbf{k}\cdot\mathbf{r}}}{\Omega} \sum_{\mathbf{G}} c_{n\mathbf{k}}(\mathbf{G}) e^{i\mathbf{G}\cdot\mathbf{r}} \tag{2.19}$$

where $\mathbf{G}$ are the reciprocal lattice vectors and the $c_{n\mathbf{k}}(\mathbf{G})$ are the expansion coefficients. Thus, the Kohn-Sham equations can solved self-consistently by transforming the kinetic operator and effective potential into the plane wave basis. Due to the continuity of wave functions, $c_{n\mathbf{k}}(\mathbf{G}) \to 0$ as $|\mathbf{G}| \longrightarrow +\infty$. In practice, $c_{n\mathbf{k}}(\mathbf{G})$ is truncated to zero once $\frac{\hbar^2}{2m}|\mathbf{G}|^2$ is greater than an energy cutoff E_{cut}. The advantages of using a plane wave basis in solid state systems include: (i) it automatically encodes the periodic nature of crystals, (ii) the kinetic energy has a simple expression in this basis, (iii) it offers an unbiased representation of all spatial regions, and (iv) and its completeness can be systematically improved by increasing the energy cutoff.

The electron wave functions near the nuclei vary rapidly because of the orthonormality constraint on the eigenstates as well as their high kinetic energy. Hence, one requires an enormous number of plane waves with a high energy cutoff to accurately represent this part of wave functions. In order to use a plane wave basis set for first principles calculation for atoms beyond the first two rows of the periodic table, one can use a norm-conserving pseudopotential to reduce the computational cost. The usefulness of the pseudopotential method is based on the observation that the electrons closely bounded to the nuclei, i.e., the low-energy core electrons, are chemically inert and irrelevant in determining the atom's chemical properties in condensed matter systems: hence one does not need to describe them explicitly in the calculation, and their effect on the valence electrons can be incorporated into a smooth pseudopotential that corresponds to smooth valence (pseudo) wave functions. In addition to reducing the plane wave cutoff to manageable values, the pseudopotential approach also reduces the number of electronic states that must be described computationally.

Norm-conserving pseudopotentials are constructed through two approximations after performing an all-electron DFT calculation of an isolated atom. The first approximation is to separate the inert core electrons from the chemically active valence electrons and remove them from the calculation of Kohn-Sham equations for the valence electrons. This is called the frozen core approximation. The second approximation is to replace the oscillatory part of the all-electron wave function of valence electrons within the core region (defined by a cutoff radius r_c) with a smooth function while keeping the wave function outside of r_c and the eigenenergy unchanged to obtain pseudo wave functions. Finally, the pseudopotential is determined such that the solution of the Kohn-Sham equation can generate the corresponding pseudo wave functions with eigenenergies equal to the all-electron calculations. Different pseudopotential schemes use different smooth functions to replace the all-electron wave functions in the core region, and each has its merits. The pseudopotential generation schemes used in this thesis are from Refs. [14–16]. The electronic structure calculations in this thesis are performed in the QUANTUM ESPRESSO [17] software package with plane wave basis and pseudopotentials.

2.1.4 Hellman-Feynman theorem

Given the atomic positions, we can solve the Kohn-Sham equations to obtain the ground state energy and electronic structure for a fixed atomic configurations. However, when we need to search for the optimal atomic coordinates and/or compute equilibrium lattice constants, we cannot exhaustively sample the whole phase space of possible atomic configurations since it is exponentially large in the number of atoms. Instead, a more typical approach is to start with a number of reasonable initial guesses and to iteratively improve the atomic coordinates according to the directions of the forces on the atoms to locate local minima. The Hellman-Feynman theorem permits the efficient computation of the forces exerted on each ion. By definition, the force on ion I is the partial derivative of the total energy (including the electronic part and ionic part) with respect to the atomic coordinate $\mathbf{R}_I$

$$\mathbf{F}_I = -\frac{\partial}{\partial \mathbf{R}_I}\left(E_0 + E_{ii}\right) \tag{2.20}$$

where E_0 is the electronic ground state energy obtained from DFT and E_{ii} is the electrostatic repulsive energy between ions that takes the form

$$E_{ii} = \frac{e^2}{2} \sum_{J \neq K} \frac{Z_J \cdot Z_K}{|\mathbf{R}_J - \mathbf{R}_K|}. \tag{2.21}$$

The second term in the partial derivative in Eq. (2.20) is straightforward to compute since E_{ii} has only an explicit dependence of atomic coordinates. The evaluation of the derivative of E_0 in the first term of Eq. (2.20) is more complex because E_0 has both explicit dependence (through the ionic potential $v(\mathbf{r})$ in Eq. (2.6)) and implicit dependence (through the electron density $n(\mathbf{r})$ in Eq. (2.6)) on the atomic coordinates $\mathbf{R}_I$. Formally, the first derivative is

$$\mathbf{F}_I = -\frac{\partial E_0}{\partial \mathbf{R}_I} = -\int d^3\mathbf{r}\, \frac{\delta E_0}{\delta n(\mathbf{r})} \cdot \frac{\partial n(\mathbf{r})}{\partial \mathbf{R}_I} - \int d^3\mathbf{r}\, n(\mathbf{r}) \cdot \frac{\partial v(\mathbf{r})}{\partial \mathbf{R}_I} \tag{2.22}$$

However, since E_0 is evaluated through a variational principle and has already been minimized over variations of the electron density $n(\mathbf{r})$, the first integral is in the previous equation is equal to zero (this is the essence of the Hellman-Feynman theorem) while the analytical formula for $\frac{\partial v(\mathbf{r})}{\partial \mathbf{R}_I}$ in the second integral can be explicitly worked out. Thus, the total force on the ion I can be written as

$$\mathbf{F}_I = -\int d^3\mathbf{r}\, n(\mathbf{r}) \cdot \frac{\partial v(\mathbf{r})}{\partial \mathbf{R}_I} - \frac{e^2}{2} \frac{\partial}{\partial \mathbf{R}_I} \sum_{J \neq K} \frac{Z_J \cdot Z_K}{|\mathbf{R}_I - \mathbf{R}_K|} \tag{2.23}$$

which can be evaluated simply using the ground state electron densities.

2.2 Density functional perturbation theory

In this thesis, we need to compute the dielectric response of an insulating material to a static and homogeneous external electric field using first principle calculations. When an external electrical field $\mathbf{E}_{ext}$ is applied to a solid, the electrons and nuclei will rearrange themselves and create an induced polarization $\mathbf{P}$ in response to the imposed filed. The macroscopic electric displacement in the solid is $\mathbf{D} = \mathbf{E} + 4\pi\mathbf{P}$ where $\mathbf{E}$ is the screened electric field instead of the bare imposed $\mathbf{E}_{ext}$. Since polarization and electric field are conjugate variables, the polarization can be evaluated as the derivative of the free energy of the system versus $\mathbf{E}$. At zero temperature, the free energy is equal to the quantum mechanical ground state energy which we can compute using DFT. So we have

$$\mathbf{P}_i = -\frac{\partial E_0[\mathbf{E}]}{\partial \mathbf{E}_i} \tag{2.24}$$

In macroscopic linear response Maxwell theory, the dielectric tensor describes the response of solids to electric fields by relating the displacement to the the electric field via the dielectric tensor

$$\mathbf{D}_i = \mathbf{E}_i + 4\pi\mathbf{P}_i = \sum_{j=1}^{3} \epsilon_{ij}\mathbf{E}_j \tag{2.25}$$

By substituting Eq. (2.24) into Eq. (2.25), one arrives at

$$\epsilon_{ij} = \delta_{ij} - 4\pi \left.\frac{\partial^2 E_0[\mathbf{E}]}{\partial \mathbf{E}_i \partial \mathbf{E}_j}\right|_{\mathbf{E}=0} \tag{2.26}$$

If the frequency of the external electrical field is much higher than the typical frequency of phonons, the nuclei will not respond to the external field, and therefore their positions will remain fixed. In this circumstance, the dielectric tensor only has an electronic contribution and is called ε^{∞} in the literature. In this work, we only consider ε^{∞} so will omit the ∞ in the superscript throughout. Eq. (2.26) shows that the dielectric tensor can be related to the second order derivatives of ground state energy with respect to electric fields. Density functional perturbation theory (DFPT) [18] provides a computational approach for calculating quantities that can be expressed as derivatives of the ground state energy versus a variety of parameters. From Eq. (2.26), we see that the dielectric tensor falls into this category if we treat $\mathbf{E}$ as a parameter. We briefly outline the method of computing dielectric tensors with the help of DFPT as follows.

Usually, a system has explicit dependence on parameters only through the potential acting on the electrons. For simplicity, we call the parameters $\{\lambda_i\}$ ($\lambda_i = \mathbf{E}_i$ in our case). We can write the ground state energy E_0 with an emphasis on its parameter dependence and its derivatives in the first two orders as

$$\begin{aligned} E_0[n_\lambda(\mathbf{r}),\lambda] &= F[n_\lambda(\mathbf{r})] + \int d^3\mathbf{r}\, n_\lambda(\mathbf{r}) v_\lambda(\mathbf{r}) \qquad (2.27) \\ \frac{\partial E_0}{\partial \lambda_i} &= \int d^3\mathbf{r}\, \left.\frac{\delta E_0}{\delta n(\mathbf{r})}\right|_{n=n_\lambda} \cdot \frac{\partial n_\lambda(\mathbf{r})}{\partial \lambda_i} + \int d^3\mathbf{r}\, n_\lambda(\mathbf{r}) \frac{\partial v_\lambda(\mathbf{r})}{\partial \lambda_i} = \int d^3\mathbf{r}\, n_\lambda(\mathbf{r}) \frac{\partial v_\lambda(\mathbf{r})}{\partial \lambda_i} \qquad (2.28) \\ \frac{\partial^2 E_0}{\partial \lambda_i \partial \lambda_j} &= \int d^3\mathbf{r}\, \frac{\partial n_\lambda(\mathbf{r})}{\partial \lambda_j} \cdot \frac{\partial v_\lambda(\mathbf{r})}{\partial \lambda_i} + \int d^3\mathbf{r}\, n_\lambda(\mathbf{r}) \frac{\partial^2 v_\lambda(\mathbf{r})}{\partial \lambda_j \partial \lambda_i} \qquad (2.29) \end{aligned}$$

in which $n_\lambda(\mathbf{r})$ means ground state electron density associated with some potential $v_\lambda(\mathbf{r})$ depending on λ. In the second line of this equation, the minimization condition of the energy E_0 at $n_\lambda(\mathbf{r})$ is used which means that $\left.\frac{\delta E_0}{\delta n(\mathbf{r})}\right|_{n=n_\lambda} = 0$. This means that the response of the density to the change of parameters is not needed when computing the first order derivatives. And we only need to know the linear order response of density (its first derivatives $\frac{\partial n}{\partial \lambda}$) to compute the second order derivatives of the energy. Hence, the task turns into finding $\Delta n(\mathbf{r})$ for some small imposed $\{\Delta\lambda_i\}$. Linearizing $\Delta n(\mathbf{r})$ in Eq. (2.8) in terms of the small change of eigen wave functions $\Delta\psi_j$ leads to

$$\Delta n(\mathbf{r}) = \sum_{j=1}^{N} \psi_j^*(\mathbf{r}) \Delta\psi_j(\mathbf{r}) + \text{c.c.} \tag{2.30}$$

where the finite-difference operator is defined as $\Delta F = \sum_j \frac{\partial F}{\partial \lambda_j} \Delta\lambda_j$. Eq. (2.30) shows that the solution for $\Delta n(\mathbf{r})$ amounts to the solution for the eigenstates' first order variations $\{\Delta\psi_i(r)\}_{1 \leqslant i \leqslant N}$. From perturbation theory in quantum mechanics, $\Delta\psi_i(r)$ can be written in a close form as

$$\Delta\psi_i(\mathbf{r}) = \sum_{i \neq j} \psi_i(i) \frac{\langle \psi_i \left| \Delta v_{\text{eff}} \right| \psi_j \rangle}{\epsilon_j - \epsilon_i} \tag{2.31}$$

Substituting Eq. (2.31) into Eq. (2.30) leads to

$$\Delta n(\mathbf{r}) = \sum_{j=1}^{N} \sum_{i \neq j} \psi_j^*(\mathbf{r}) \psi_i(\mathbf{r}) \cdot \frac{\langle \psi_i \left| \Delta v_{\text{eff}} \right| \psi_j \rangle}{\epsilon_j - \epsilon_i} + \text{c.c.} \tag{2.32}$$

But one can not get $\Delta n(\mathbf{r})$ from a direct evaluation of Eq. (2.32) as a one-shot method. The problem is twofold: the summation in the formula requires knowledge of the full spectrum of Kohn-Sham equations which cannot be achieved practically, and $\Delta v_{\text{eff}}(\mathbf{r})$ manifests its dependence on $\{\Delta \psi_i(\mathbf{r})\}_{1 \leqslant i \leqslant N}$ through $\Delta n(\mathbf{r})$ which is unknown beforehand. The key trick in DFPT is to write the first order perturbation result as a linearized equation for $\Delta \psi_j(\mathbf{r})$:

$$(H_{\text{scf}} - \epsilon_j) \left| \Delta \psi_j \right\rangle = -(\Delta v_{\text{eff}} - \Delta \epsilon_j) \left| \psi_j \right\rangle \tag{2.33}$$

where $H_{\text{scf}} = -\frac{\hbar^2}{2m} \nabla^2 + v_{\text{eff}}(\mathbf{r})$ is the self-consistent Hamiltonian for the unperturbed system and $\Delta \epsilon_j = \langle \psi_j \left| \Delta v_{\text{eff}} \right| \psi_j \rangle$. Solving this linear equation can be done iteratively (and efficiently) using numerical methods and does not require the full spectrum of the Hamiltonian. DFPT then solves this equation self-consistently in a manner similar to solving the Kohn-Sham equations. The left hand side of this equation is singular but only in the subspace of occupied states. Eq. (2.32) shows that the contributions to $\Delta n(\mathbf{r})$ from products of two occupied states cancel each other, so what really matters is the solution of $\Delta \psi_j(\mathbf{r})$ in the subspace of unoccupied states where the equation is not singular. One can eliminate the singularity of the left hand side by adding αP_v and projecting the right hand side onto the subspace of conduction bands

$$(H_{\text{scf}} + \alpha P_v - \epsilon_j) \left| \Delta \psi_j \right\rangle = -P_c \Delta v_{\text{eff}} \left| \psi_j \right\rangle \tag{2.34}$$

where P_v and P_c are the projections operators onto valence and conduction bands. The second equation of DFPT (Eq. (2.34)) yields the same solution with the first one (Eq. (2.33)) in conduction bands subspace. The formulae for dielectric tensor in solids have been explicitly worked out in DFPT in the review paper of Ref. [18].

2.3 Maximally Localized Wannier Functions

Electrons in crystals are often described by the Bloch waves $\psi_{n\mathbf{k}}(\mathbf{r})$, i.e., eigenstates of the periodic crystal Hamiltonian that extend through the whole solid with the quantum number of band index n and crystal momentum $\mathbf{k}$. When we want a description of localized phenomena, e.g., a chemical bond or point defect in solids, the Bloch representation becomes less convenient. Alternatively, one can use Wannier functions to describe the electronic structures of the crystals. For a single isolated band, Wannier functions with band index n can be achieved by the Fourier transform of Bloch states from the $\mathbf{k}$ representation to the $\mathbf{R}$ representation

$$W_{n\mathbf{R}}(\mathbf{r}) = \frac{V}{(2\pi)^3}\int_{\mathrm{BZ}} d^3\mathbf{k}\; e^{-i\mathbf{k}\cdot\mathbf{R}}\,\psi_{n\mathbf{k}}(\mathbf{r}) \tag{2.35}$$

where V is the volume for the primitive cell of the crystal and the integral runs over the first Brillouin zone (BZ). It can be seen from the basic properties of Fourier transforms that Wannier functions with different lattice indices $\mathbf{R}$ are orthonormal to each other and, in fact, are related to each other through lattice translations: they can be written as $W_{n\mathbf{R}}(\mathbf{r}) = W_n(\mathbf{r}-\mathbf{R})$. In addition, since they are unitary transforms of the Bloch states, the set of Wannier functions for a band span the same Hilbert space as the Bloch states so no information is lost. Wannier function can be made localized in real-space (see below), hence they are useful tools in understanding localized electronic properties. However, Wannier functions are nonunique due to the "gauge" degree of freedom in the definition of Bloch states, leading to difficulties in applying Wannier functions directly without further constraints. For example, at each k-point, Bloch states are determined up to an arbitrary phase $\psi_{n\mathbf{k}}(\mathbf{r}) \longrightarrow \psi_{n\mathbf{k}}(\mathbf{r})\cdot e^{i\theta_n(\mathbf{k})}$, and such gauge freedom translates into the Wannier functions changing their shape after the Fourier transform.

Composite Bands

More generally, for a group of N interconnected composite bands that are isolated in energy (i.e. separated by gaps from other bands across the whole BZ), the gauge freedom manifests itself through mixing of Bloch states at each k-point through a unitary transformation matrix $U^{(\mathbf{k})}$ when defining the Wannier functions [19]:

$$W_{n\mathbf{R}}(\mathbf{r}) = \frac{V}{(2\pi)^3}\int_{\mathrm{BZ}} d^3\mathbf{k}\, e^{-i\mathbf{k}\cdot\mathbf{R}} \sum_{m=1}^{N} \psi_{m\mathbf{k}}(\mathbf{r}) \cdot U_{mn}^{(\mathbf{k})} \tag{2.36}$$

where $U^{(\mathbf{k})}$ is a $N \times N$ unitary matrix at each k-point. Different choice of $U^{(\mathbf{k})}$ lead to Wannier functions with different spatial shapes and localities. Therefore, one needs constraints in the generation of Wannier functions to determine the $U^{(\mathbf{k})}$ before using them in practice.

The Maximally Localized Wannier Functions (MLWFs) ansatz proposed by Marzari and Vanderbilt [19] fixes the gauge degree of freedom by minimizing the sum of the quadratic spreads of the Wannier functions in real-space using the following expression

$$\Omega = \sum_{n=1}^{N} \left(\left\langle W_{n\mathbf{0}} \left| r^2 \right| W_{n\mathbf{0}} \right\rangle - \left| \left\langle W_{n\mathbf{0}} \left| \mathbf{r} \right| W_{n\mathbf{0}} \right\rangle \right|^2 \right) \tag{2.37}$$

where Ω is the sum of the quadratic spreads of all the Wannier function in the home unit cell. Ω can be further decomposed into two parts as

$$\Omega = \Omega_{\mathrm{I}} + \tilde{\Omega} \tag{2.38}$$

where

$$\Omega_{\mathrm{I}} = \sum_{n=1}^{N} \left[\left\langle W_{n\mathbf{0}} \left| r^2 \right| W_{n\mathbf{0}} \right\rangle - \sum_{\mathbf{R}m} \left| \left\langle W_{m\mathbf{R}} \left| \mathbf{r} \right| W_{n\mathbf{0}} \right\rangle \right|^2 \right] \tag{2.39}$$

and

$$\tilde{\Omega} = \sum_{n=1}^{N} \sum_{\mathbf{R}m \neq \mathbf{0}n} \left| \left\langle W_{m\mathbf{R}} \left| \mathbf{r} \right| W_{n\mathbf{0}} \right\rangle \right|^2 . \tag{2.40}$$

It can be shown that both Ω_{I} and $\tilde{\Omega}$ are positive-definitive quantities and Ω_{I} is gauge invariant [19], i.e., its value is invariant under different choice of the $U^{(\mathbf{k})}$ matrices. Hence, the minimization of Ω corresponds to the minimization of $\tilde{\Omega}$.

It turns out that the evaluation of the matrix element of the position operator $\mathbf{r}$ in the expressions for the quadratic spread does not have to be carried out in real-space. In fact, using the quantum mechanical equivalent relationship [20, 21] of the position operator

$\mathbf{r}$ in real-space and the derivative operator $-i\nabla_{\mathbf{k}}$ in momentum-space, the information needed to compute the matrix elements in Eq. (2.39) and Eq. (2.40) is the momentum-space derivatives encoded in the overlaps between the Bloch states (the periodic part) at neighboring k-point

$$M_{mn}^{(\mathbf{k},\mathbf{b})} = \langle u_{m\mathbf{k}} | u_{n\mathbf{k}+\mathbf{b}} \rangle \tag{2.41}$$

where $\mathbf{b}$ is the vector that connects two adjacent points in the k-point grid and the $u_{n\mathbf{k}}(\mathbf{r})$ are the cell-periodic parts of the Bloch states, $\psi_{n\mathbf{k}}(\mathbf{r}) = e^{i\mathbf{k}\cdot\mathbf{r}} u_{n\mathbf{k}}(\mathbf{r})$. The overlaps $M_{mn}^{(\mathbf{k},\mathbf{b})}$ only need to be calculated once at the start of the "Wannierization" procedure, and the actual minimization of the spreads only depends on the unitary matrices $U^{(\mathbf{k})}$ and the overlaps $M_{mn}^{(\mathbf{k},\mathbf{b})}$. Thus, the generation of MLWFs can be treated as a post-processing step to the standard electronic structure calculation. For the work in this thesis, the QUANTUM ESPRESSO [17] electronic structure software is used together with the WANNIER90 MLWF generation software [22, 23].

Iterative minimization of Ω starts with some reasonable initial guess for the Wannier functions, which requires *a priori* knowledge of the material being studied. Different initial guesses can lead to different MLWFs produced. For example, one can achieve either bonding and antibonding-like Wannier functions or sp^3 hybrid-like Wannier functions for tetrahedral insulators (e.g. diamond and Si). MLWFs are found to be exponentially localized around their centers [24, 25] and are real-valued functions [20]. Wannier functions, because of their construction, span the same Hilbert space as the Bloch bands, leading to a localized basis set for electrons that reaches the same level of accuracy as the first principles method. Due to their exponential locality, Wannier functions can be used as the basis for linear-scaling electronic structure methods [20]. Next, Wannier functions can provide local chemical information that is hard to extract from the Bloch state representation of electrons. Finally, the centers of Wannier functions can be interpreted as the coordinates of the electrons when computing the electronic polarization and provide an intuitive connection to the modern theory of polarization [26].

Entangled Bands

In certain cases, the energy bands we wish to Wannierize overlap in energy (i.e., are entangled) with other undesired bands. For instance, in copper, the bands with d characters are hybridized with a dispersive band with s character, and we need to “pick” the bands with d characters before constructing MLWFs for them. The “disentanglement” procedure developed in Ref. [27] selects the right energy bands before sending them to the spread-minimizing Wannierization procedure (described in the previous section for composite bands).

We briefly describe the main physical ingredient of the disentanglement procedure. To perform the disentanglement procedure and obtain N bands, we first identify an energy window (“outer window”) that can includes all the targeted bands as well as some undesired bands. Then, at each k-point, we define a transformation matrix $V^{(\mathbf{k})}$ that mixes the $J^{\mathbf{k}}$ eigenstates ($J^{\mathbf{k}} \geqslant N$) whose energy falls in the outer window to produce a set of N orthonormal Bloch states :

$$\psi_{n\mathbf{k}}^{\text{opt}}(\mathbf{r}) = \sum_{m \in J^{\mathbf{k}}} \psi_{m\mathbf{k}}(\mathbf{r}) \cdot V_{mn}^{(\mathbf{k})} \tag{2.42}$$

before sending the Bloch states $\psi_{n\mathbf{k}}^{\text{opt}}(\mathbf{r})$ to the Wannierization procedure described above for composite bands. At each k-point, the $V^{(\mathbf{k})}$ is a rectangular unitary matrix with dimension $J^{\mathbf{k}} \times N$ which obeys $\left\{V^{(\mathbf{k})}\right\}^{\dagger} \cdot V^{(\mathbf{k})} = \mathbb{I}$. Hence, disentangling is equivalent to choosing a set of $V^{(\mathbf{k})}$ to produce a set of Bloch states $\psi_{n\mathbf{k}}^{\text{opt}}(\mathbf{r})$ that can ensure maximal locality (i.e., minimize Ω) after the Wannierization procedure. As noted above, the Ω_{I} only depends on $V^{(\mathbf{k})}$ and $\tilde{\Omega}$ depends on both $V^{(\mathbf{k})}$ and $U^{(\mathbf{k})}$. Therefore, the heuristic for constructing MLWFs for entangled energy bands is naturally decomposed into two step: first Ω_{I} is minimized with respect to $V^{(\mathbf{k})}$ to achieve a set disentangled bands, then $\tilde{\Omega}$ is minimized with respect to $U^{(\mathbf{k})}$ to achieve MLWFs. Conceptually, the disentanglement corresponds to selecting subspaces at each k-point that are smoothiest across the BZ, and the Wannierization corresponds to selecting a gauge that smoothly varies the phases of Bloch states in the BZ. The smoothness of the Bloch states in momentum-space leads to localization of MLWFs in real-space.

The usage of MLWFs in solid state systems will be detailed below in Chapter 3.

2.4 Van der Waals corrections

Dispersive interaction, or Van der Waals (vdW) interaction, will exist between two separate fragments of matter that consist of charged particles whose positions can fluctuate. Van der Waals interactions originate from the long-ranged electrostatic interactions between quantum mechanically fluctuating dipoles and play an important role in the chemical properties of inorganic molecules and 2D material heterostructures [28,29]. In principle, all correlation effects including vdW interactions are included in the exact DFT exchange-correlation functional $E_{xc}[n]$; in practice, however, semi-local approximations such as LDA and PBE-GGA do not contain such long-ranged correlations. How one can try to incorporate vdW effects into the DFT framework is an active field of research, and the available schemes fall into two general categories: (i) adding explicitly non-local density-density interaction terms in the exchange-correlation functional $E_{xc}[n]$ to capture the long-ranged correlations between electron densities [30], (ii) adding a simple semi-empirical correction term "on top of" the DFT energy which is proportional to the London formula $-C_6/R^6$ at large interatomic separation R asymptotically. The three vdW corrections used in this thesis belong to category (ii), which we shall outline briefly here.

The energy correction term for evaluating the total energy for the three vdW functionals (i.e., DFT-D2, DFT-vdW, DFT-vdW$^{\mathrm{surf}}$) take the form

$$E_{\mathrm{disp}} = -\sum_{\langle i,j\rangle} f_{\mathrm{dmp}}(R_{ij}) \cdot \frac{C_6^{ij}}{R_{ij}^6} \tag{2.43}$$

where C_6^{ij} is the dispersion coefficient, R_{ij} is the interatomic distance between atom i and atom j, and the summation $\langle i,j\rangle$ runs over each pairs of the atoms in the system. $f_{\mathrm{dmp}}(R_{ij})$ is a damping function which converges to 1 at large interatomic distance ($R_{ij} \longrightarrow +\infty$) to achieve a correct asymptotic behavior and decays to zero exponentially fast at small interatomic distance ($R_{ij} \longrightarrow 0$) to suppress any singularities in the dispersion term. Three vdW functionals differentiate from each other in how the C_6^{ij} dispersion coefficients are determined:

- DFT-D2 [31] obtains its C_6^{ij} coefficients from first principles calculations of isolated atoms of species i and j. C_6^{ij} is determined by atom i and j's atomic ionization potential and atomic dipole polarization.

- DFT-vdW [32] first computes the free-atom coefficients $C_{6,\,\mathrm{free}}^{ij}$ as reference values using frequency-dependent polarizabilities of atoms i and j reported from time-dependent DFT (TDDFT) calculations. The dispersion coefficient C_6^{ij} used in the solid state calculation is scaled from free-atom $C_{6,\,\mathrm{free}}^{ij}$ based on the "effective volume" of atom i and j in the solid environment to account for the change of atomic polarizability with the chemical environment.
- DFT-vdW$^{\mathrm{surf}}$ [33] is designed for describing the dispersive interaction between the organic molecules and metallic substrates. It builds on top of the DFT-vdW framework and can further include the effect of the metallic substrate's screening behavior.

Chapter 3

Degree of locality of elasto-optic response in solids

Note: This chapter is adopted from an article we have submitted to *Physical Review B,* and it is under review.

3.1 Introduction

The elasto-optic effect, or photoelasticity, of a crystal describes the linear response change of optical refractive index with applied strain. By definition, only the electronic contribution to the dielectric response is included in the elasto-optic effect, and therefore it describes the strain dependence of the dielectric tensor at frequencies well above those of lattice vibrations but below the electronic band gap. The elasto-optic effect is of interest for technological applications as well as for fundamental science. For example, the elasto-optic effect reduces the efficiency of fiber Bragg gratings [34]. Next, semiconductor heterostructures in devices such as transistors have built-in inter-layer strains due to the lattice mistmatch between their constituent layers which, via the elasto-optic effect, modifies their electronic and optical properties. The elasto-optic effect also gives rise to birefringence phenomena in crystals by lowing their symmetries. For example, the normally isotropic dielectric constant in cubic solids turns into a rank-two tensor under strain, so that light will propagate with different speeds along different crystallographic axes. This effect has been used to make photoelastic modulators to modulate the polarization of light [35]. In nanoscale systems such as waveguides, the optical forces exerted by electromagnetic waves can be engineered by the elasto-optic effect through its relation with electrostrictive forces, enabling selective excitation of acoustic phonon modes in the waveguides [36]. The coupling between electromagnetic waves and acoustic phonons provide applications in making photonic-phononic devices [37–41]. Since the magnitude and directions of the electrostrictive forces are determined by the elasto-optic and dielectric properties which have strong material dependences, they can be used to enhance or suppress the photon-phonon coupling. Hence, understanding and predicting elasto-optic response helps with the selection or design rules for materials for photon-phonon interactions.

Numerous computational works [42–46] have calculated the elasto-optic tensor for insulators and semiconductors using density functional theory (DFT) [3,4] and density functional perturbation theory (DFPT) [18]. DFPT is a powerful *ab initio* approach that can provide physical insight into the separate responses of electrons and ions, and the DFPT-computed elasto-optic tensors are in a good agreement with available experimental data. However, as a numerical method for response calculations, DFPT does not provide direct insight into the underlying physical principles of elasto-optic behavior in a localized, real-space manner in the sense detailed in Sec. 3.2. There also exist phenomenological models for photoelasticity. Donadio and Bernasconi [46] developed a model to describe the photoelasticity of silica materials. Their model assumes that the dielectric response of silica is entirely determined by the sum over each oxygen atom's polarizability which is affected by the local geometry of the crystal in response to strain. However, the attempt to generalize the model from silica to sodium silicate has been less successful [47]. Another model proposed by Damas *et al.* [48] centralized the role of individual chemical bonds in silicon and their response to lattice distortion based on bond orbital theory for tetrahedrally covalent crystals [49]. By analyzing how the bond polarizability changes with strain in Si, Damas *et al.* were able to extract the strain dependence of silicon's dielectric tensor, i.e., the elasto-optic effect. However, these phenomenological models include a variety of empirical parameters and assumptions on locality and short-ranged electronic response which must be verified and extracted from experimental data or *ab initio* calculations.

In this paper, we aim to understand the governing physical principle of the elasto-optic effect at the microscopic level from first principles. We first show that comparing to state-of-the-art DFPT calculations, the random phase approximation (RPA) presents a simple yet as accurate enough approach for describing the dielectric and elasto-optic response. By rewriting the RPA formula for the dielectric tensor in the basis of Maximally Localized Wannier Functions (MLWFs) [20], we discover that the strain-dependent dipole transitions between occupied and unoccupied Wannier functions are the main determinants of the elato-optic effect. We also reveal a surprisingly long-ranged nature for the dielectric and elasto-optic response using the Wannier basis which means the basic assumptions of many semi-empirical approaches to photoelasticity should be reconsidered carefully. Four insulating materials from two distinct material classes are considered in this work: the covalent semiconductors Si and diamond, and the ionic crystals NaCl and MgO.

The structure of this paper is as follows. Sec. 3.3 describes our computational methods. Sec. 3.4 presents the state-of-the-art DFPT calculations for elasto-optic responses done in this work that are in good agreement with prior first principle calculations and experiments. Sec. 3.5 is devoted to understanding the silicon elasto-optic effect. Sec. 3.5.1 compares the RPA and DFPT methods for calculating the photoelasticity of silicon and suggests that a promising venue to describe the elasto-optic effect is to use Wannier functions. It is also discovered in Sec. 3.5.1 that the change of dielectric constant with strain is dominated by the dipole matrix elements rather than the eigenenergies of the Bloch states. Sec. 3.5.2 furthers the discussion about the dipole transitions by rewriting the matrix elements into the Wannier basis. We then develop a “constrained sum” method in real space by partitioning dipole transitions into shells according to their distances. This “constrained sum” method reveals the long-ranged behavior of the dielectric and elasto-optic response of silicon which can be only understood intuitively in a localized basis set like Wannier functions. Sec. 3.6-3.8 apply the tools developed for Si to diamond, NaCl, and MgO. Similar conclusions about the locality of the photoelasticity can also be drawn for these three materials. We summarize the main findings, their implications and the relation of our work to the prior literature in Sec. 3.9.

3.2 Physical insight and bond-orbital models

As we will see in Sec. 3.4, fully *ab initio* approaches such as DFPT provide reliable tools for numerical computation of dielectric and photoelastic responses. However, such approaches do not provide sufficient insight in terms of a compact localized picture of the response that allows intuitive understanding and development of simple rules of thumb. More precisely, an ideal model would describe the materials response in terms of highly localized orbitals centered on the atoms or bonds constituting the material. Prior work in this area has been based on Harrison's bond orbital model [**?**]: in the simplest approximation, the linear dielectric susceptibility of a tetrahedral covalent solid (e.g., bulk silicon) can be written as

$$\chi_1 = Ne^2\gamma^2 d^2\alpha_c^2/(12V_2)$$

where N is the mean valence electron density, e is the elementary charge, d is the equilibrium bond length between neighboring atoms, α_c is a parameter that describes the covalency of the bonds in the solid (in non-polar materials such as Si, $\alpha_c = 1$), twice V_2 is equal to the energy splitting between the bonding and antibonding orbitals on the same chemical bond, and γ is an adjustable scaling parameter that is used to compensate for the discrepancies between the model and experimental data. All the parameters in the above expression for χ_1 relate to the physical properties of one single chemical bond. Therefore, such a model possesses extreme locality, is straightforward to interpret, and, if accurate, provides an excellent starting point for materials design. Finding the strain dependencies of these parameters describes the photoelastic response within the bond-orbital picture. A recent example of this approach for elasto-optic response can be found in Ref. [48]. Despite the simplicity and easy interpretation of such models, the fact that the adjustable parameters such as γ can only be found by fitting to known materials properties limits their predictive power. Ideally, one would prefer to approach the problem using first principles in order to have predictive power for new materials.

Our fundamental aim in this paper is to answer two basic questions. First, how short-ranged is the photoelastic response when described in a localized bond-orbital type model developed from first principles? In other words, is this physical property short-ranged enough so that a simple physical picture emerges? Second, can the key parameters in the localized model be computed from first principles? Below, we will succeed in developing an *ab initio* real-space approach based on localized Wannier functions to compute the photoelastic response and find that the responses are longer ranged than assumed in the standard bond-orbital picture.

3.3 Computational Methods

The elasto-optic tensor p_{ijkl} is defined by the expression

$$\Delta\epsilon_{ij}^{-1} = p_{ijkl}e_{kl} \tag{3.1}$$

where ϵ_{ij} is the dielectric tensor of the crystal and e_{kl} is the strain tensor. Therefore, the elasto-optic tensor p_{ijkl} is a rank-4 tensor with i, j, k, l being one of the x, y, z axial directions. The notation $\Delta\epsilon^{-1}$ describes the linear response change of ϵ. Since both the inverse dielectric tensor ϵ^{-1} and the strain tensor e are symmetric, the elasto-optic tensor possesses a number of permutation symmetries: $(i \leftrightarrow j)$ and $(k \leftrightarrow l)$ [50]. In this work, we use Voigt's notation to compactify: $1 = xx, 2 = yy, 3 = zz, 4 = yz, 5 = xz$, and $6 = xy$. All the crystal structures studied in this paper (Si, diamond, NaCl, and MgO) have cubic symmetry at equilibrium which makes their elasto-optic tensors have only 3 independent components, i.e., p_{11}, p_{12}, and p_{44}.

In this work, we use density functional theory (DFT) [3, 4] to compute the electronic structure of bulk crystals using the Quantum Espresso software package [17] with periodic boundary conditions and a plane-wave basis. We use the local density approximation (LDA) [6–8] for exchange and correlation and employ norm-conserving pseudopotentials [14, 51] to describe the ionic cores. The four bulk crystals in this paper are all simulated using 2-atom primitive unit cells with their experimental lattice constants of $a_0 = 5.43$ Å, 3.57 Å, 5.64 Å, and 4.21 Å for Si, diamond, NaCl, and MgO, respectively [52]. A $6 \times 6 \times 6$ uniform k-point grid sampling with appropriate energy cutoff (35 Ry for Si, 60 Ry for diamond, 30

Ry for NaCl, and 65 Ry for MgO) achieves total energy convergence within 1 meV/atom. To calculate the static dielectric constant of solids, we use density functional perturbation theory (DFPT) [18] as implemented in QUANTUM ESPRESSO. Since we are interested in describing the change of the dielectric response with strain rather than the dielectric response itself, further analysis reveals that a $12 \times 12 \times 12$ uniform k grid sampling is needed to converge the change of dielectric constant to 0.01 in absolute value with 1% uniaxial strain.

We also use the random phase approximation (RPA) to compute dielectric response [53,54]. The RPA is very useful because it is written as an explicit analytical formula. Our results will show that the RPA provides a highly satisfactory approximation to the more accurate DFPT results for both the dielectric constants and their strain dependences. We use the expression for the longitudinal RPA dielectric constant given by

$$\epsilon = 1 + \frac{16\pi}{V} \cdot \frac{1}{|q|^2} \sum_{\mathbf{k}} \sum_{c,v} \frac{\left| \left\langle \psi_{c,\mathbf{k}} \left| e^{-i\mathbf{q}\cdot\mathbf{r}} \right| \psi_{v,\mathbf{k}+\mathbf{q}} \right\rangle \right|^2}{E_{c,\mathbf{k}} - E_{v,\mathbf{k}+\mathbf{q}}} \tag{3.2}$$

where $V = N_{\mathbf{k}}\Omega$ is the volume of the super cell which is equal to number of k-points $N_{\mathbf{k}}$ multiplied by the volume of the primitive cell Ω. The summation ranges over all pairs of valence (v, occupied) and conduction bands (c, unoccupied) and also the whole Brillouin zone ($\mathbf{k}$). The wave vector $\mathbf{q}$ is that of the external electric field applied to the material, but since photoelasticity is a long-wavelength response (i.e, uniform imposed electric field), we let $|\mathbf{q}|$ approach zero ($|\mathbf{q}|$ is set to be 1% of a primitive reciprocal lattice vector in our calculations).

We aim to use an accurate first principles real-space representation for dielectric response in solids, especially for the $\left\langle e^{-i\mathbf{q}\cdot\mathbf{r}} \right\rangle$ dipole matrix elements in (3.2). A natural choice is to utilize Maximally Localized Wannier Functions (MLWFs) [19,20,27] as the basis set. For a selected set of energy bands, MLWFs span the same Hilbert space as Bloch states since they are constructed by unitary transformation of the Bloch states. MLWFs are exponentially localized in real-space [25], which is a desired feature when describing a system's locality.

The mathematical expression for MLWFs is

$$W_{n,\mathbf{R}}(r) = \frac{1}{\sqrt{N_{\mathbf{k}}}} \sum_{\mathbf{k}} \sum_{m=1}^{J} e^{-i\mathbf{k}\cdot\mathbf{R}} \psi_{m,\mathbf{k}}(r) \cdot U_{m,n}^{(\mathbf{k})} \tag{3.3}$$

where $U^{(\mathbf{k})}$ are rectangular $J \times N_{\mathrm{wann}}$ unitary matrices representing the gauge freedom in building Wannier functions, J is the number of bands targeted to make Wannier functions whereas N_{wann} is the number of Wannier functions wanted per unit cell. The $U^{(\mathbf{k})}$ are determined to achieve the maximal locality criterion [19]. Wannier functions in this work are generated using the WANNIER90 software package [22, 23].

Wannier functions in this work are generated separately for valence and conduction bands so that we can describe dipole transitions between filled (valence) and empty (conduction) Wannier functions in real-space. The spatial characters of the generated Wannier functions are determined by the chemistry of the solids (detailed in Secs. 3.5-3.8). For example, for each 2-atom primitive unit cell of silicon, we generate 4 bonding Wannier functions for the 4 valence bands and then disentangled the low lying conduction bands to generate 4 antibonding Wannier functions. The 8 Wannier functions basis per cell form a "minimum basis set" in a tight-binding model for silicon crystal. By substituting the relation between MLWFs and Bloch states from Eq. (3.3) into Eq. (3.2), we arrive at an expression for the RPA dielectric constant in the MLWF basis:

$$\epsilon = 1 + \frac{16\pi}{V} \cdot \frac{1}{|q|^2} \cdot \sum_{a,b,\mathbf{R}} \sum_{a',b',\mathbf{R}'} M_{a',b',\mathbf{R}'}^{*} \cdot M_{a,b,\mathbf{R}} \cdot F_{a',b',\mathbf{R}';a,b,\mathbf{R}} \tag{3.4}$$

where

$$M_{a,b,\mathbf{R}} = \left\langle W_{a,\mathbf{R}} \left| e^{-i\mathbf{q}\cdot\mathbf{r}} \right| W_{b,\mathbf{0}} \right\rangle \tag{3.5}$$

$$F_{a',b',\mathbf{R}';a,b,\mathbf{R}} = \frac{1}{N_{\mathbf{k}}} \sum_{c,v,\mathbf{k}} e^{-i\mathbf{k}\cdot(\mathbf{R}-\mathbf{R}')} \cdot \frac{U_{ca'}^{(\mathbf{k})*} U_{ca}^{(\mathbf{k})} U_{vb'}^{(\mathbf{k})} U_{vb}^{(\mathbf{k})*}}{E_{c,\mathbf{k}} - E_{v,\mathbf{k}+\mathbf{q}}} \tag{3.6}$$

The summation over $\mathbf{R}, \mathbf{R}'$ in Eq. (3.4) ranges over all lattice vectors in the supercell. Eq. (3.5) is the Wannier dipole matrix element connecting a bonding state in the "home" unit cell (at $\mathbf{R} = 0$) to an antibonding state in unit cell $\mathbf{R}$. Eq. (3.6) is the Fourier transform of the energy difference denominator in the Bloch representation, and $U^{(\mathbf{k})}_{ca}$ and $U^{(\mathbf{k})}_{vb}$ are the unitary matrices mixing conduction and valence bands to make antibonding and bonding Wannier functions, respectively. Eq. (3.4) is a sum over all pairs of dipole transitions in the supercell modulated by the Fourier transform of energy denominator.

Making the unitary transformation of the basis from Bloch states in Eq. (3.2) to Wannier functions in Eq. (3.4) permits us to analyze the spatial behavior (e.g., locality) of the dielectric response. While it is hard to guess the behavior of ϵ versus increasing size of the k-point mesh in Eq. 3.2, the real-space version of Eq. (3.4) is more transparent to analyze since we are increasing the size of the supercell by including longer $\mathbf{R}$ vectors. As $\mathbf{R}$ grows, $M_{a,b,\mathbf{R}}$ will decrease since it involves the overlap of two Wannier functions that are at growing separations: we expect the sum in Eq. (3.4) to converge as successively larger $\mathbf{R}$ vectors are included. In addition, we can make a reasonable guess (verified numerically below) on the type of convergence that will be seen. Since $F_{a',b',\mathbf{R}';a,b,\mathbf{R}}$ in Eq. 3.6 is the unitary transform of the energy difference denominator $\frac{1}{E_{c,\mathbf{k}}-E_{v,\mathbf{k}+\mathbf{q}}}$ (which is a positive definite quantity), $F_{a',b',\mathbf{R}';a,b,\mathbf{R}}$ is also a positive-definite matrix. We can compactify and rewrite Eq. (3.4) via the inner product of M with itself through F, $M^\dagger \cdot F \cdot M$, as

$$\epsilon = 1 + \frac{16\pi}{V} \cdot \frac{1}{|q|^2} \cdot M^\dagger \cdot F \cdot M \tag{3.7}$$

where we have compactified the indexing of the vector M_l and the matrix F_{lm} using collective indices $l = (a, b, \mathbf{R})$. The Fourier-transform nature of F indicates that it is diagonally dominant (i.e., largest when $\mathbf{R} = \mathbf{R}'$) so that as we add longer $\mathbf{R}$ to the sum to achieve convergence, we can expect the convergence to be monotonically increasing since we are adding more contributions from of a positive-definite matrix. We will build on this idea below to understand the spatial locality of dielectric constant in the Wannier basis (detailed in Secs. 3.5-3.8).

As will become evident below, the RPA approach to computing dielectric and photoelastic response is not as numerically accurate as DFPT; the RPA is missing a number of physical effects including local field corrections as well as the effects of exchange and correla-

	DFPT (this work)	Prior first principle calculation	Experiment
Si (unstrained)			
ϵ	12.986	13.200 [43], 10.468 [42]	11.830 [55]
p_{11}	−0.101	−0.098 [43], −0.111 [42]	−0.094 [55]
p_{12}	0.010	0.007 [43], 0.020 [42]	0.017 [55]
p_{44}	−0.050	−0.046 [43], −0.056 [42]	−0.051 [55]
Si (2.0% uniaxial strain along x)			
ϵ	13.356	-	-
p_{11}	−0.113	-	-
p_{12}	−0.010	-	-
Diamond			
ϵ	5.801	5.668 [42]	5.819 [56]
p_{11}	−0.263 (−0.262)	−0.264 [42]	−0.248 [57]
p_{12}	0.061 (0.063)	0.076 [42]	0.044 [57]
NaCl			
ϵ	2.508	2.615 [42]	2.380 [58]
p_{11}	0.058 (0.055)	0.077 [42]	0.115 [59]
p_{12}	0.153 (0.153)	0.157 [42]	0.161 [59]
MgO			
ϵ	3.127	3.160 [46], 3.077 [42]	3.020 [60]
p_{11}	−0.299 (−0.301)	−0.310 [46], −0.218 [42]	−0.259 [60]
p_{12}	−0.042 (−0.041)	−0.050 [46], 0.013 [42]	−0.011 [60]

Table 3.1: Elasto-optic coefficients for bulk crystals (Si, diamond, NaCl, and MgO) obtained using DFPT. For Si, the results are provided for both equilibrium and strained lattices. For diamond, NaCl and MgO, the elasto-optic coefficients based on one-sided (unparenthesized) and two-sided (parenthesized) finite differences using 1% strain are tabulated.

tion on screening. However, the primary utility of the RPA lies in its simplicity in the form of an analytical formula that can then be used to derive a localized form *ab initio* for the dielectric response; in addition, the numerical results below show that the RPA approach is quantitative (for Si, diamond and MgO) or at least semi-quantitative (for NaCl) when computing photoelastic response.

3.4 DFPT

We begin by presenting computed results for the dielectric and elasto-optic tensors of bulk Si, diamond, NaCl, and MgO using DFPT which lay the groundwork for the results that we wish to understand using a more detailed analysis.

Cubic crystals, like the ones studied in this work, have only 3 independent components in elasto-optic tensor, namely, p_{11}, p_{12}, and p_{44}. Elasto-optic coefficients computed from

DFPT for these materials at the experimental lattice constant are reported in the first column of Table 3.1. We use a $12 \times 12 \times 12$ k-point grid (unless otherwise specified) for the calculations in this work. We impose uniaxial strain along the x direction on the bulk to compute p_{11} and p_{12} and off-diagonal shear strain (with e_{23} being the only non-zero component in the strain tensor) to compute p_{44}. For uniaxial strain, we move the atoms proportionally with strain. For off-diagonal e_{23} strain, we strain the unit cell first and then relax the atoms inside the strained cell. For silicon, for each independent deformation, we compute the inverse dielectric tensor for several different strain values and then interpolate them using third order polynomials (in strain) to obtain the elasto-optic tensor. Results are also benchmark against higher order polynomial interpolations (up to fifth order) and finite difference formulae to ensure numerical stability to within the quoted number of digits in Table 3.1. For diamond, NaCl, and MgO, only the elasto-optic responses related to uniaxial strain are computed. In these three materials, we compute the inverse dielectric tensor at equilibrium and 1% uniaxial strain along x-axis and use the finite difference formula to extract the p_{11} and p_{12} components. We have checked explicitly that 1% strain is small enough to give precise enough results for further analysis below: the table shows that using simple one-sided versus the higher order two-sided finite differencing makes very little difference for the computed p_{11} and p_{12} values.

From Table 3.1, we observe that our results for both the static dielectric constant and the elasto-optic tensor are in semi-quantitative agreement with experiments and prior first principles calculations except for MgO's p_{12} component from Ref. [42]. The effect of finite wavelength λ of the electric field on photoelasticity in MgO has been investigated by Erba and Dovesi [42] and is reported to change the sign of p_{12} when λ goes from 400 nm to 1400 nm. The experimental values of p_{12} for MgO are scattered: e.g., the measurement of Giardini and Poindexter [61] has a different sign of p_{12} compared to the other measurements [60,62]. The discrepancies of the sign of p_{12} reported from experiments also suggest that the accurate determination of p_{12} in MgO is also a non-trivial task and requires future work. Overall, we find that DFPT is a reliable tool for predicting or computing the elasto-optic tensor of solids. We also report the elasto-optic tensor for silicon in a strained configuration in Table 3.1. It is worth noting that one can tune the elasto-optic response of silicon

	DFPT	RPA (100 bands)	RPA (12 bands)	RPA (8 bands)
Si (unstrained)				
ϵ^{∞}	12.986	13.823	13.805	13.629
p_{11}	-0.101	-0.094	-0.094	-0.099
p_{12}	$+0.010$	$+0.008$	$+0.008$	$+0.010$
Si (2.0% uniaxial strain along x)				
p_{11}	-0.113	-0.106	-0.106	-0.111
p_{12}	-0.010	-0.011	-0.011	-0.010

Table 3.2: Elasto-optic coefficients for bulk Si obtained using the RPA compared with DFPT.

crystal by deformation. Interestingly, the p_{12} elasto-optic coefficient even changes sign from $+0.010$ to -0.010 when silicon is strained uniaxially by 2%. In addition, Table 3.1 also shows the intriguing fact that NaCl and MgO, which have the same crystal structure and similar chemical properties, have the opposite elasto-optic response in both p_{11} and p_{12} components. These surprises, found in both computations and experiments, provide further motivation for studying the microscopic basis of photoelasticity.

3.5 Silicon

3.5.1 RPA

We use the RPA formula Eq. (3.2) to compute the dielectric response of bulk Si using the same procedure as for DFPT. In our RPA calculations, we have only imposed uniaxial strain on the crystal and therefore have only computed the p_{11} and p_{12} components in Table 3.2. We can see from the tabulated data that the RPA provides p_{11} and p_{12} coefficients that are very close to the DFPT values. In addition, the RPA offers a simple mathematical expression (Eq. (3.3)) that allows us to do further analysis below. Table 3.2 shows that both the static dielectric constant and the elasto-optic tensor converge quickly with total number of bands. Using only 8 bands, i.e., 4 valence and 4 lowest conduction bands, the results are good enough to capture the main features of the elasto-optic response. In addition, 8 bands also represent the minimal sp^3 basis needed for a tight-binding model for bulk Si which allows further analysis of the photoelasticity.

To study the convergence of the dielectric response versus k sampling, we separate out

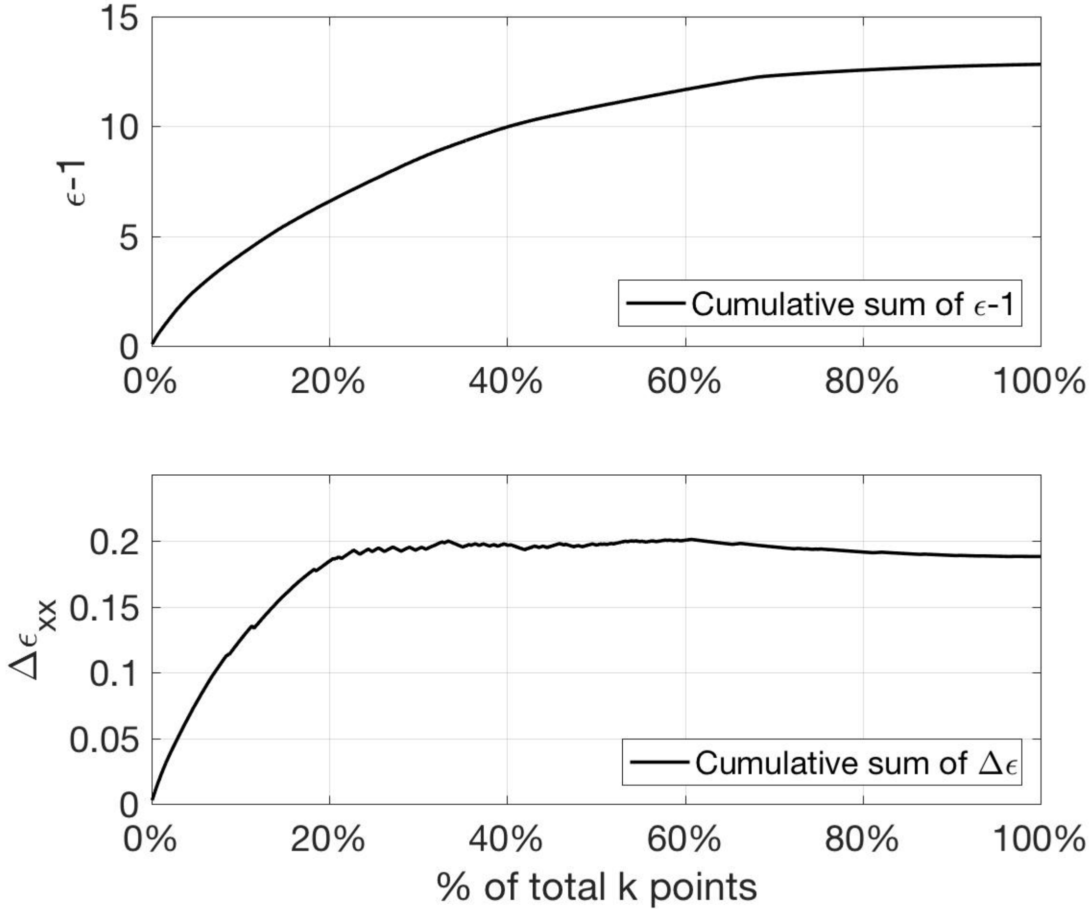

Figure 3.1: Cumulative sum of $D(\mathbf{k})$ and $\Delta D(\mathbf{k})$ with 1.0% uniaxial strain along x-axis in bulk Si. The horizontal axis is the fraction of k-points in the total $12 \times 12 \times 12 = 1728$ k-point mesh. In the upper plot of the cumulative sum of $D(\mathbf{k})$, the k-points are sorted by magnitude of $D(\mathbf{k})$ in decreasing order; in the lower plot of the cumulative sum of $\Delta D(\mathbf{k})$, which is the change in $D(\mathbf{k})$ due to the imposed 1.0% strain along x-axis, the k-points are sorted by magnitude of $\Delta D(\mathbf{k})$ in decreasing order.

ϵ	$\Delta\epsilon_{xx}$	$\Delta\epsilon_{xx}$ (fixed $\left\langle e^{-i\mathbf{q}\cdot\mathbf{r}}\right\rangle$)	$\Delta\epsilon_{xx}$ (fixed $E_{n,\mathbf{k}}$)
13.823	0.188	−0.027	0.083

Table 3.3: Dielectric constant for bulk Si using RPA. The first and second columns are the dielectric constant at equilibrium and its change with 1% uniaxial strain along the x-axis. In the third and fourth columns, $\Delta\epsilon_{xx}$ is computed by calculating the dielectric constant at the strained configuration with either the dipole matrix elements $\left\langle \psi_{c,\mathbf{k}} \left| e^{-i\mathbf{q}\cdot\mathbf{r}} \right| \psi_{v,\mathbf{k+q}} \right\rangle$ or eigenenergies $E_{n,\mathbf{k}}$ in Eq. (3.2) fixed to their equilibrium values.

the contribution to ϵ from each k-point:

$$\epsilon = 1 + \sum_{\mathbf{k}} D(\mathbf{k}) \tag{3.8}$$

where

$$D(\mathbf{k}) = \frac{16\pi}{V} \cdot \frac{1}{|q|^2} \sum_{c,v} \frac{\left|\left\langle \psi_{c,\mathbf{k}} \left| e^{-i\mathbf{q}\cdot\mathbf{r}} \right| \psi_{v,\mathbf{k+q}} \right\rangle\right|^2}{E_{c,\mathbf{k}} - E_{v,\mathbf{k+q}}} \tag{3.9}$$

in Eq. (3.2) is a delocalized quantity in momentum space: we can see from Figure 3.1 that the cumulative sum of $D(\mathbf{k})$ slowly converges to $\epsilon - 1$, meaning that one cannot single out a small subset of k-points that can account for most of the contribution to dielectric response. Figure 3.1 also shows that the change of dielectric constant $\Delta\epsilon$ due to strain is somewhat more localized in k-space than ϵ, but we still need a significant fraction of the total number of k-points to converge the cumulative sum of $\Delta D(\mathbf{k})$.

We find that the changes of dipole matrix elements $\left\langle e^{-i\mathbf{q}\cdot\mathbf{r}}\right\rangle$ with strain plays a more important role than the changes of Bloch eigenergies $E_{n,\mathbf{k}}$ in determining a material's photoelasticity. We can separate the impacts of these two factors in this way: we compute the dielectric constant ϵ_{xx} at strained configuration using Eq. ((3.4)) with either the dipole matrix elements $\left\langle \psi_{c,\mathbf{k}} \left| e^{-i\mathbf{q}\cdot\mathbf{r}} \right| \psi_{v,\mathbf{k+q}} \right\rangle$ or eigenenergies $E_{n,\mathbf{k}}$ fixed at their equilibrium values. Table 3.3 shows that the change of dielectric constant in Si is dominated by the dipole matrix elements rather than the eigenenergies. In fact, evaluating the dielectric constant for strained silicon while keeping the $\left\langle e^{-i\mathbf{q}\cdot\mathbf{r}}\right\rangle$ at the equilibrium value will give a change of dielectric response $\Delta\epsilon_{xx}$ in the wrong direction. This also agrees with Detraux and Gonze's assessment about the influence of the deformation potential (i.e., the change of electronic eigenenergies with lattice deformation) on the photoelasticity [63]. These observations warrant our continued investigations of elasto-optic response while focusing on the role of the

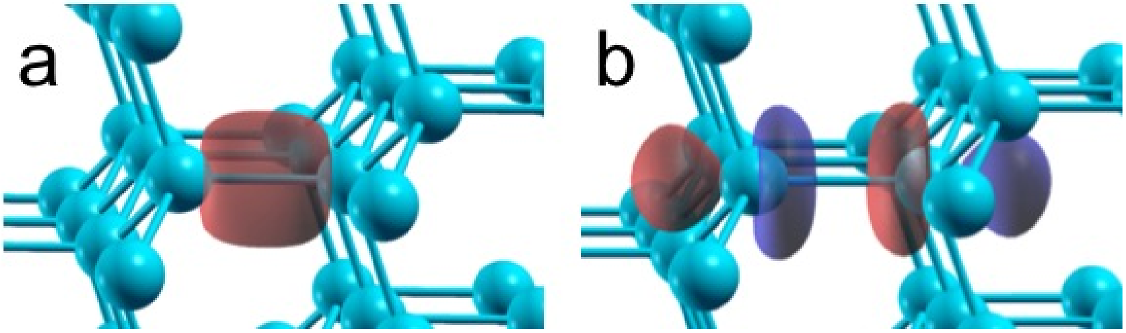

Figure 3.2: Wannier functions in bulk Si: (a) bonding and (b) antibonding. Red and blue correspond to positive and negative value in these isosurface plots, respectively. These isosurface plots demonstrate that the bonding and antibonding Maximally Localized Wannier functions are localized in real-space about the center of a Si-Si bond.

dipole transition matrix elements.

While the delocalization of the dielectric response in k-space is not helpful, it does point to a possible path forward. The adequacy of 8 energy bands combined with the delocalized nature of dielectric response in k-space strongly suggests that using a basis set localized in real-space may be more fruitful for understanding the photoelasticity of Si.

3.5.2 Wannier analysis & unexpected convergence behavior

We begin by generating 4 bonding and 4 antibonding Wannier functions for each 2-atom primitive cell in bulk Si. These Wannier functions come in pairs: each pair consists of a bonding and an antibonding Wannier function centered on the same chemical bond between two nearest-neighbor silicon atoms. (The bonding/antibonding pair on a bond are physically identical to those on other bonds by appropriate translations and rotations.) Figure 3.2 shows one bonding/antibonding pair. The description of the electronic structure given by these Wannier functions is consistent with the localized chemical picture where two sp^3 hybrid orbitals from neighboring silicon atoms overlap and form a chemical bond. The interpolated band structure (Figure 3.3) using these Wannier functions shows that they reproduce the DFT bands accurately for both valence and conduction bands around the Fermi energy.

We compute the dielectric tensor of bulk Si in the Wannier function basis using Eq. 3.4 for bulk Si at equilibrium and with 1% uniaxial strain and 1% shear strain. Table 3.4 shows

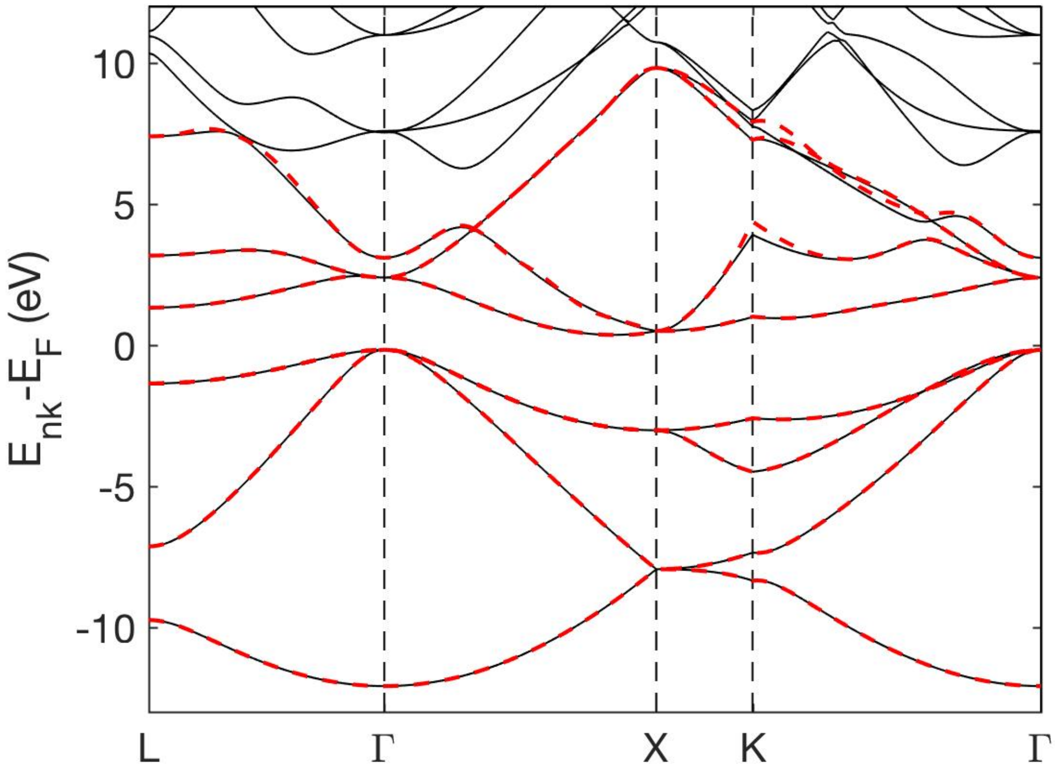

Figure 3.3: Band structure of bulk Si. Black solid lines are the DFT-LDA bands; red dashed lines are the Wannier interpolated bands. Since the frozen window [27] ranges from below the valence band to a few eV above the Fermi energy, the valence and low-lying conduction bands are reproduced exactly; as shown in the text, the differences at higher energies only lead to small errors in the computed dielectric response in the Wannier basis.

	DFPT	RPA (100 bands)	RPA (12 bands)	RPA (8 bands)	Wannier
ϵ (0.0%)	12.985	13.823	13.805	13.629	13.553
$\Delta\epsilon_{xx}$ (1.0%)	0.178	0.188	0.188	0.194	0.199
$\Delta\epsilon_{yy}$ (1.0%)	-0.008	-0.006	-0.006	-0.008	-0.004
ϵ_{yz} (0.0%)	0.000	0.005	0.005	0.005	0.005
$\Delta\epsilon_{yz}$ (1.0%)	0.081	0.093	0.093	0.093	0.094

Table 3.4: The dielectric constant and its change with 1% uniaxial strain along x-axis (first three rows of the table) and the ϵ_{yz} component of dielectric tensor and its change with $e_{23} = 1\%$ shear strain (last two rows of the table) for Si. The results in the table are based on a $12 \times 12 \times 12$ grid and are obtained using DFPT, using the RPA with Bloch states from Eq. (3.2), and using Wannier functions from Eq. (3.4) (see Sec. 3.10 for the equations used to compute the full dielectric tensor).

that the Wannier function method with the 4 bonding and 4 antibonding orbitals agrees well with RPA results with 8 bands for both the dielectric constant and its change under uniaxial strain. The small differences between the 8-band RPA method and the Wannier method are a consequence of the disentanglement procedure used in building the antibonding Wannier functions: the disentanglement procedure selects the subspace of Bloch states that are "smoothest" across k-space [27] which is not equivalent to reproducing the 4 lowest energy-sorted conduction bands (see Figure 3.3). Our method for computing the full dielectric tensor is detailed in 3.10. The changes in components $\Delta\epsilon_{xx}$, $\Delta\epsilon_{yy}$, and $\Delta\epsilon_{yz}$ are shown in Table 3.4 since they are related directly to the computation of the p_{11}, p_{12}, and p_{44} photoelastic components. The small non-zero value of the ϵ_{yz} component at zero strain (equilibrium) is due to the fact that standard Monkhorst-Pack k grid used for the 2-atom primitive cell does not obey the full crystalline symmetry of Si (but the grid is dense enough to give only small numerical asymmetries).

Having established the sufficient accuracy of the Wannier method, we now analyze the spatial locality of the dielectric response of bulk Si using Wannier functions. We begin by investigating the decaying behavior of the Wannier dipole matrix element M (Eq. 3.5) as a function of distance (see Figure 3.4) with $\mathbf{q}$ aligned along x-axis. Figure 3.4 shows that the dipole matrix element has a rather "long tail", i.e., the magnitude is still non-negligible even when the centers of bonding and antibonding Wannier functions are many bond lengths apart. This means the the dielectric response in the Wannier basis has relatively long-ranged behavior, which is unexpected since Maximally Localized Wannier Functions are expected to be quite compact. We infer that the dipole matrix element becomes longer-ranged than the Wannier functions themselves due to the long-ranged nature of the position operator: the lowest order contribution for small $\mathbf{q}$ is $e^{-i\mathbf{q}\cdot\mathbf{r}} \approx 1 - i\mathbf{q}\cdot\mathbf{r}$, and due to the orthogonality of Wannier functions, $M \approx -\langle W_{a,\mathbf{R}} | i\mathbf{q}\cdot\mathbf{r} | W_{b,\mathbf{0}}\rangle$ which highlights how the long-ranged position operator $\mathbf{r}$ can give rise to long-ranged dipole matrix elements.

Such long-ranged behavior also manifests itself in the convergence of the dielectric constant with increasingly dense k-point meshes or equivalently larger real-space supercells. In k-space, a periodic supercell is represented by a uniform Born-von Karman k-point sampling of the Brillouin zone; in real-space, the supercell is represented by a large volume of material on which periodic boundary conditions are imposed. The diagonal entries of Table 3.5 represent a "standard" convergence calculation: we increase the size of the supercell, generate Wannier functions, and compute the dielectric response using the full supercell's worth of data. We can see that the ϵ_{xx} is not quite converged even for a $12 \times 12 \times 12$ supercell. In the k-space view, slow convergence with the density of the k-point sampling represents a "long-ranged" quantity. However, based on the equivalence of k-point mesh in the RPA method (Eq. (3.2)) and the size of supercell in the Wannier method (Eq. (3.4)), the monotonically decreasing dielectric constant (see blue dashed line in Figure 3.5) with increasing k-point mesh is counterintuitive since, as discussed in Sec. 3.3, we might expect that by including dipole transitions between Wannier functions further apart in a larger supercell, the dielectric constant should increase.

To shed further light on this unexpected convergence behavior, we employ Eq. 3.4 in a different manner as a "constrained sum". We generate Wannier functions for a large supercell but constrain the sum over lattice vectors $\mathbf{R}, \mathbf{R}'$ in Eq. (3.4) to range over a smaller subset centered on the origin that represents a smaller supercell. In this way, we can disentangle the change of the spatial form of the Wannier functions themselves with supercell size from the actual locality of the dipole matrix elements and energy denominators ($M_{a,b,\mathbf{R}}$ and $F_{a',b',\mathbf{R}';a,b,\mathbf{R}}$ in Eq. (3.4)). Namely, we only include the dipole matrix elements $M_{a,b,\mathbf{R}}$ (Eq. 3.5) whose bonding Wannier function $W_{b,\mathbf{0}}$ and antibonding Wannier function $W_{a,\mathbf{R}}$ both fall inside the smaller $x \times x \times x$ supercell centered around origin. For example, in the last column of Table 3.5, we vary x from 6 to 12, and the dielectric constant convergences in an increasing manner (See Figure 3.5). Similar convergence is also observed in the $8 \times 8 \times 8$ and $10 \times 10 \times 10$ columns in Table 3.5. Despite the more sensible convergence behavior, we confirm the long-ranged nature of the dielectric response within this "constrained sum" method. In fact, for Wannier functions generated in $12 \times 12 \times 12$ supercell, including the dipole transitions between Wannier functions on the same, nearest-neighbor, and second nearest-neighbor chemical bonds together only accounts for 50% of the total dielectric response when using the subset $x = 2$ (see last column of Table 3.5).

The above results provide the following physical picture. For a fixed sets of Wannier functions generated in a large supercell, one sees sensible convergence from below for the dielectric response upon adding more distant contribution in real-space: this is physically what we expect for a localized real-space representation. Hence, the unexpected behavior of dielectric response versus supercell size in the "standard" computations must be due to the Wannier functions themselves changing as they are generated in progressively larger supercells. In fact, the Wannier functions generated in smaller supercells must be longer ranged so that they lead to overestimation of the dipole elements and the dielectric response. This behavior also makes sense: Wannier functions generated in a periodic supercell are necessarily periodic as well because of the overall Born-von Karman periodic boundary condition; when the supercell is not large enough, the periodized Wannier functions will include the periodic images of the true (infinite supercell) Wannier functions in the tail regions summed from adjacent supercells. While the errors in the Wannier function tails are small, they are sizable enough to lead to the misleading convergence with supercell size. Figure 3.4 shows how the $6 \times 6 \times 6$ and $12 \times 12 \times 12$ supercells differ quantitatively for the same dipole matrix elements M due to the Wannier functions themselves changing with supercell size. We conclude that the artificial periodicity of the supercell Wannier functions is the root of the convergence behavior in the "standard" calculation.

We build on the constrained sum method to further analyze the spatial locality of the change of the dielectric constant with strain. First, the Wannier dipole transition matrix elements can be spatially grouped into shells: each shell includes the dipole transitions that are related to each other through crystal symmetry. Hence, dipole transitions belonging to the same shell have the same distance between the bonding and antibonding Wannier

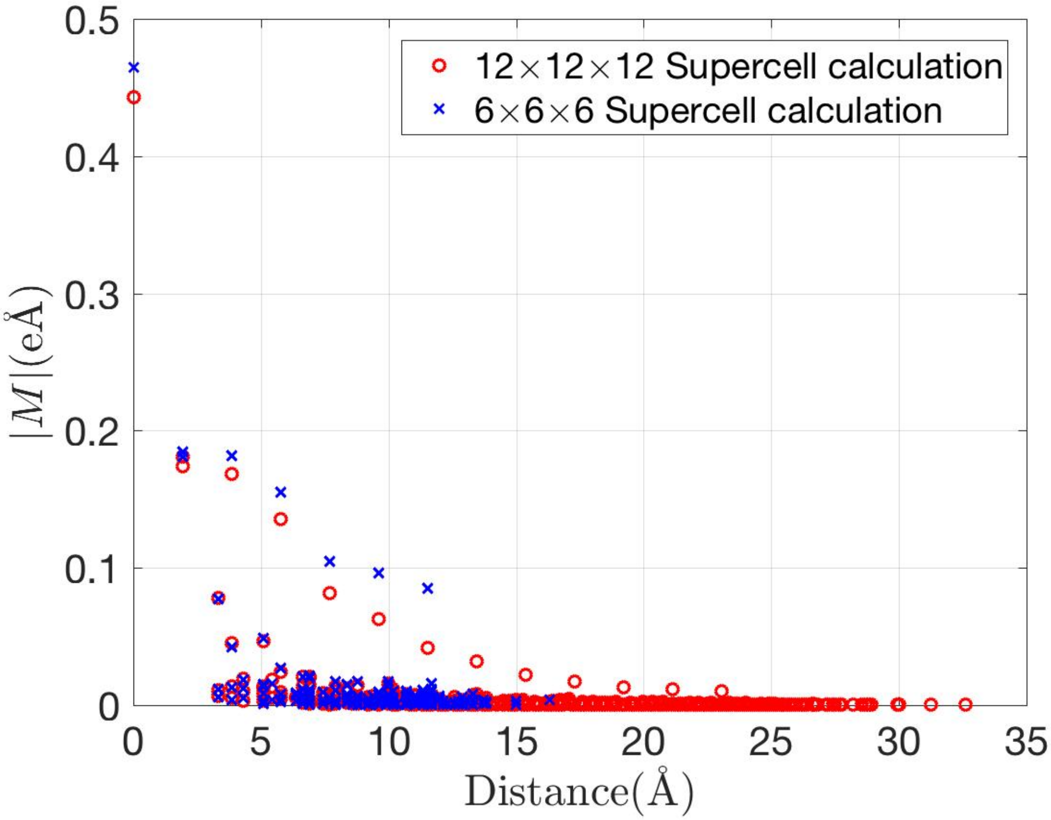

Figure 3.4: Magnitude of the Wannier dipole matrix elements $|M|$ (Eq. 3.5) versus distance between Wannier functions. Wave vector $\mathbf{q}$ is aligned with x-axis. The distance is between the center of $W_{b,\mathbf{0}}$ (the bonding Wannier function in the home unit cell) and $W_{a,\mathbf{R}}$ (the antibonding Wannier function $\mathbf{R}$ lattice vectors away). For reference, the bond length between nearest-neighbor Si atoms is 2.35 Å. The two sets of results are for Wannier functions generated in two different supercells.

		Size of supercell used to generate Wannier functions			
		$6 \times 6 \times 6$	$8 \times 8 \times 8$	$10 \times 10 \times 10$	$12 \times 12 \times 12$
Subset of Wannier functions used	$2 \times 2 \times 2$	5.94(0.10)	5.53(0.08)	5.43(0.08)	5.41(0.08)
	$4 \times 4 \times 4$	11.89(0.19)	10.62(0.15)	10.34(0.16)	10.27(0.16)
	$6 \times 6 \times 6$	16.87(0.23)	13.11(0.17)	12.55(0.19)	12.43(0.18)
	$8 \times 8 \times 8$	-	14.59(0.18)	13.36(0.19)	13.16(0.19)
	$10 \times 10 \times 10$	-	-	13.81(0.20)	13.41(0.20)
	$12 \times 12 \times 12$	-	-	-	13.55(0.20)

Table 3.5: Convergence of dielectric constant in bulk Si using the Wannier RPA method. The columns represent the size of supercell used to generate the Wannier functions. The rows represent the subset of the supercell whose dipole transition are summed up to obtain the dielectric constant. The numbers without parentheses are the dielectric constant ϵ_{xx} of bulk Si at equilibrium; the numbers in parentheses are the change of dielectric constant $\Delta\epsilon_{xx} = \epsilon_{xx}(1.0\%) - \epsilon_{xx}(0.0\%)$ of Si strained uniaxially by 1.0% along the x-axis.

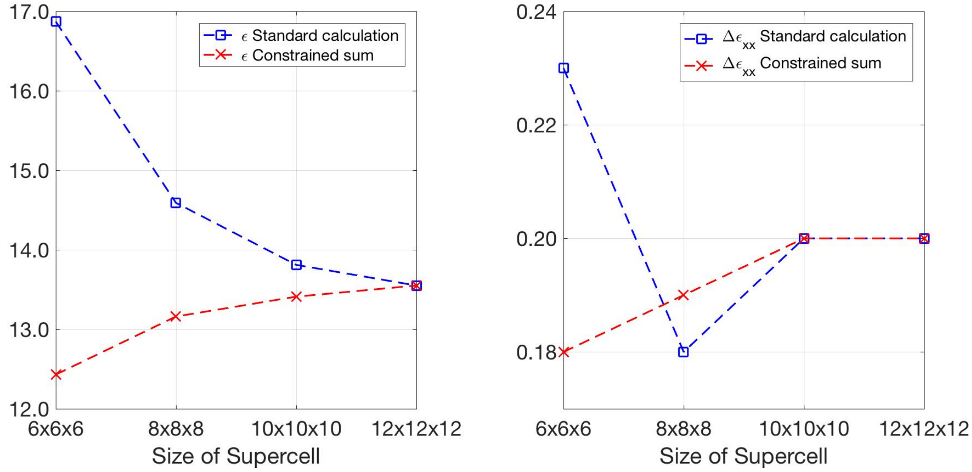

Figure 3.5: Convergence of ϵ_{xx} and $\Delta\epsilon_{xx}$ with 1.0% uniaxial strain along x-axis in bulk Si using the Wannier function method.

functions, and we sort them by distance. We focus on the first three shells of the dipole transitions with largest matrix element from Figure 3.4 and show them graphically in Figure 3.6. Table 3.6 displays the matrix elements from the three shells and how they change with applied strain. Table 3.6 shows that increasing distance reduces the dipole transition strength, but the rate of decrease is modest: matrix elements between the same chemical bond, nearest-neighbor bonds, and second nearest-neighbor bonds still have the same order of magnitude. The change of the matrix elements with strain is more complicated: Table 3.6 shows that $|M|$ can either become larger or smaller depending on the type of imposed strain.

Now we analyze the locality of the change of the dielectric constant using the constrained sum method. Table 3.6 shows that all three shells are required to reach a reasonable convergence of $\Delta\epsilon_{xx}$ for 1% uniaxial strain along the x or y axis where $\Delta\epsilon_{xx} = \epsilon_{xx}(\text{strained}) - \epsilon_{xx}(\text{equilibrium})$. When the strain is along the x-axis, the change is directly proportional to the elasto-optic coefficient p_{11}, while strain along the y-axis describes p_{12}; the data for $\Delta\epsilon_{yz}$ is generated by 1% shear strain and is proportional to p_{44}. Our conclusion is that the change in dielectric constant with strain is rather delocalized. First, the convergence with added shells is either slow (for strain along x) or non-monotonic (for strain along y where the sign of the cumulative sum changes twice between the second and third

Dipole transition matrix elements	$\lvert M\rvert$ (Å)			Cumulative contribution to $\Delta\epsilon_{xx}$		Cumulative contributi to $\Delta\epsilon_{yz}$
	0% strain	$e_{xx} = 1\%$	$e_{yy} = 1\%$	$e_{xx} = 1\%$	$e_{yy} = 1\%$	$e_{yz} = 1\%$
"1" → "1"	0.443	0.448	0.443	0.041	-9.4×10^{-3}	0.025
"1" → "2"	0.174	0.176	0.175	0.083	2.8×10^{-3}	0.048
"1" → "3"	0.169	0.171	0.168	0.152	-3.5×10^{-3}	0.039
All shells	-	-	-	0.199	-3.5×10^{-3}	0.094

Table 3.6: Three transition dipole matrix elements $|M|$ with largest magnitude and their changes with different strain are listed in the second to fifth columns; the shell indices in the first column are those described in Figure 3.6. The wave vector $\mathbf{q}$ is along the x-axis for the calculation of the matrix elements, so that $|M|$ is the magnitude of dipole transition vector projected on the x-axis. In the last three columns, each row reports the cumulative contribution from the listed and preceding shells.

shell). Second, although transitions on the same bond are the strongest, only including them does not provide quantitative accuracy. Third, while reasonable accuracy is obtained by summing up to the third shell of transitions, this involves a sum over nineteen independent transitions and, in our mind, is too complicated a physical picture to give insight for materials design in terms of photoelasticity. Hence, while the dielectric and elasto-optic response are spatially localized in Si, the length scale of the locality is too large and involves too many transitions for us to extract simple rules of thumb or provide simple guidance for designing elasto-optic response.

We now build upon this analysis protocol to analyze other materials with a primary focus on the degree of locality of the elasto-optic effect.

3.6 Diamond

Diamond, which shares the same crystal structure as silicon, serves as another example of a tetrahedral covalent insulator for our study of photoelasticity. The larger band gap and more localized atomic orbitals of diamond compared to Si give us hope that the elasto-optic response may be shorter ranged. We use the same methodology as we do for bulk Si.

The Wannier functions for bulk diamond are generated in a very similar manner as in Si, i.e., there are 4 bonding-antibonding Wannier function pairs per 2-atom unit cell. Each pair consists of a bonding and an antibonding orbital centered around the same chemical bond between the neighboring carbon atoms. The computed band structure (see Figure 3.7)

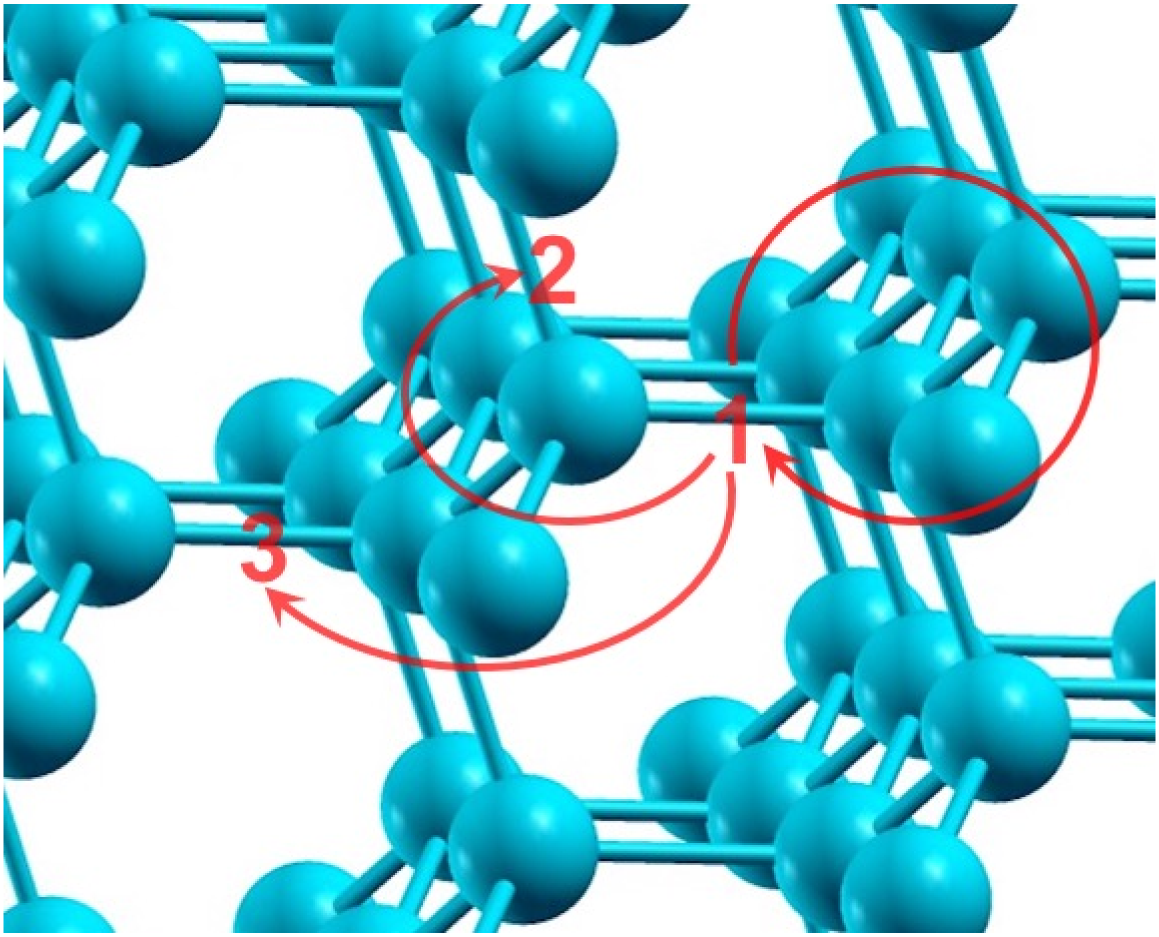

Figure 3.6: The three shells of dipole transitions with the largest matrix elements in Wannier basis visualized in real space. Arrows are drawn from a bonding Wannier function (the initial state) to an antibonding Wannier function (the final state) of the dipole transition matrix elements. Given that the initial state is the bonding Wannier function on bond "1", the arrow "1" → "1" illustrates the dipole transitions to the same bond (there is only one such type of transition per chemical bond), the arrow "1" → "2" illustrates the dipole transitions to the nearest-neighbor bonds (there are six such transitions per chemical bond), and the arrow "1" → "3" illustrates the dipole transitions to the second nearest-neighbor bonds that are parallel to bond "1" (there are six such transitions per chemical bond).

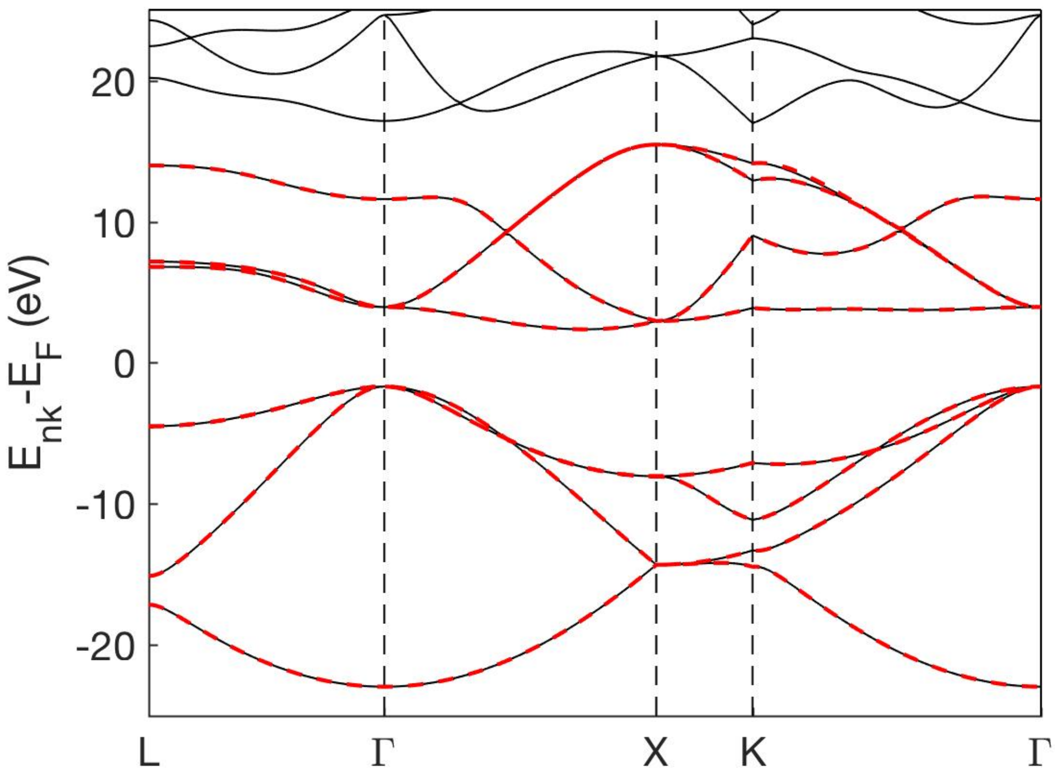

Figure 3.7: Band structure of bulk diamond. Black solid lines are the DFT-LDA bands; red dashed lines are the Wannier interpolated bands. Both of the 4 valence and 4 lowest conduction bands form an isolated group of bands.

shows that the 4 lowest conduction bands of diamond form an isolated group. Therefore the Wannier basis can describe both the valence bands and lowest 4 conduction bands exactly in diamond as shown in Figure 3.7.

The dielectric constant for bulk diamond at equilibrium and its change with 1% strain along x-axis are computed using Eq. 3.4. Table 3.7 shows that the Wannier function method with a basis of 4 bonding and 4 antibonding agrees well with RPA method with only 8 bands included. Table 3.7 also demonstrates the qualitative similarity of photoelasticity between bulk diamond and bulk Si. Namely, the dielectric constant changes in the same direction with 1% strain along x in both materials..

To further examine the spatial locality of diamond's dielectric response and to compare it with that of Si, the dipole transition matrix elements $|M|$ are computed using the Wannier

	DFPT	RPA (100 bands)	RPA (8 bands)	Wannier
$\epsilon(0.0\%)$	5.801	5.964	5.746	5.735
$\Delta\epsilon_{xx}(1.0\%)$	0.090	0.094	0.096	0.098
$\Delta\epsilon_{yy}(1.0\%)$	-0.020	-0.020	-0.023	-0.022

Table 3.7: Bulk diamond dielectric constant and its change with 1% uniaxial strain along x-axis obtained using DFPT, RPA with Bloch basis and with Wannier basis. The methods used are the same as Table 3.4. The results in the table are based on a $12 \times 12 \times 12$ k grid.

basis. Figure 3.8 shows that, as expected, $|M|$ in diamond decays faster as a function of distance than Si. In addition, $6\times6\times6$ and $12\times12\times12$ supercells generate Wannier functions giving dipole transitions that are much closer in magnitude compared to Si (compare Figures 3.4 and 3.8). Based on the physical picture developed above for bulk Si, this means that the Wannier functions in bulk diamond are more compact than in bulk Si, as expected due to diamond's wider band gap [25]. The superposition of the periodic images of the Wannier functions in the $6 \times 6 \times 6$ supercell still leads to dipole matrix elements that are quite accurate compared to those of the larger $12 \times 12 \times 12$ supercell. This indicates that the Wannier functions with their exponentially decaying tails are well contained in the $6\times6\times6$ supercell in diamond.

The compactness of the Wannier functions in diamond is also evident in the convergence calculation of the dielectric constant. The bulk diamond dielectric constant converges faster in both of the "standard" and "constrained sum" convergence calculation comparing to bulk Si (see Figures 3.5 and 3.9). The increasing behavior of the dielectric constant (detailed above in the bulk Si results) is also observed using the "constrained sum" method (see the columns of Table 3.8 and Figure 3.9 left panel). However, the change of the dielectric constant ϵ_{xx} along x-axis in diamond converges at a similar rate using the "constrained sum" method to Si. In fact, in both materials, the dipole transitions between the bonding and antibonding orbitals whose distance is within a $4 \times 4 \times 4$ supercell account for $80\% \sim 90\%$ of the change in ϵ_{xx} due to uniaxial strain along the x-axis.

Finally, just like Si, a "shell" analysis can be performed for bulk diamond. The diamond dipole transitions are first grouped into shells that are defined in exactly the same way as bulk Si. Then, we identify the three different near-neighbor shells of dipole transitions that are largest in magnitude and also give the largest contribution to the dielectric constant

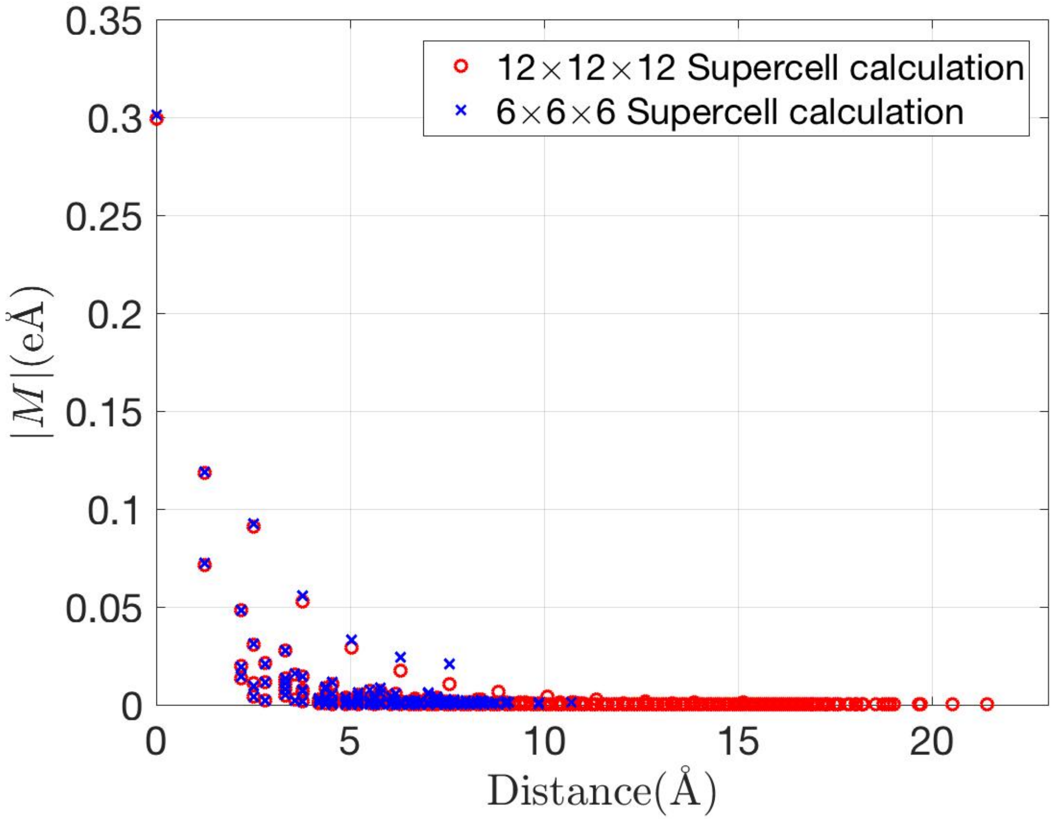

Figure 3.8: Magnitude of the bulk diamond Wannier dipole matrix elements $|M|$ (Eq. 3.5) versus distance between Wannier functions. Wave vector $\mathbf{q}$ is aligned with x-axis. The distance is between the center of $W_{b,\mathbf{0}}$ (the bonding Wannier function in the home unit cell) and $W_{a,\mathbf{R}}$ (the antibonding Wannier function $\mathbf{R}$ lattice vectors away). For reference, the bond length between nearest-neighbor C atoms is 1.55 Å. The two sets of results are for Wannier functions generated in two different supercells.

		Size of supercell used to generate Wannier functions			
		$6\times6\times6$	$8\times8\times8$	$10\times10\times10$	$12\times12\times12$
Subset of Wannier functions used	$2\times2\times2$	3.38(0.05)	3.34(0.05)	3.34(0.05)	3.33(0.05)
	$4\times4\times4$	5.38(0.09)	5.25(0.08)	5.23(0.09)	5.23(0.09)
	$6\times6\times6$	6.04(0.10)	5.67(0.09)	5.64(0.09)	5.64(0.09)
	$8\times8\times8$		5.79(0.10)	5.72(0.10)	5.71(0.10)
	$10\times10\times10$			5.75(0.10)	5.73(0.10)
	$12\times12\times12$			-	5.74(0.10)

Table 3.8: Convergence of dielectric constant in bulk diamond using the Wannier RPA method. The table is in the same nomenclature as Table 3.5.

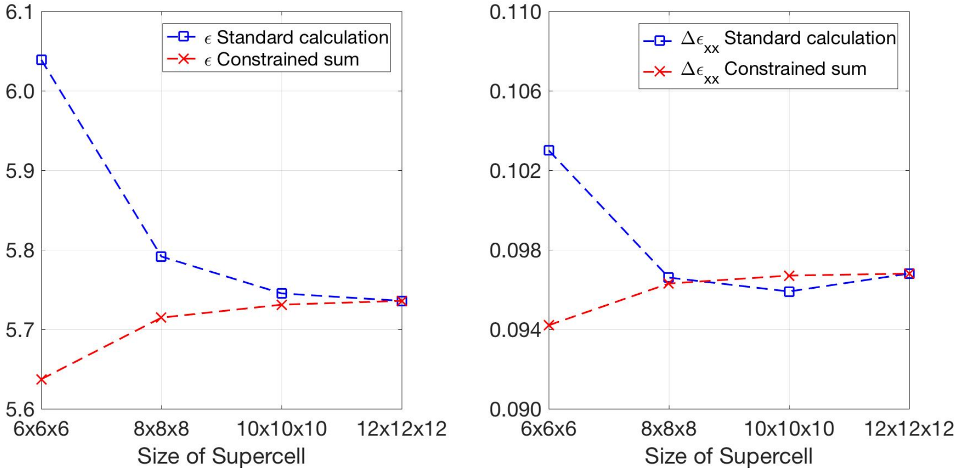

Figure 3.9: Convergence of ϵ_{xx} and $\Delta\epsilon_{xx}$ with 1.0% uniaxial strain along x-axis in bulk diamond using the Wannier function method. The figure adopts the same notation as Figure 3.5.

Dipole transition matrix elements	$\lvert M \rvert$ (Å) 0% strain	1% x-strain	1% y-strain	Cumulative contribution to $\Delta\epsilon_{xx}$ 1% x-strain	1% y-strain
"1" → "1"	0.299	0.303	0.299	0.032	-6.7×10^{-3}
"1" → "2"	0.119	0.118	0.119	0.052	-5.5×10^{-3}
"1" → "3"	0.091	0.092	0.090	0.078	-11.9×10^{-3}
All shells	-	-	-	0.098	-22.2×10^{-3}

Table 3.9: Three transition dipole matrix elements $|M|$ with largest magnitude and their changes with strain in bulk diamond are listed in the second to fourth column. The shells (in the first column) are indexed the same as bulk Si (see Table 3.6 and Figure 3.6). Last two columns of the table reports the cumulative contribution to $\Delta\epsilon_{xx}$ from the listed shells. The table follows the same notation as Table 3.6.

(see Table 3.9). The cumulative contribution to the change of the dielectric constant using these three shells are also computed in Table 3.9. Though the Wannier functions are more compact in diamond than Si, our characterization of the spatial locality of the elasto-optic effect in diamond is to a great extent the same as silicon: one needs to sum up at least three shells' contribution to achieve reasonable accuracy for photoelasticity in bulk diamond.

3.7 NaCl

The NaCl crystal serves as the first example of an ionic material for our study. It is a rocksalt structured, electronically closed-shell band insulator with the valence electrons filling bands of primarily Cl character. We use this chemical description to construct atom-centered Wannier functions for the valence bands, making one Wannier function have Cl s character and three Wannier functions have Cl p character. These four occupied Wannier functions can accommodate all the eight valence electrons (from both spin channels) in the two-atom *fcc* primitive unit cell. Though the conduction band edge is expected to have primarily Na $3s$ atomic orbital character, a quantitative description of the low-lying conduction bands is more complex. After examining the atomic projections of the low-lying conduction bands, we have decided to use one s-like and three p-like orbitals centered on the Na and five d-like orbitals centered on the Cl to construct the unoccupied Wannier basis. Figure 3.10 illustrates these occupied and unoccupied Wannier functions. The 4 occupied and 9 unoccupied Wannier functions per unit cell can span the Hilbert space of the valence and lower part of the conduction bands. The band interpolation using the Wannier basis and its comparison to the DFT bands are shown in Figure 3.11. The valence and five lowest conduction DFT bands are well reproduced by the Wannier basis but the four highest Wannier-derived conduction bands deviate from the corresponding DFT bands. Such discrepancy is normal and unavoidable: first, the Wannier disentanglement procedure hybridizes DFT bands to achieve the "smoothest"subspace across the Brillouin zone which tends to lead to narrower Wannier bands; second, higher conduction bands contain larger plane wave (free electron) character which becomes progressively harder to describe with any localized basis set leading to further discrepancies. We also point out that the choice of the Wannier representation of the conduction bands is not unique. Other sets of unoccupied Wannier orbitals, e.g., the set of five d states on the Cl and one s state on Na or the set of five d states on Cl and two s states on the two interstitial sites half way between the Na and Cl along [111] direction, can interpolate at least the five lowest conduction bands very well. Our choice of the unoccupied Wannier functions gives the best numerical agreement for ϵ and $\Delta\epsilon$ between the RPA and Wannier methods, but the overall nature of the locality of photoelasticity in NaCl does not depend on which one of these Wannier representations is used.

Table 3.10 shows the comparison between the computed values of the dielectric constant and its change with 1% uniaxial strain using different methods. As noted above, the Wannier method agrees well with the RPA results using either a converged number of bands or

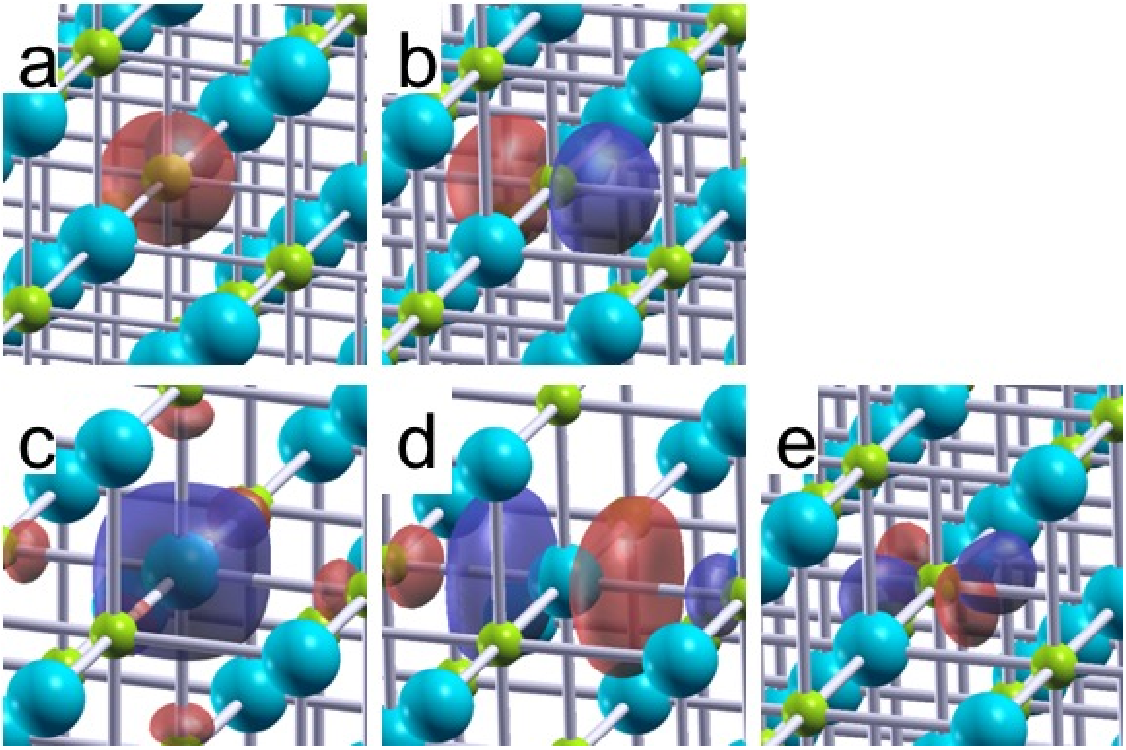

Figure 3.10: Wannier functions in NaCl: occupied Wannier functions (a) Cl *s* orbital and (b) one of Cl *p* orbitals, unoccupied Wannier functions (c) Na *s* orbital, (d) one of Na *p* orbitals, (e) one of Cl *d* orbitals. Red and blue correspond to positive and negative value in these isosurface plots, respectively. These plots illustrate the atomic centered Maximally Localized Wannier Functions. Color scheme of the atoms: Na: cyan, Cl: green.

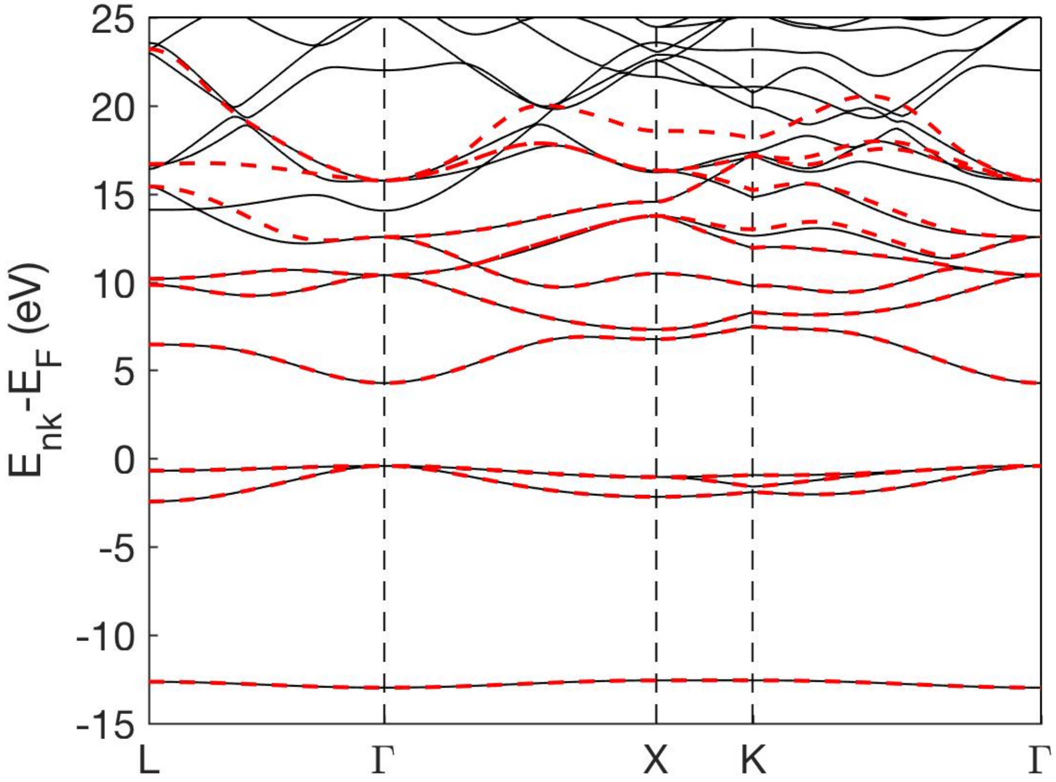

Figure 3.11: Band structure of bulk rocksalt NaCl. Black solid lines are the DFT-LDA bands; red dashed lines are the Wannier interpolated bands. The valence Wannier bands are spanned by *sp*-like Wannier functions centered on Cl. The conduction Wannier bands are spanned by *sp*-like Wannier functions centered on Na and *d*-like Wannier functions centered on Cl.

	DFPT	RPA (100 bands)	RPA (13 bands)	Wannier
$\epsilon(0.0\%)$	2.51	2.81	2.77	2.79
$\Delta\epsilon_{xx}(1.0\%)$	-3.7×10^{-3}	-5.4×10^{-3}	-6.3×10^{-3}	-5.6×10^{-3}
$\Delta\epsilon_{yy}(1.0\%)$	-9.6×10^{-3}	-10.5×10^{-3}	-11.1×10^{-3}	-10.7×10^{-3}

Table 3.10: Bulk rocksalt NaCl dielectric constant and its change with 1% uniaxial strain along x-axis obtained using DFPT, RPA with Bloch states in a plane wave basis and with the Wannier basis. These methods are the same as those in Table 3.4 and Table 3.7. The results in the table are based on a $12 \times 12 \times 12$ k grid.

13 bands which is equal to the total number of orbitals in the Wannier basis. However, NaCl shows a qualitatively different elasto-optic response from the two tetrahedral covalent materials. The dielectric constant in NaCl decreases in the direction along which the tensile strain is applied opposite to the behavior of Si and diamond. The order of magnitude of $\Delta\epsilon_{xx}$ is also much smaller in NaCl than in Si and diamond. In fact, the change of ϵ is smaller in magnitude along the strain direction ($\Delta\epsilon_{xx}$) than in the perpendicular direction ($\Delta\epsilon_{yy}$).

Figure 3.12 shows that the magnitude of NaCl dipole transition matrix element $|M|$ is a very short-ranged function of the distance between Wannier function centers. In fact, $|M|$ drops to below 12% of its maximum magnitude when the occupied and unoccupied Wannier functions are further apart than the nearest neighbor Na-Cl distance. Furthermore, Wannier functions generated in the $6 \times 6 \times 6$ and the $12 \times 12 \times 12$ supercells virtually give the identical dipole matrix elements. Using the previous physical argument concerning Si and diamond, we conclude that the NaCl Wannier functions are quite compact, making the dipole transitions short-ranged between them.

The "standard" and "constrained sum" convergence results for the dielectric response are reported in Table 3.11 and Figure 3.13 for both ϵ and $\Delta\epsilon_{xx}$. As expected, the compactness of the NaCl Wannier functions leads to a rapid convergence of ϵ using both the "standard" and "constrained sum" methods. The change of the dielectric constant $\Delta\epsilon_{xx}$ also converges rapidly using the "constrained sum" method (see Figure 3.13), making the locality of the change of the dielectric constant evident. However, the right panel of Figure 3.13 shows that "standard" calculation of $\Delta\epsilon_{xx}$ converges more slowly versus supercell size, suggesting that subtle changes of the Wannier functions with strain can only be captured using the large

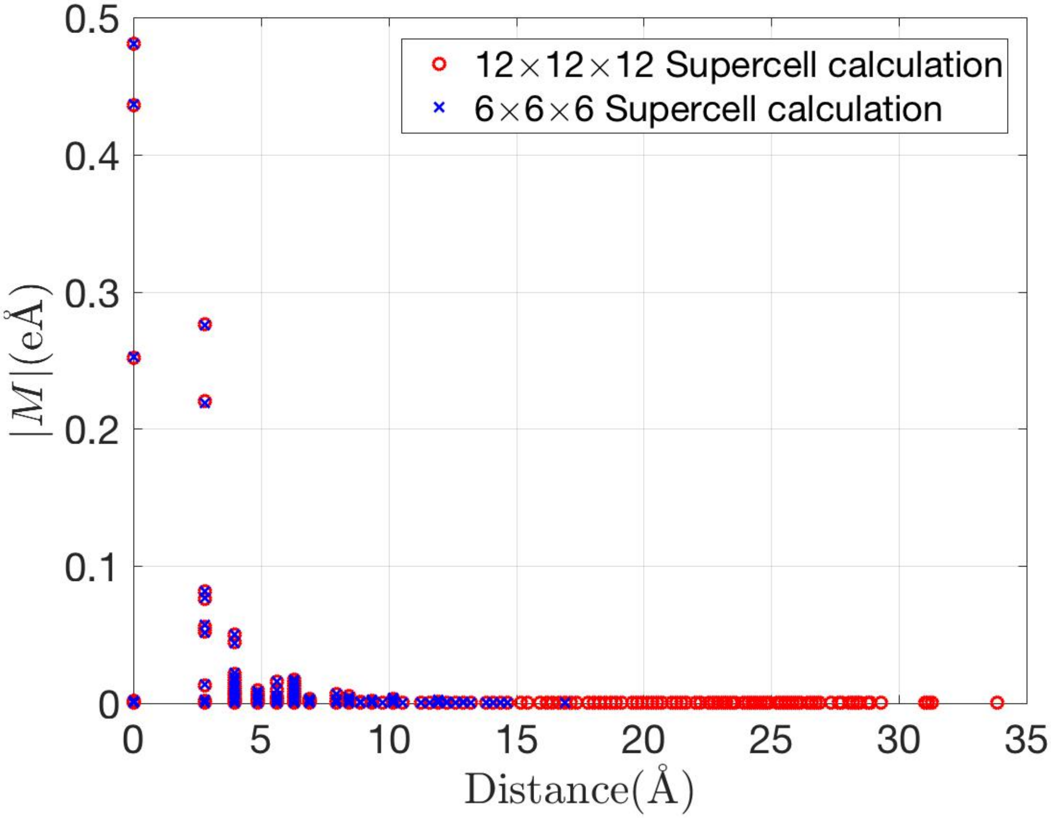

Figure 3.12: Magnitude of the bulk NaCl Wannier dipole matrix elements $|M|$ versus distance between Wannier functions. The notations are the same as Figure. 3.4. For reference, the distance between the nearest Na and Cl atoms is 2.82 Å.

		Size of supercell used to generate Wannier functic			
		$6 \times 6 \times 6$	$8 \times 8 \times 8$	$10 \times 10 \times 10$	
Subset of Wannier functions used	$2 \times 2 \times 2$	$2.16(-1.8 \times 10^{-3})$	$2.17(-2.7 \times 10^{-3})$	$2.17(-2.4 \times 10^{-3})$	2.
	$4 \times 4 \times 4$	$2.75(-3.5 \times 10^{-3})$	$2.75(-6.9 \times 10^{-3})$	$2.76(-5.7 \times 10^{-3})$	2.
	$6 \times 6 \times 6$	$2.79(-4.1 \times 10^{-3})$	$2.79(-7.3 \times 10^{-3})$	$2.79(-6.1 \times 10^{-3})$	2.
	$8 \times 8 \times 8$		$2.79(-7.4 \times 10^{-3})$	$2.79(-6.1 \times 10^{-3})$	2.
	$10 \times 10 \times 10$			$2.79(-6.1 \times 10^{-3})$	2.
	$12 \times 12 \times 12$				2.

Table 3.11: Convergence with supercell size of the dielectric constant and its strain dependence in bulk NaCl using the Wannier function method. This table uses the same nomenclature as Table. 3.5 and Table. 3.8.

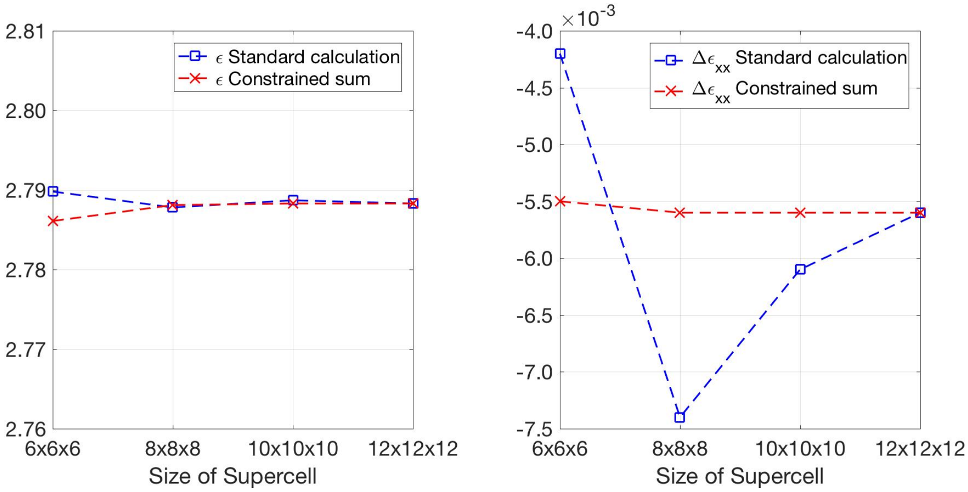

Figure 3.13: Convergence of ϵ_{xx} and $\Delta\epsilon_{xx}$ with 1.0% uniaxial strain along x-axis in bulk NaCl using the Wannier function method. The figure uses the same notations as Figure 3.5.

$12 \times 12 \times 12$ supercell. Therefore, the previous conclusion for locality in the elasto-optic response carries over from Si and diamond to NaCl: a large enough supercell is needed to generate the Wannier functions, and we should use the "constrained sum" method to sum up the local contributions in ϵ and $\Delta\epsilon$ in a predictable manner.

Last but not the least, the "shell" analysis can be performed for NaCl. Since the Wannier functions are atom-centered in NaCl, the shells can be labeled by the atomic sites between which the dipole transitions take place. The three shells contributing the largest magnitudes to both ϵ and $\Delta\epsilon$ are illustrated with arrows in Figure 3.14. The cumulative contributions to the change of the dielectric constant using these three shells are found in Table 3.12. Since each atomic site hosts more than one kind of Wannier functions in NaCl,

Dipole transition matrix elements	Cumulative contribution to $\Delta\epsilon_{xx}$ 1% x-strain	 1% y-strain
"1" → "1"	-1.9×10^{-3}	-5.4×10^{-3}
"1" → "2"	-1.9×10^{-3}	-7.7×10^{-3}
"1" → "3"	-4.4×10^{-3}	-10.0×10^{-3}
All shells	-5.6×10^{-3}	-10.7×10^{-3}

Table 3.12: The cumulative contribution to $\Delta\epsilon_{xx}$ of three shells of dipole transitions are shown in the table for NaCl. The shell indices in the first column correspond to those described in Figure 3.14. The table follows the same notation as Table. 3.6's last two columns.

there exists multiple inequivalent dipole transitions within each shell with differing dipole elements, and therefore the values for the dipole matrix elements are omitted in Table 3.12. We can see from the table that even in an ionic insulator like NaCl with very compact Wannier functions, in order to converge $\Delta\epsilon$ to a satisfactory accuracy, one must still sum the first three shells' contribution which includes dipole transitions between second-nearest neighbor atoms. (However, if we seek only an order of magnitude estimate with correct sign, two shells are sufficient.)

3.8 MgO

MgO shares the same crystal structure as NaCl and has very similar chemical properties. It is a rocksalt structured, closed-shell band insulator with its valence electrons filling the orbitals with mostly O character. In fact, after projecting the bands onto atomic-like orbitals, we find that the Wannier basis similar to the one for NaCl is also an appropriate choice for MgO: for occupied Wannier functions, we use one orbital with O s character and three orbitals with O p character to describe the valence bands; for unoccupied Wannier functions, we use one s-like and three p-like orbitals centered on Mg and five d-like orbitals centered on O to describe the low energy conduction bands. The DFT band structure and its Wannier interpolation are shown in Figure 3.15. One can see that the valence bands and lowest three conduction bands are accurately reproduced by the Wannier basis. The discrepancies between higher conduction bands and Wannier bands are attributed to the fact that there is more plane wave character in higher conduction bands, making for difficulties for any localized basis set.

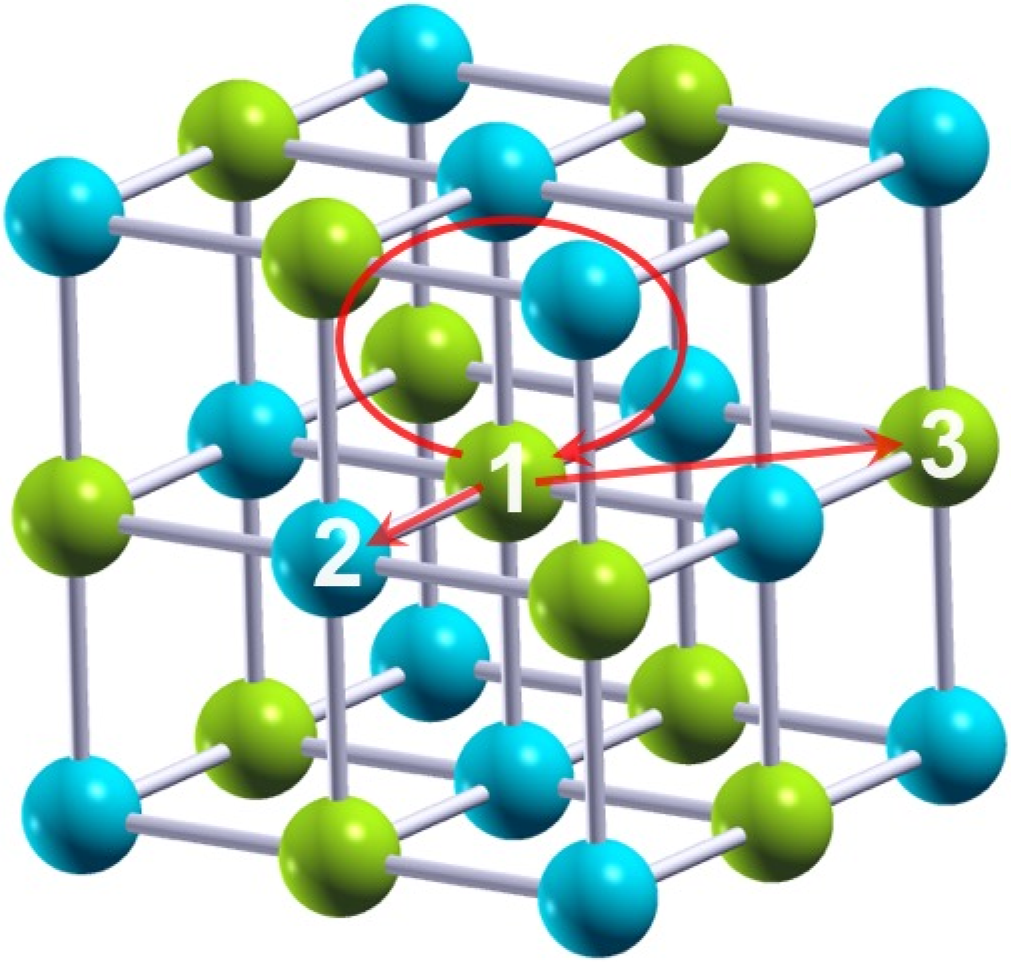

Figure 3.14: The three shells of dipole transitions in bulk NaCl with the largest matrix elements in the Wannier basis visualized in real space. Color scheme of the atoms: Na: cyan, Cl: green. Similar to Figure. 3.6, arrows are drawn from the centers of the occupied Wannier function (initial state on Cl) to the centers of the unoccupied Wannier functions (final state on either Cl or Na) of the dipole transition. Each individual atomic site corresponds to multiple occupied and unoccupied Wannier functions in NaCl (unlike in bulk Si and diamond where each chemical bond accommodates a unique pair of bonding and antibonding Wannier functions). With an initial occupied Wannier function on Cl atom "1", the arrow "1" → "1" illustrates the dipole transitions to the same atom (from the *sp* states to the *d* states of the same Cl atom), "1" → "2" illustrates the dipole transitions to the nearest-neighbor Na atoms (from the *sp* states of Cl to the *sp* states of the neighboring Na atoms), and "1" → "3" illustrates the dipole transitions to the second nearest-neighbor Cl atoms (from the *sp* states of Cl to the *d* states of its second nearest-neighbor Cl atoms).

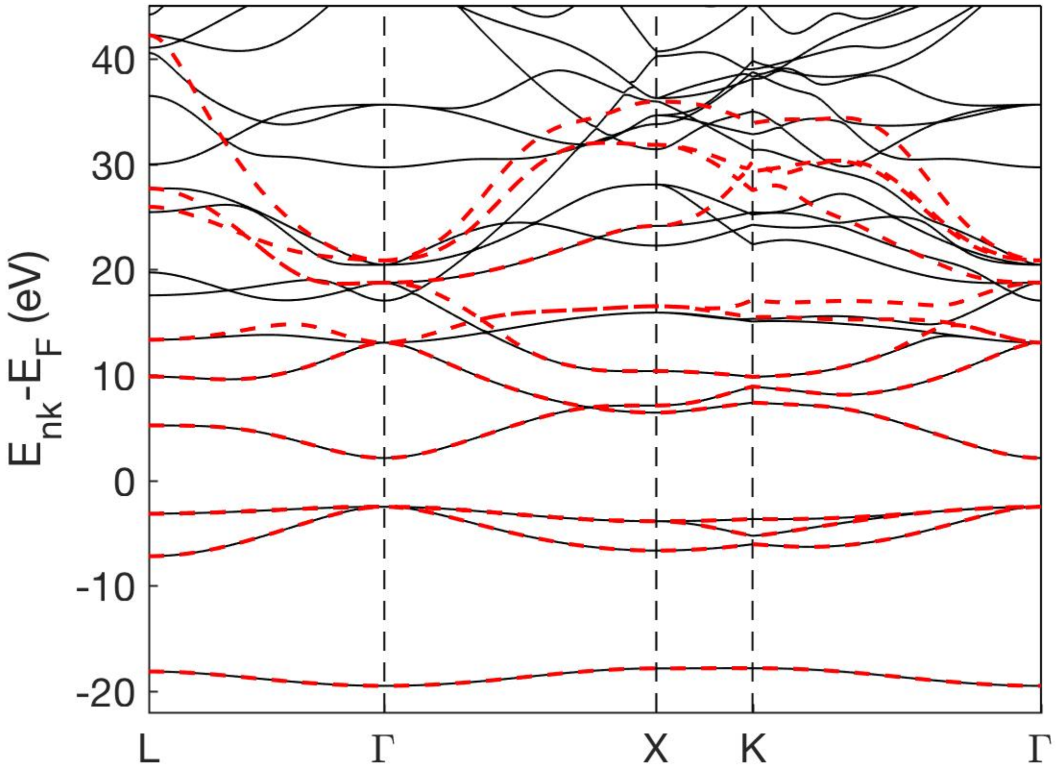

Figure 3.15: Band structure of bulk rocksalt MgO. Black solid lines are the DFT-LDA bands; red dashed lines are the Wannier interpolated bands. The valence Wannier bands are spanned by *sp*-like Wannier functions centered on O. The conduction Wannier bands are spanned by *sp*-like Wannier functions centered on Mg and *d*-like Wannier functions centered on O.

	DFPT	RPA (100 bands)	RPA (13 bands)	Wannier
$\epsilon(0.0\%)$	3.13	3.25	3.18	3.21
$\Delta\epsilon_{xx}(1.0\%)$	3.0×10^{-2}	3.0×10^{-2}	2.9×10^{-2}	3.1×10^{-2}
$\Delta\epsilon_{yy}(1.0\%)$	0.4×10^{-2}	0.4×10^{-2}	0.4×10^{-2}	0.5×10^{-2}

Table 3.13: Bulk rocksalt MgO dielectric constant and its change with 1% uniaxial strain along x-axis obtained using DFPT, RPA with Bloch states in a plane wave basis and with the Wannier basis. These methods are the same as those in Table. 3.4 and Table. 3.7. The results in the table are based on a $12 \times 12 \times 12$ k grid.

Table 3.13 shows how the dielectric constant changes with uniaxial strain in MgO computed using various methods. As expected, the Wannier method agrees well with RPA method with either converged number of bands or 13 bands which is equal to the total number of orbitals in the Wannier basis, just like discussed above in Si, diamond, and NaCl. However, MgO has the opposite elasto-optic response to NaCl in both p_{11} and p_{12} components: the dielectric constant of MgO increases both along and perpendicular to the tensile strain direction. In addition, the $\Delta\epsilon$ has much larger magnitude along the strain ($\Delta\epsilon_{xx}$ in Table 3.13) than perpendicular to the strain ($\Delta\epsilon_{yy}$ in Table 3.13). This difference between NaCl and MgO must originate from the chemistry of the different constituting atoms of the two materials and is a subject for future work.

The "standard" convergence calculation using different k grid has been performed for Si, diamond, and NaCl, and similar physical conclusions about the locality have be drawn from the relationship between the "standard" and "constrained sum" methods for all three materials. Hence, the calculations for MgO are done only based a dense $12 \times 12 \times 12$ k grid. Figure 3.16 shows that the dipole transition matrix element $|M|$ is very short-ranged, suggesting that the Wannier basis is also very localized in MgO.

Table 3.14 and Figure 3.17 report the spatial locality of ϵ and $\Delta\epsilon_{xx}$ with 1% strain along x-axis using the "constrained sum" method. As observed above, a spatial convergence of ϵ is obtained by progressively summing the contributions of dipole transitions with increasing distance. However, it is critical to emphasize that despite the sensible locality of dielectric and elasto-optic response, one must still include the dipole transitions in the $4 \times 4 \times 4$ supercell to achieve good convergence in both ϵ and $\Delta\epsilon_{xx}$.

The "shell" analysis results are shown in Table 3.15. Since MgO and NaCl both have

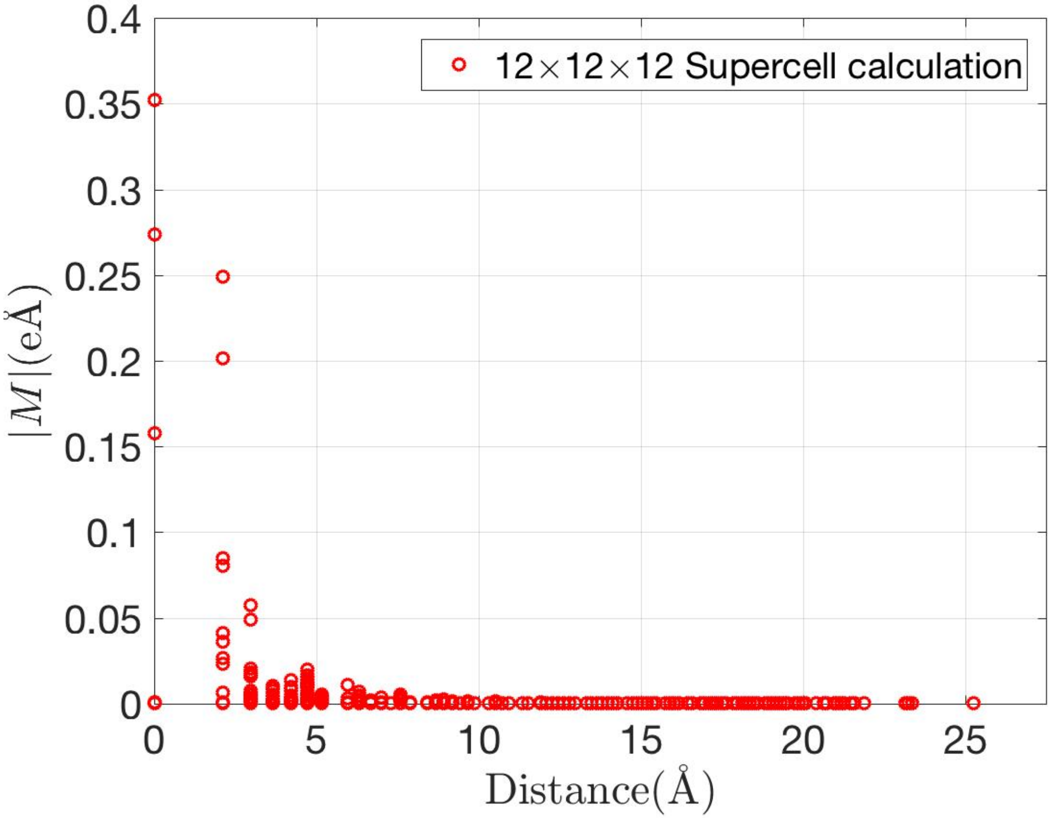

Figure 3.16: Magnitude of the bulk MgO Wannier dipole matrix elements $|M|$ versus distance between Wannier functions. The notations are the same as Figure. 3.4. For reference, the distance between the nearest Mg and O atoms is 2.11 Å.

		Size of supercell used to generate Wannier functions $12 \times 12 \times 12$
Subset of Wannier functions used	$2 \times 2 \times 2$	$2.10(1.4 \times 10^{-2})$
	$4 \times 4 \times 4$	$3.09(2.8 \times 10^{-2})$
	$6 \times 6 \times 6$	$3.19(3.0 \times 10^{-2})$
	$8 \times 8 \times 8$	$3.20(3.1 \times 10^{-2})$
	$10 \times 10 \times 10$	$3.21(3.1 \times 10^{-2})$
	$12 \times 12 \times 12$	$3.21(3.1 \times 10^{-2})$

Table 3.14: Convergence with supercell size of the dielectric constant and its strain dependence in bulk MgO using the Wannier function method. The "standard" convergence calculation is not performed for MgO. The results in the table are all based on the $12 \times 12 \times 12$ k grid calculation. This table uses the same nomenclature as Table. 3.5.

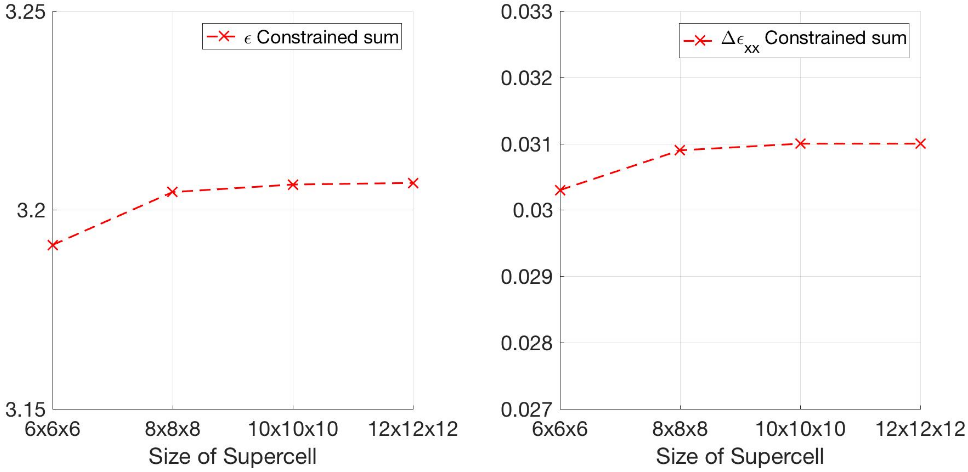

Figure 3.17: Convergence of ϵ_{xx} and $\Delta\epsilon_{xx}$ with 1.0% uniaxial strain along x-axis in bulk MgO using the Wannier function method. The figure uses the same notations as Figure 3.5.

Dipole transition matrix elements	Cumulative contribution to $\Delta\epsilon_{xx}$ 1% x-strain	1% y-strain
"1" → "1"	$+0.7 \times 10^{-2}$	-0.4×10^{-2}
"1" → "2"	$+2.1 \times 10^{-2}$	$+0.4 \times 10^{-2}$
"1" → "3"	$+2.5 \times 10^{-2}$	$+0.1 \times 10^{-2}$
All shells	$+3.1 \times 10^{-2}$	$+0.5 \times 10^{-2}$

Table 3.15: The cumulative contribution to $\Delta\epsilon_{xx}$ of three shells of dipole transitions are shown in the table for MgO. The shell indices in the first column are defined the same as those in Figure 3.14 and Table 3.12. The table follows the same notation as Table 3.12.

the rocksalt crystal structure, we can label their "shells" in exactly the same way. Although in MgO, $\Delta\epsilon$ converges according to the shells at a similar rate to NaCl, the MgO dielectric responds to the strain in the opposite direction to NaCl as noted above in Table 3.13. In addition, the $\Delta\epsilon$ perpendicular to strain even converges non-monotonically with shells, which makes the photoelasticity longe-ranged in MgO.

3.9 Summary and Outlook

In this paper, we have developed a method to calculate the dielectric and elasto-optic response of solids within the RPA using a Maximally Localized Wannier Function basis. Compared with state-of-the-art DFPT method, RPA in the Wannier basis achieves a satisfactory numerical accuracy while presenting a simple analytical expression that highlights the role of dipole transitions between the occupied and unoccupied Wannier functions. By organizing the dipole transitions into shells according to the distances between the occupied and unoccupied Wannier functions, both of the dielectric and photoelastic responses systematically converge within the "constrained sum" method and their spatial behavior is sensible. We have discovered that elasto-optic responses are rather delocalized in the Maximally Localized Wannier basis: in Si, diamond, NaCl, and MgO, we must sum the cumulative contributions of at least 3 spatially localized shells to converge $\Delta\epsilon$ to a reasonable precision. Moreover, the convergence with increasing shells is not monotonic in some cases (e.g., p_{12} in Si and MgO). Silicon's long-tailed Wannier functions, which need to be generated in a relatively large supercell, lead to the long-ranged behavior of its photoelasticity. However, in spite of the Wannier functions being quite compact in diamond, NaCl, and MgO, their locality of the elasto-optic response is still at a similar scale to bulk Si: one must sum up to 3 shells' contribution to converge the change of dielectric constant with reasonable precision. The length scale of locality in the Maximally Localized Wannier basis is too large and contains too many dipole transitions for us to extract simple material design rules for photoelasticity. This is in contrast to the locality of the electronic polarizability in the MLWF basis [64] where a nearest-neighbor only model is already quantitatively accurate. However, not all is lost: while not localized as one would like on individual atoms and chemical bonds, the real-space Wannier description is far more localized than the k-space description for describing the dielectric and photoelastic response, and a reasonably-sized nanocluster of the material (i.e., up to the third shell of nearest-neighbors) is sufficient to describe the photoelastic response. In addition, we have discovered some unexpected photoelastic behaviors, e.g., Tables 3.12 and 3.15 show that NaCl and MgO have opposite photoelastic responses, or that there is a non-monotonic convergence with increasing number of space shells for the p_{12} component in Si, diamond, and MgO. Despite significant effort, at present we are unable to explain these unexpected behaviors and hope the future work will elucidate the situation.

There is an existing literature that uses highly-localized bond orbital tight-binding models to compute dielectric response in solids [49, 65] that can be extended to photoelastic response. For example, the empirical model for the strain dependencies of dielectric response by Damas *et al.* [48] assumes a nearest-neighbor tight-binding model in tetrahedral semiconductors based on bond orbital theory for Si. They build a (2×2) Hamiltonian with fitting parameters with two sp^3 hybrid orbitals on neighboring atoms as the basis to describe the bond polarizability, and the free parameters are fit to photoelasticity experiments. Since this model only includes the first shell of contribution for dielectric response, which according to our work is microscopically inadequate, the effects of higher order shells must be strongly renormalizing the values of the empirical parameters. Such a compact description can help us understand *a posteriori* the photoelasticity of known materials where experimental values are available, but it is of limited value for materials design or prediction.

In this work, we have revealed the relatively long-ranged nature for photoelasticity when described in real space using Wannier functions. The questions of whether the elasto-optic effect is intrinsically a relatively long-ranged phenomenon for all materials and whether an alternative *ab initio* real-space basis will compactify its description remain open for future investigations.

3.10 Appendix

Sec. 3.3 describes our method for computing the longitudinal RPA dielectric constant in both Bloch and Wannier bases, which is adequate for calculating the p_{11} and p_{12} component of photoelasticity. However, the calculation of the last non-zero component of photoelastic tensor in a cubic crystal, p_{44}, requires extending our method to compute off-diagonal components of the dielectric tensor such as ϵ_{yz}. We summarize our approach here.

We compute the full dielectric tensor using the following expression:

$$\epsilon_{ij} = \delta_{ij} + \frac{16\pi}{V} \cdot \frac{1}{|q|^2} \sum_{\mathbf{k}} \sum_{c,v} \frac{\left\langle \psi_{c,\mathbf{k}} \left| e^{-i\mathbf{q}_i \cdot \mathbf{r}} \right| \psi_{v,\mathbf{k}+\mathbf{q}_i} \right\rangle^* \cdot \left\langle \psi_{c,\mathbf{k}} \left| e^{-i\mathbf{q}_j \cdot \mathbf{r}} \right| \psi_{v,\mathbf{k}+\mathbf{q}_j} \right\rangle}{E_{c,\mathbf{k}} - E_{v,\mathbf{k}+\mathbf{q}_j}} \tag{3.10}$$

where the small wave vectors $\mathbf{q}_i$ and $\mathbf{q}_j$ are aligned with the i and j axes (i.e., two perpendicular Cartesian axes); other aspects of the notation follow the nomenclature of Eq. (3.2). In our calculations, the length of the $\mathbf{q}$ vectors are equal to 1% of that of a primitive reciprocal lattice vector.

Substituting the relation between MLWFs and Bloch states leads to the following expression for the dielectric tensor in the Wannier basis:

$$\epsilon_{ij} = \delta_{ij} + \frac{16\pi}{V} \cdot \frac{1}{|q|^2} \cdot M^{i\,\dagger} \cdot F \cdot M^j \tag{3.11}$$

We have used a compactified representation of the summation notation similar to Eq. ((3.7)) where $M^i_{a,b,\mathbf{R}} = \left\langle W_{a,\mathbf{R}} \left| e^{-i\mathbf{q}_i \cdot \mathbf{r}} \right| W_{b,\mathbf{0}} \right\rangle$ and $M^j_{a,b,\mathbf{R}} = \left\langle W_{a,\mathbf{R}} \left| e^{-i\mathbf{q}_j \cdot \mathbf{r}} \right| W_{b,\mathbf{0}} \right\rangle$ are the dipole matrix elements along the i and j axes, respectively.

One technical issue with the above equations concerns the fact that two separate sets of k point grids are used to compute the dipole matrix elements: the conduction bands are evaluated on the usual Γ-centered k grid while the valence bands are evaluated on two separate k grid shifted by the small vectors $\mathbf{q}_i$ and $\mathbf{q}_j$ from Γ. A correct calculation of dielectric tensor requires that the Bloch states on two sets of k grids obey the "natural" gauge: $\langle \psi_{m,\mathbf{k}} | \psi_{n,\mathbf{k}+\mathbf{q}} \rangle \longrightarrow \delta_{mn}$ when $\mathbf{q} \longrightarrow 0$, which is not guaranteed by numerical diagonalization procedures used in standard electronic structure calculations (e.g., when using Quantum Espresso). Generally, the computed Bloch states on two k point grids are related to each other through a unitary transformation:

$$\langle \psi_{m,\mathbf{k}} | \psi_{n,\mathbf{k}+\mathbf{q}} \rangle = Q^{(\mathbf{k})}_{mn}$$

where $Q^{(\mathbf{k})} \cdot Q^{(\mathbf{k})\dagger} = Q^{(\mathbf{k})\dagger} \cdot Q^{(\mathbf{k})} = I$ when q $\longrightarrow 0$. The "natural" gauge can be restored easily by performing a unitary transformation (only needed for the shifted valence bands:

$$\tilde{\psi}_{v,\mathbf{k}+\mathbf{q}} = \sum_{v'} \psi_{v',\mathbf{k}+\mathbf{q}} \cdot Q^{(\mathbf{k})\dagger}_{v'v}$$

where v, v' range over valence band indices. We use such unitary rotated valence bands $\tilde{\psi}$ when computing off-diagonal dielectric tensor components such as ϵ_{yz} (for diagonal components, there is only a single shifted k grid so the issue of the natural gauge does not arise).

Chapter 4

First principles description of 2D SiO_2 on metal substrates

4.1 Introduction

In the past decade, two-dimensional (2D) atomically thin sheets that interact with their surroundings through Van der Waals interactions have attracted significant interest [29, 66–68] due to the new physical properties observed in such reduced-dimensional systems and their relative chemical stability. The recent creation of 2D SiO_2 [1, 69–75] adds a new member to this material class. 2D SiO_2 is a bilayer constructed from two mirror image planes of corner-sharing SiO_4 tetrahedra with no dangling bonds. First principles calculations show that these bilayers interact weakly through dispersive Van der Waals forces with metallic substrates [74, 76]. The 2D bilayer SiO_2, in its ground state, has a crytalline structure with hexagonal six-membered Si ring motifs (see Figure 4.1a,b) [74, 77]. However, due to the flexibility of the intra-sheet SiO_4 tetrahedral linkages, 2D SiO_2 can adopt a variety of other sturctures: defects, domain boundaries, and amorphous phases in 2D SiO_2 lead to a broad distribution of Si ring sizes ranging from four to nine [69]. 2D SiO_2 does not have a layered structural counterpart in bulk form, and thus it cannot be found by thinning a known bulk phase silica. In addition to being a 2D material, 2D SiO_2 is of interest because of its structural similarity to zeolite catalysts: bulk 3D SiO_2 in zeolite form has broad applications in catalysis due to a porous structure that hosts a large internal surface area where chemical reactions can take place [78–80]. However, it is experimentally difficult to probe the microporous internal surfaces of zeolites, leading to difficulties in identifying key catalytic mechanisms [81]. 2D bilayer SiO_2 can serve as a model system that imitates the interior surface of bulk zeolites while its 2D nature permits application of surface microscopy techniques that reach atomic scale resolution [82,83]. It is known that variable Si ring sizes are present in representative zeolites structures [84] whose chemical reactivity is modified by substituting Si by Al dopants in different-sized rings: 2D SiO_2's variable Si ring sizes open a gate for studying catalytic sites in zeolite structures. Finally, the flexibility of the Si ring sizes in 2D SiO_2 can be exploited to create molecular sieves that operate based on the size of the rings [85]. Due to these fundamental and practical interests, it is preferable to be able to introduce different sized Si rings in 2D SiO_2 in a predictable manner.

2D SiO_2 is prepared in experiments typically by deposition on a metal surface from a silicon source with subsequent high temperature annealing in a background of oxygen gas. There have been a number of studies concerning the morphologies of 2D SiO_2 on various transition metal substrates. On the Mo(112) surface, 2D silica organizes itself into a crystalline $SiO_{2.5}$ monolayer that is chemically coupled to the substrate through Si-O-substrate bonds [86, 87]. On Ru(0001), 2D silica can form a crystalline monolayer, an epitaxial crystalline bilayer, or an amorphous bilayer depending on the growth conditions [73–75]. Only crystalline incommensurate 2D bilayer SiO_2 is observed when grown on Pd(111) [1] while only amorphous 2D bilayer SiO_2 is observed on Pt(111) [70]. Prior first principles calculations by Malashevich *et al.* [77] demonstrated the possibility of controlling the 2D SiO_2 morphology by straining the SiO_2 thin film. Malashevich *et al.* also proposed a number of structural models for 2D SiO_2 with various sized Si ring motifs that can be used to model defects [88], domain boundaries [89,90], and amorphous regions [91,92] in 2D SiO_2. The recent creation of Ni-Pd random alloy surfaces [93] provides a substrate system with a continuously tunable lattice constant (through changing the chemical composition), enabling the study of how the substrate lattice mismatch and binding can determine the 2D SiO_2 overlayer morphology.

Motivated by these prior studies, this work describes first principles calculations of

2D bilayer SiO_2 on various metal substrates and investigates the effects of the overlayer-substrate lattice mismatch and binding on the commensurate-incommensurate competition in the 2D SiO_2 overlayer. The structure of the paper is as follows. Sec. 4.2 describes our computational methods and a discussion about Van der Waals corrections to density functional theory (DFT). The impact of having the underlying metal support is investigated using DFT together with three Van der Waals functionals in Sec. 4.3.1. In Sec. 4.3.2, the favorability of the epitaxial 8-6-4 bilayer silica structure and hexagonal bilayer structure on Ru(0001) are compared, generalizing prior work on strain-induced non-hexagonal Si ring motifs in isolated 2D SiO_2 layers. Sec. 4.3.3 describes a practical method to approximately compare the energies of commensurate and incommensurate 2D SiO_2 overlayers without performing large-scale first principles calculations, and the method is then applied to predict the stable morphologies of 2D SiO_2 on the three metal substrates Ru(0001), Pd(111), and $Ni_{0.5}Pd_{0.5}$(111). Sec. 4.3.4 describes the impact of chemisorbed oxygen on the metal surfaces on 2D SiO_2's structures. Key findings are summarized in Sec. 4.4.

4.2 Methods

We use density functional theory (DFT) with the PBE [13] generalized gradient approximation (GGA) exchange-correlation functional to study 2D bilayer silica on various metallic substrates, i.e., Ru(0001), Pd(111), and the Ni-Pd alloy $Ni_{0.5}Pd_{0.5}$(111) which all have a hexagonal surface lattice. The calculations are performed using the Quantum Espresso [17] software package using a plane wave basis and periodic boundary conditions. Norm-conserving pseudopotentials are used to describe the ionic cores [14–16]. An energy cutoff of 70 Ry is used for the plane wave basis. Due to the metallic nature of the substrates, Gaussian smearing with a broadening of 0.01 Ry is used to describe the occupations of Kohn-Sham states. Two kinds of surface periodicities are considered: a (2×2) surface unit for the hexagonal bilayer SiO_2 and a $(3 \times 2\sqrt{3})$ surface unit cell for the "8-6-4" bilayer SiO_2 (detailed in Sec. 4.3). Both unit cells employ a $6 \times 6 \times 6$ k-point grid to sample the first Brillouin zone. Spin polarization is included for the simulations containing the $Ni_{0.5}Pd_{0.5}$ alloy substrate. Our choice of the computational parameters is sufficient to converge the total energies to within 2 meV/atom.

The simulations of atomic structures consist of two steps. First, we fully relax the substrate in bulk form to obtain its optimal lattice parameters. Then, we place 2D bilayer SiO_2 on a substrate slab with fixed bulk lattice vectors for further relaxation. The substrate slab is modeled using five layers of metal atoms, and the atomic coordinates of bottom two layers are fixed to their bulk positions to simulate mechanical boundary conditions corresponding to a thick and bulk-like substrate. The periodic images of each silica+substrate slab are separated by at least 15 Å of vacuum in the simulation cell. The structural relaxation is performed until all axial force components on each atom are smaller than 10^{-4} Ry/Bohr in magnitude and all components of the stress tensor are less than 0.1 kbar in magnitude.

Due to the fully saturated nature of every chemical bond in 2D bilayer SiO_2, the bilayer interacts weakly and primarily through van de Waals (vdW) interactions with any substrate. Recent work has shown that this vdW interaction draws the SiO_2 closer to a Ru substrate and can induce some charge redistribution near the interface [76]. Semilocal functionals such as PBE-GGA do not account for long-ranged vdW interations. Hence, vdW corrections must be added "on top" of standard DFT calculations to model these systems more accurately. The design and use of vdW corrections for DFT total energy functionals is a broad and active field of research with many available methods [28]. In this work, we use three of the simplest functionals (DFT-D2, DFT-vdW, DFT-vdW$^{\mathrm{surf}}$) [31–33] due to their computational efficiency. The DFT-D2 is an empirical functional depending only on interatomic distances and atomic polarizabilities, while for the DFT-vdW and DFT-vdW$^{\mathrm{surf}}$ functionals the vdW interactions use atomic polarizabilities that are scaled using the electron density in a self-consistent manner.

Our work describes 2D SiO_2 layers placed on random Ni-Pd metal alloy substrates with *fcc* lattices [93]. A standard approach to dealing with random alloys in DFT calculations is to use the virtual crystal approximation (VCA) where the alloy atoms are replaced by a virtual atom whose pseudopotential is the composition-weighted average of those of the different species forming an alloy [94]. The 2D bilayer SiO_2 on $Ni_{0.5}Pd_{0.5}$ served as a benchmark system in our previous study [2] of Ni silicate forming on the Ni-Pd alloy substrate: experimental data indicated that the Ni atoms from the alloy diffuse from the bulk and segregate at the interface between the substrate and the overlayer after the growth of the 2D $\mathrm{SiO_2}$. Hence, we model the alloy substrate in this work in the same manner to accommodate the experimental facts: the alloy substrate slab consists of one surface layer of Ni atoms above four layers of $\mathrm{Ni_{0.5}Pd_{0.5}}$ virtual atoms. The appropriateness of using the VCA in this manner is explained in Ref. [2].

We also need to modify the vdW functionals to allow for their use with the VCA approach. The modifications can be performed in a way that gives the correct asymptotic behavior at large interatomic separation. In the DFT-D2 functional, the sum of pairwise interatomic $-C_6/R^6$ dispersion terms is added to the DFT total energy with the added energy term taking the form [31]

$$E_{\text{disp}} = -s_6 \sum_{\langle i,j \rangle} f_{\text{dmp}}(R_{ij}) \cdot \frac{C_6^{ij}}{R_{ij}^6}$$

where the summation over $\langle i, j \rangle$ runs over each pair of atoms in the system. Here, s_6 is scaling factor that is optimized for different exchange-correlation functionals, C_6^{ij} is the dispersion coefficient, and R_{ij} is the distance between atoms i and j. A damping function $f_{\text{dmp}}(R_{ij}) = [1 + \exp(-d(R_{ij}/R_r - 1))]^{-1}$ is used to avoid the sigularities in the dispersion terms when the interatomic distances become small. The number d is a dimensionless parameter that controls the decay rate of the damping function to zero. The optimized value for PBE-GGA is $d = 20$ [31]. $R_r = R_i^0 + R_j^0$ is the sum of atomic vdW radii of atoms i and j which are determined using isolated-atom computations of their species. The interatomic dispersion coefficient C_6^{ij} is taken to be the geometric mean of the atomic dispersion coefficient $C_6^{ij} = \sqrt{C_6^i \cdot C_6^j}$ where the C_6^i are computed from first principles for an isolated atom of the same species: the main physical ingredients that determine the atomic C_6 are the atomic ionization potential and atomic dipole polarizability. Here, we only modify the DFT-D2 functional to make it fit into the VCA framework for the random alloy $\mathrm{Ni_{0.5}Pd_{0.5}}$. The C_6 coefficient for the virtual alloy atom is

$$C_6^{\mathrm{Ni_{0.5}Pd_{0.5}}} = \left(\frac{\sqrt{C_6^{\mathrm{Ni}}} + \sqrt{C_6^{\mathrm{Pd}}}}{2} \right)^2$$

in order to ensure that at large interatomic distances (where $f_{\mathrm{dmp}} \approx 1$) the dispersion force caused by an alloy atom is equal to the statistical average of those caused by Ni and Pd. Lastly, we set the value of the vdW radius of the virtual alloy atom to be the arithmetic mean of the vdW radii of Ni and Pd.

4.3 Results and Discussions

4.3.1 Hexagonal bilayer silica on various metal substrates

First, we present results for 2D bilayer SiO_2 with a hexagonal six-membered-ring structure on various metal surfaces simulated using the three vdW functionals (DFT-D2, DFT-vdW, DFT-vdW$^{\mathrm{surf}}$) described in Sec. 4.2. The structures are visualized in Figure 4.1. 2D SiO_2 can have a variety of registries on the surface, i.e., the overlayer can have different alignments in x-y plane with respect to the substrate. Figure 4.1 depicts the bilayer SiO_2 overlayer having two representative registries: in registry 1, every O atom is above a surface metal atom, while in registry 2, every O atom is above a hollow site of the substrate surface layer.

The geometrical information and binding energies of the relaxed 2D SiO_2 system shown in Table 4.1 help elucidate the vdW nature of the interaction across the overlayer-substrate interface. The binding energy per Si atom of the 2D SiO_2 overlayer is computed according to the following equation for a (2×2) surface unit cell

$$\Delta E_{\mathrm{binding}} = \frac{1}{4} \cdot \left(E^{\mathrm{Si_4O_8/Metal}} - E^{\mathrm{Si_4O_8}} - E^{\mathrm{Metal}}\right) \tag{4.1}$$

where $E^{\mathrm{Si_4O_8/Metal}}$ is the total energy of the system of 2D SiO_2 on the metal slab, $E^{\mathrm{Si_4O_8}}$ is the total energy of the free-standing 2D bilayer SiO_2 strained to the corresponding substrate lattice, and E^{Metal} is the total energy of the relaxed metal substrate slab. Table 4.1 shows that the distances between the bottom layer oxygen atoms in SiO_2 and the substrates, d(M-O), are well above the typical bond length of 1.8–2.0 Å for a chemisorbed oxygen on the corresponding substrate: this highlights the absence of chemical bonds between the two subsystems. When the 2D SiO_2 on Ru(0001) is simulated using DFT without any vdW correction, the resulting distance d(M-O) becomes even larger, suggesting that the

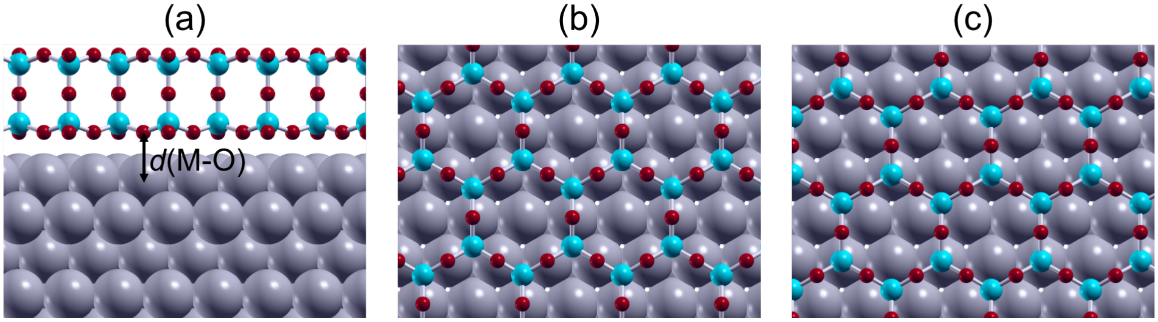

Figure 4.1: Side and top views of the hexagonal bilayer SiO_2 on metal substrates. Color scheme: Si cyan, O red, M grey (M is the metal atom in the substrate). (a) side view of the bilayer SiO_2 on a metal substrate; (b) top view of the bilayer SiO_2 in registry 1 with the surface: every O atom is above a metal atom; (c) top view of the bilayer SiO_2 in registry 2 with the surface: every O atom is above a hollow site.

interaction between 2D SiO_2 and metal substrate is truly long-ranged. In fact, if we were to consider only the DFT part of the total energies (by removing the contribution from the vdW correction term) for the DFT-D2 relaxed registry 1 structure of 2D SiO_2 on Ru, the SiO_2 would have a positive binding energy of 35 meV per Si. This means that it is the vdW correction that draws the 2D SiO_2 close to the surface, and that the DFT-only contribution of the total energy is in the repulsive regime.

Although the specific values of d(M-O) and the binding energies depend on the vdW functional used (see Table 4.1), the same trend is observed for all three vdW corrections: registry 2 has a weaker binding and a larger d(M-O) than registry 1 for all the substrates. In fact, we find that registry 1 has the strongest binding and registry 2 has the weakest binding among all possible SiO_2 overlayer alignments that we have studied on these metals. (The variation of the binding energies with registry will become important in Sec. 4.3.3 regarding the competition between commensurate and incommensurate 2D SiO_2 overlayers.)

4.3.2 Epitaxially strained 2D bilayer SiO_2 in different morphologies on Ru

Our prior work demostrated the possibility of controlling the morphology of 2D SiO_2 using epitaxial strain imparted by a substrate [77]. In fact, 2D bilayer silica can take forms other than hexagonal six-membered Si rings. Ref. [77] proposed several structural models for

			Ru(0001)	Pd(111)	$Ni_{0.5}Pd_{0.5}(111)$
Strain			3.5%	5.8%	0.5%
Registry 1	d(M-O)	DFT	3.99 Å	-	-
		DFT-D2	2.61 Å	2.77 Å	2.60 Å
		DFT-vdW	2.60 Å	2.93 Å	-
		DFT-vdW$^{\mathrm{surf}}$	2.61 Å	2.89 Å	-
	Binding energy/Si	DFT	-5 meV	-	-
		DFT-D2	-226 meV	-218 meV	-172 meV
		DFT-vdW	-224 meV	-139 meV	-
		DFT-vdW$^{\mathrm{surf}}$	-109 meV	-122 meV	-
Registry 2	d(M-O)	DFT-D2	3.09 Å	2.80 Å	3.05 Å
		DFT-vdW	3.26 Å	3.09 Å	-
		DFT-vdW$^{\mathrm{surf}}$	3.67 Å	2.95 Å	-
	Binding energy/Si	DFT-D2	-137 meV	-197 meV	-121 meV
		DFT-vdW	-158 meV	-118 meV	-
		DFT-vdW$^{\mathrm{surf}}$	-45 meV	-101 meV	-

Table 4.1: Binding energies of hexagonal bilayer SiO_2 on various metal substrate computed using the DFT-D2, DFT-vdW, and DFT-vdW$^{\mathrm{surf}}$ functionals. The atomic structures for registry 1 and 2 are depicted in Figure 4.1b, c, respectively. The strain is defined by the amount of lattice expansion required to epitaxially strain one unit cell SiO_2 to a (2×2) cell of the hexagonal surface. The SiO_2 overlayer-surface distance d(M-O) is measured by the distance between the bottom-most layer of oxygen atoms in 2D SiO_2 and the metal surface atoms along z direction as per Figure 4.1a. For comparison, the typical bond length between a chemisorbed oxygen atom to its bonded surface metal atom is 2.06 Å, 1.99 Å, and 1.81 Å for Ru(0001), Pd(111), and $Ni_{0.5}Pd_{0.5}(111)$, respectively. It is clear that d(M-O) is too large for the formation of chemical bonds between substrate metal atoms and 2D SiO_2 overlayer oxygen atoms. The role of surface chemisorbed oxygen atoms will be disscussed below in Sec.4.3.4.

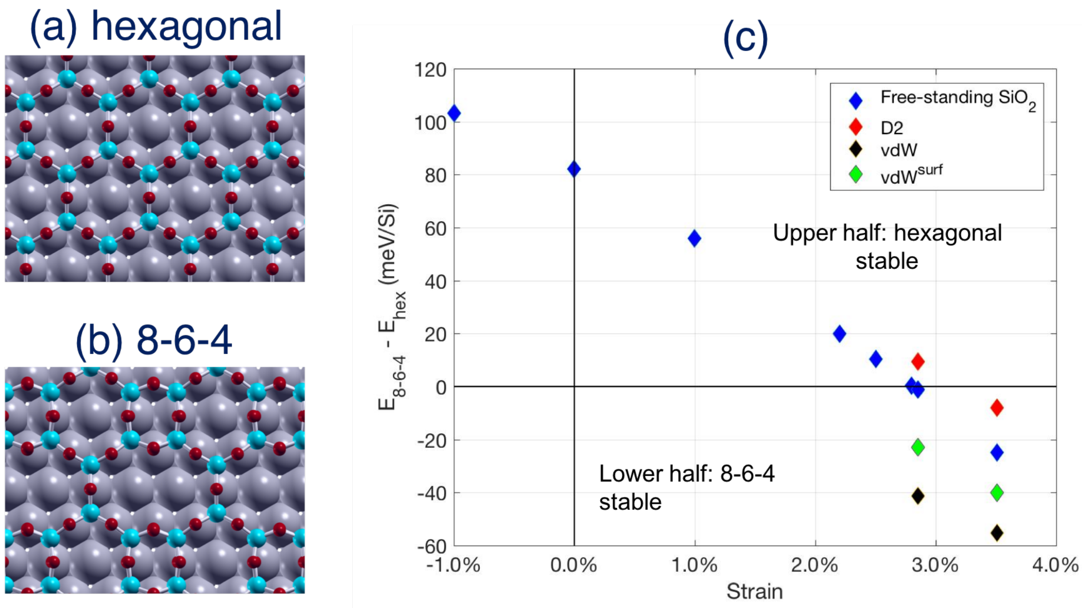

Figure 4.2: Energy difference between 2D SiO_2 in 8-6-4 structure and hexagonal structure. (a) top view of 2D hexagonal SiO_2 on Ru(0001); (b) top view of 2D 8-6-4 SiO_2 on Ru(0001); (c) energy difference between SiO_2 in 8-6-4 and hexagonal structures computed from first principles on Ru(0001) with three different vdW corrections.

2D SiO_2 that are constructed by stitching together different sized Si ring motifs. At zero strain, these structural models are all higher in energy (e.g., by a few tens meV per Si) than unstrained hexagonal 2D SiO_2. However, when the 2D SiO_2 is epitaxially strained to Ru(0001), 2D $SiO_2$with non-hexagonal ring motifs can become more energetically stable than the hexagonal one. This suggests that one can achieve larger or smaller sized Si ring structures by the choice of substrate. Motifs formed by five and eight-membered rings are observed as domain boundaries of 2D crystalline silica on Ru(0001) [90]. When prinstine 2D SiO_2 is doped with Al to form aluminium silicate, motifs combined from four, six and eight-memebered rings become increased in number and are observed as the domain boundary structure on Ru(0001) [95]. The label "8-6-4" for such structures describes the combination of these ring sizes in one unit cell (Figure 4.2b). Bilayer SiO_2 with the "8-6-4" structure is also relevant for modeling bulk zeolites because four, six, and eight-membered rings are present at the interior of chabazite, i.e., one of the key representative zeolite structures [84, 96].

In our prior work, the 2D bilayer SiO_2 was simulated as a free standing film where the effect of the substrate was incorporated through epitaxially straining the isolated SiO_2 layer to the substrate's lattice constant. Though this approach is sensible due to the fact that the 2D silica is chemically decoupled from the substrate, the binding to the surface due to dispersion forces plays a role in the relaxation of the atomic structures, i.e., it draws the 2D SiO_2 closer to the surface as noted in Sec. 4.3.1. Thus, explicit inclusion of the substrates in the simulations is desired for an improved physical description. Here, we compare the energy difference between 2D SiO_2 in the 8-6-4 and hexagonal structures on Ru(0001) using the three vdW correction functionals (see Figure 4.2a,b for the structures). Since the simulations are computationally demanding, only two strain states are selected: 3.5% and 2.9% tensile strain in Figure 4.2c correspond to the theoretical and experimental [74] lattice constant of Ru, respectively. As Figure 4.2 shows, the strain value at which the energy difference between hexagonal and 8-6-4 SiO_2 changes sign depends on the vdW functional used, but the trend is the same for 2D SiO_2 simulated with and without Ru substrate: a smaller tensile strain favors the hexagonal structure while a larger tensile strain favors the 8-6-4 structure. This suggests that 2D SiO_2 can form Si ring motifs other than hexagonal six-membered rings as a strain relieving mechanism, as suggested by experiments where point defects [88], domain boundaries [89,90], and amorphous structures [91,92] in 2D SiO_2 display a distribution of ring sizes ranging from four to nine. We conclude that epitaxial strain plays an important role in controlling the morphologies of 2D SiO_2 overlayers.

4.3.3 Approximate description of incommensurate binding

As observed in experimental studies, 2D bilayer SiO_2 does not always form a crystalline commensurate (epitaxial) structure on the metal substrate. When a 2 monolayer equivalent amount of Si is deposited on Ru(0001), which could lead to an epitaxial overlayer under 2.9% (experimental) tensile strain (with zero strain defined by the free-standing 2D hexagonal bilayer SiO_2 lattice constant computed using DFT), 2D SiO_2 can form either a commensurate crystalline haxagonal structure or an amorphous structure depending on the cooling rate after high temperature annealing [73]. In another experiment, coexisting patches of crystalline and amorphous 2D SiO_2 are observed on the surface of Ru [89]. When grown on Pd(111) which has a larger experimental tensile strain of 4.3% [1], 2D SiO_2 forms an

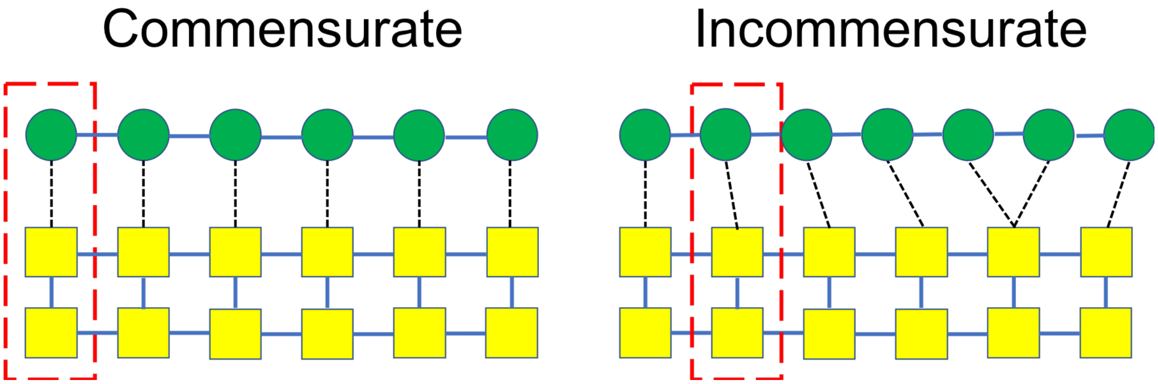

Figure 4.3: Schematic of commensurate (left) and incommensurate (right) lattices in one dimension. Yellow squares represent the substrate's atoms and green circles represent the overlayer's atoms. Rad dashed rectangles describe the substrate unit cell. Black dashed lines indicate binding bewteen overlayer and substrate with vertical lines corresponding to optimal binding.

incommensurate structure and a moiré pattern is observed in STM instead of an epitaxially strained 2D layer with enlarged hexagonal rings. When an even greater experimental tensile strain of 5.1% is applied by Pt(111) [70], only amorphous 2D SiO_2 has been observed. It is evident that the lattice mismatch and binding strength provided by different metal substrates play a role in controlling the final morphologies of the 2D SiO_2 [69]. The creation of the Ni-Pd random alloy system [93] provides a platform where the lattice constant can be tuned continuously by changing its chemical composition. It helps us answer the question of how much lattice distortion can be applied to 2D SiO_2 before it changes its morphology.

Here, we focus on the structural competition between the 2D hexagonal bilayer SiO_2 in commensurate and incommensurate relation to the substrate. In what follows, a commensurate lattice is achieved by one unit cell of the hexagonal 2D SiO_2 being epitaxially strained to a (2×2) unit cell of a metal surface with a hexagonal lattice. A commensurate structure enforces the overlayer to have the same periodicity as the subsrate thereby maximizing the binding energy (see Figure 4.3 (left)) at the cost of straining the overlayer. In the incommensurate structure, the overlayer adopts its own relaxed periodicity thereby minimizing strain energy at the cost of imperfect binding to the substrate due to the lack of registry since the overlayer and substrate lattice constants have no reason to be equal (see Figure 4.3 (right)).

The difficulty in directly comparing the energies of 2D SiO_2 in commensurate and incommensurate lattices arises from the fact that a very large superlattice is required to faithfully describe a low-strain incommensurate overlayer. For example, a (2×2) unit cell of Ru(0001) has a 3.5% theoretical tensile strain mismatch compared to the (1×1) unit cell of 2D SiO_2, so that a (31×31) unit cell superlattice of the 2D SiO_2 on a (60×60) surface unit cell of Ru(0001) is the minimum periodicity required to achieve 0.2% tensile strain for the overlayer: this superlattice has more than 29,000 atoms in the simulation cell and is computationally intractable from first principles.

One way to go around this difficulty would be to employ a simple analytical model, e.g., the Frenkel-Kontorova (FK) model [97, 98], to model the large supecell. In such a model, the total energy has two competing contributions with parameters fit to first principles calculations: first, the overlayer atoms interact with each other via harmonic springs, and this describes the effect of straining the overlayer; second, a simple sinusoidal model potential describes the binding of the overlayer atoms to the periodic substrate. This type of model can efficiently describe the extreme cases where one energy contribution dominates as well as intermediate situations where they are of similar magnitude.

Here, we will compute instead the two energy contributions approximately but directly from first principles. The strain contribution is computed easily by straining free-standing SiO_2 to different surface lattice constants. The binding energy for commensurate SiO_2 overlayers is computed by placing the 2D SiO_2 on the substrate using its optimal binding registry (registry 1 in Sec. 4.3.1). To approximate the binding energy for an incommensurate SiO_2 overlayer, we use the long wavelength limit appropriate for a long-period superlattice: we assume the overlayer samples all the different relative local registries between substrate and overlayer equally as we scan across the superlattice. We model this situation by performing a large number of calculations of commensurate (2×2) surface unit cells of 2D SiO_2 on the metal substrate for a variety of different registries between overlayer and substrate (i.e., fixed relative alignment in the x-y plane between the two subsystems). Each calculation shifts the overlayer by some amount in the x-y plane and then relaxes all atomic positions while fixing one overlayer atom's x-y position relative to the fixed bottom layers of the substrate. We employ a uniform 5×5 grid of x-y registries; for the cases of the Ru and

Pd substrates, we have checked that a 10 × 10 grid yields the same final results within a precision of 1 meV/Si. By averaging the binding energies over the grid of registries, we approximate the binding energy for the incommensurate case. Within this physical picture, the absolute value of the binding energy is not relevant for determining the competition between commensurate and incommensurate: it is the variation in binding energy across different registries that is to be compared to the cost of straining the overlayer.

Table 4.2 compares the total energies and their decompositions into the two contributions for 2D SiO_2 on various metal surfaces. The first observation is that all three vdW functionals give the same conclusion concerning the energetic favorability of commensurate versus incommensurate 2D SiO_2 on the substrates. In addition, the total energy differences between the two states for a given substrate are numerically very similar for the three different vdW functionals. On Pd and Ru, an incommensurate SiO_2 overlayer is found to be favorable, while on $Ni_{0.5}Pd_{0.5}$ a commensurate overlayer is predicted. Experimentally, 2D SiO_2 is known to form a crystalline incommensurate structure on Pd(111) due to its large lattice mismatch with the substrate [1]. However, in experiments, 2D bilayer SiO_2 can either form a commensurate (2×2) periodic lattice or become amorphous on Ru(0001) depending on the growth conditions [73]. The simple method developed here can only address the competition between commensurate and long-period incommensurate structures and does not say anything about the tendency for amorphous structures. A better understanding of the behavior of 2D silica on Ru will require furture work.

4.3.4 The role of chemisorbed oxygen atoms

In experiments, the 2D SiO_2 thin film is sythesized on the metal surface in an environment with a background oxygen pressure (up to 2×10^{-6} Torr) and high annealing temperature (up to 1000 K). Under these conditions, oxygens can chemically bind to and oxidize the surface. For the growth of 2D SiO_2 on Pd(111) [1], the annealingtemperature is well above the oxygen desorption temperature on the surface, thus the Pd(111) surface should have very low coverage of chemisorbed oxygens. However, the joint work of experiment and computation [72] shows that the typical growth condition of 2D SiO_2 on Ru(0001) leads to one or two chemisorbed oxygens on a (2×2) surface unit cell. Hence, it is relevant to

Substrate	Lattice	Strain energy (meV/Si)	Binding energy (meV/Si)			Total energy (meV/Si)		
			D2	vdW	vdW$^{\mathrm{surf}}$	D2	vdW	vdW$^{\mathrm{surf}}$
Ru(0001)	Commensurate	88	-226	-224	-109	-138	-136	-21
	Incommensurate	0	-165	-176	-59	-165	-176	-59
Pd(111)	Commensurate	260	-218	-139	-122	42	121	138
	Incommensurate	0	-204	-125	-108	-204	-125	-108
$Ni_{0.5}Pd_{0.5}(111)$	Commensurate	< 1	-172	-	-	-172	-	-
	Incommensurate	0	-129	-	-	-129	-	-

Table 4.2: Energies of commensurate and incommensurate hexagonal 2D bilayer SiO_2 on metal substrates using different vdW corrections (DFT-D2, DFT-vdW, and DFT-vdW$^{\mathrm{surf}}$). The zero energy is referenced by the energy of free-standing 2D SiO_2 in its relaxed lattice constant computed using DFT (5.27 Å). Ru, Pd, and $Ni_{0.5}Pd_{0.5}$ impart 3.5%, 5.8%, and 0.5% theoretical tensile strain on 2D SiO_2, respectively.

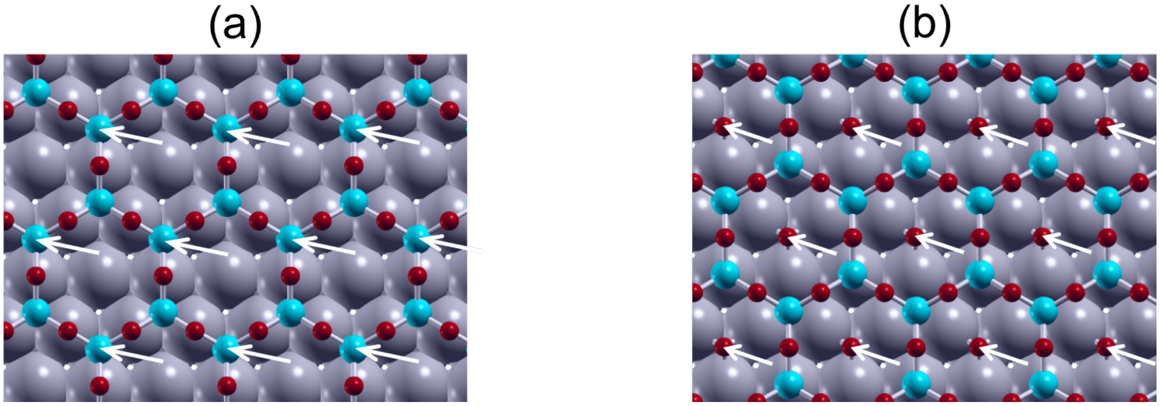

Figure 4.4: Structure of the 2D bilayer SiO_2 on "oxygen-rich" metal substrates with 1 O per (2×2) unit cell. Color scheme: Si cyan, O red, M grey (M is the metal atom in the substrate). (a) Top view of the 2D SiO_2 in registry 1 with the surface; (b) top view of the 2D SiO_2 in registry 2 with the surface. The positions of the chemisorbed oxygen are marked by the arrow. The registry 1 and 2 refer the same relative alignment of the thin film to the substrate as in Figure 4.1.

study 2D SiO_2 on metal surfaces with chemisorbed oxygens. One representative observed structure for surface oxygen adsorption is a (2×2) periodic structure, i.e., one oxygen atom adsorbed on the surface per (2×2) unit cell [99–102]. We find that the favorable binding site for oxygen is the *hcp* hollow site on Ru(0001) and the *fcc* hollow site on Pd(111) and $Ni_{0.5}Pd_{0.5}$(111). Prior studies have examined 2D SiO_2 sythesized on an "oxygen-rich" metal surface [72,76] with a focus on tuning the electronic structure of the 2D SiO_2 by varying the oxygen content on the surface. Here, we show that surface oxygen content can potentially alter the overlayer structure by changing the binding energy of 2D SiO_2.

In our calculations, the oxygen atoms are positioned at their corresponding favorable binding sites on the surfaces of Ru, Pd, and $Ni_{0.5}Pd_{0.5}$, and then 2D SiO_2 overlayers are stacked on the top of the these surfaces for structural relaxation. We find that the bond length between the adsorbed oxygen and the surface metal atom differ by at most 0.01 Å before and after the 2D SiO_2 overlayer's placement on the surface, indicating an unchanged bond to the surface for the chemisorbed oxygen. Table 4.3 shows that the binding energy of 2D SiO_2 in registry 1 becomes weaker due the presence of the chemisorbed oxygen, but the binding energy of 2D SiO_2 in registry 2 stays relatively unchanged (compare to Table 4.1). The change of d(M-O) follows the evolution of the binding energies: d(M-O)

			Ru(0001)	Pd(111)	$Ni_{0.5}Pd_{0.5}(111)$
Registry 1	d(M-O)	DFT-D2	3.53 Å	3.10 Å	3.30 Å
		DFT-vdW	3.52 Å	3.33 Å	-
		DFT-vdW^{surf}	3.77 Å	3.37 Å	-
	Binding energy/Si	DFT-D2	-122 meV	-150 meV	-104 meV
		DFT-vdW	-145 meV	-98 meV	-
		DFT-vdW^{surf}	-53 meV	-80 meV	-
Registry 2	d(M-O)	DFT-D2	3.08 Å	2.87 Å	2.96 Å
		DFT-vdW	3.25 Å	3.03 Å	-
		DFT-vdW^{surf}	3.38 Å	2.98 Å	-
	Binding energy/Si	DFT-D2	-150 meV	-190 meV	-128 meV
		DFT-vdW	-178 meV	-121 meV	-
		DFT-vdW^{surf}	-62 meV	-104 meV	-

Table 4.3: Binding energies and geometries of 2D SiO_2 on metal substrates with ordered structure of one adsorbed O per (2×2) surface unit cell. The registry 1 and registry 2 here are defined to have the same SiO_2 alignment with respect to the metal surface as Table 4.1 using the same nomenclature. The 2D SiO_2 overlayer-surface distance d(M-O) is defined in the same way as Table 4.1: it is measured by the vertical distance between the 2D SiO_2 bottom layer oxygens and top layer metal atoms on the surface. The structures of 2D SiO_2 on "oxygen rich" metal substrates with one adsorbed O per (2×2) unit cell are depicted in Figure 4.4.

becomes larger for the more weaklybound 2D SiO_2 in registry 1, but d(M-O) is essentially unchanged for 2D SiO_2 in registry 2. We attribute these changes to the repulsive interaction between the chemisorbed surface oxygen atoms and the 2D SiO_2 overlayer: in registry 1, the surface oxygen atoms are directly underneath the Si atoms and lead to repulsion, while for registry 2, the surface oxygen atoms are below the hollow center of the hexagonal rings which minimizes repulsive interactions. With the addition of the chemisorbed oxygens, the relative favorability of registry 1 and registry 2 reverses. In fact, registry 2 becomes the most favorable registry and registry 1 becomes the least favorable registry among the few registries of 2D SiO_2 that we have sampled on the "oxygen-rich" surface.

Table 4.4 compares the total energy of commensurate and incommensurate 2D SiO_2 in on oxidized metal substrates in the same way as Table 4.2 by decomposing the energy into strain and binding contributions. The three vdW corrections all give the same conclusion concerning the energetic favorability of commensurate and incommensurate 2D SiO_2 on the oxidized metal surfaces. As discovered in Sec. 4.3.3, 2D SiO_2 favors an incommensurate lattice on Ru and Pd and a commensurate lattice on $Ni_{0.5}Pd_{0.5}$. Table 4.4 shows that

Substrate	Lattice	Strain energy (meV/Si)	Binding energy (meV/Si)			Total energy (meV/Si)		
			D2	vdW	vdW$^{\mathrm{surf}}$	D2	vdW	vdW$^{\mathrm{surf}}$
Ru(0001)	Commensurate	88	−150	−178	−62	−62	−90	26
	Incommensurate	0	−136	−162	−58	−136	−162	−58
Pd(111)	Commensurate	260	−190	−121	−104	70	139	156
	Incommensurate	0	−170	−110	−92	−170	−110	−92
$Ni_{0.5}Pd_{0.5}(111)$	Commensurate	< 1	−128	-	-	−128	-	-
	Incommensurate	0	−116	-	-	−116	-	-

Table 4.4: Energies of commensurate and incommensurate hexagonal 2D bilayer SiO_2 on oxidized metal substrates with one adsorbed O per (2×2) surface unit cell using the same nomenclature as Table 4.2. The incommensurate binding energy is computed by averaging the binding energies of 2D SiO_2 (from Table 4.3) in registry 1 and 2 on oxidized metal substrates.

the binding variation becomes weaker with the presence of chemisorbed oxygen atoms on Ru(0001), thus 2D SiO_2 prefers an incommensurate lattice even more compared to a clean Ru(0001) surface. The binding variation also becomes weaker on $Ni_{0.5}Pd_{0.5}(111)$ with chemisorbed oxygen atoms, thus 2D SiO_2 prefers a commensurate lattice less compared to a clean $Ni_{0.5}Pd_{0.5}(111)$ surface. On Pd(111), the relative energy differences between commensurate and incommensurae 2D SiO_2 are numerically similar for the substrate with and withour chemisorbed oxygens.

4.4 Conclusions and outlook

In this work, we have used DFT together with three vdW corrections (i.e., DFT-D2, DFT-vdW, and DFT-vdW^{surf}) to simulate the 2D bilayer SiO_2 on three metal substrates (i.e., Ru(0001), Pd(111), and $Ni_{0.5}Pd_{0.5}(111)$). We find that the relaxed atomic geometries and binding energies for 2D SiO_2 depends on the type of vdW correction, but the relative energies for 2D SiO_2 in different registries with the substrate is similar among the three vdW corrections. We confirm that the epitaxial strain imparted by the substrate plays an important role in directing the 2D SiO_2 overlayer's morphology by comparing the energy difference between 2D silica in hexagonal and 8-6-4 structures on the Ru(0001) surface. We find that at higher tensile strain, the 8-6-4 structure is stablized over the hexagonal structure, agreeing with prior simulations on free-standing 2D SiO_2 thin films. However, depending on the growth conditions and the choice of substrates, epitaxially strained 2D SiO_2 cannot always be realized. Thus, we focus on the structural competition between crystalline hexagonal 2D SiO_2 in commensurate and incommensruate relation to the substrate. By separating the total energy of the 2D SiO_2 into two competing contributions from epitaxial strain and binding to the surface, we determine the preferred lattice formed by the overlayer 2D SiO_2. We also show that the surface chemisorbed oxygen atoms have a repulsive interaction with overlayer 2D SiO_2, altering the favorable registry of the 2D silica with respect to the metal surface.

A better understanding of the behavior of 2D SiO_2 containing non-crystalline structures (e.g., domain boundaries and amorphous regions) should be the subject of the future investigations. The FK model is a simple analytical tool that can help address the occurrence of domain boundaries that form interfaces between two crytalline regions of 2D SiO_2. Our work on the registry dependence of the binding energy and strain energy of 2D SiO_2 can provide values for the parameters defining the FK model. Finally, our sampling method that uses a commensurate overlayer in different registries with the substrate to approximate an incommensurate superlattice in the long wavelength limit should also be useful in other 2D overlayer or thin film simulations.

Chapter 5

Structure of a two-dimensional silicate layer formed by reaction with an alloy substrate

Note: This chapter is adopted from an article we have published in *ACS Chemistry of Materials* [2]. The experimental work was done by our collaborators Chao Zhou and Gregory S. Hutchings from Altman's group at Yale. The computational work was done by me.

5.1 Introduction

Transition metals have been broadly applied as substrates for two-dimensional (2D) materials growth. Most of the extensively studied 2D materials, such as graphene, h-BN, and MoS_2, have been successfully prepared on transition metal substrates by epitaxial methods [103–105]. In addition, transition metal surfaces can be oxidized to yield 2D surface oxides that are structurally distinct from their bulk oxides and can support oxides of other materials in unique 2D structures that can have a profound effect on catalysis [99,106–110]. The discrete lattice constants and chemical properties of the elemental transition metals, however, constrain the systematic study of 2D material formation on transition metal substrates. The recently reported epitaxial, solid solution, single crystalline Ni-Pd alloy films with continuously tunable lattice constant opens the possibilities to tackle this challenge [93]. This paper focuses on the growth of 2D silicates on transition metal substrates that have gained interest as 2D analogs of zeolites [69, 95, 111, 112]. It will be shown that silica deposition onto a Ni-Pd alloy substrate in an oxygen rich environment results in the self-limited growth of a 2D Ni silicate in a dioctahedral clay structure not seen in bulk Ni silicates.

Previous studies have shown that bilayer 2D silica and aluminosilicate films grown on Pd(100) [71, 92], Pd(111) [1], Pt(111) [70], and Ru(0001) [70, 74, 95, 113, 114] are composed of mirror image planes of corner-sharing SiO_4 tetrahedra, where Al can substitute for Si. The dangling-bond-free bilayer structure is preferred on substrates with weak metal–oxygen interactions compared to silicon–oxygen interactions, which leads to solely van der Waals (VDW) interactions between pure silica bilayers and the underlying substrates. When silica is deposited on metal substrates with stronger metal–oxygen interactions, such as Mo(112), a monolayer structure connected to the substrate through Si-O-metal linkages is more stable [87, 115, 116]. Ruthenium lies at the border; on Ru(0001), the monolayer structure forms until it completely covers the surface, at which point a transition to the bilayer VDW form is observed [70]. In contrast, on Pt(111) the bilayer is seen immediately at low coverages [70].

In addition to silica monolayers and bilayers, substrates that can form metal silicates adds another layer of complexity. Ruthenium, Pd, and Pt are not known to isomorphously substitute into zeolite frameworks or form silicates such as clays, while this behavior is common for the first row transition metals [117, 118]. For example, Fe can both substitute for Si in a zeolite tetrahedral site [119] and form clays in which hydrated, octahedrally coordinated Fe layers are bound to a plane of six-membered rings of corner-shared SiO_4 tetrahedra that is largely indistinguishable from monolayer 2D SiO_2 [109, 120]. The 2D VDW nature of clays opens possibilities for new classes of synthetic 2D materials that may be integrated into VDW heterostructures. Iron can form clays with Fe in the 3+ and 2+ oxidation states; the former, $Fe_2Si_2O_5(OH)_4$, is referred to as a dioctahedral clay since Fe fills 2/3 of the octahedral sites, while the latter, $Fe_3Si_4O_{10}(OH)_2$, with all of the octahedral sites filled is called a trioctahedral clay [121]. When Fe or Ti was co-deposited with Si on Ru(0001) and annealed in oxygen at high temperatures, only clay-like structures were observed [109, 110, 120, 122]. For Fe, a dioctahedral structure resembling a dehydrated Fe-clay was seen. Curiously, despite the expectation that Ti would adopt a higher oxidation state than Fe, a similar structure was seen for Ti which differed substantially from the structure of bulk layered Ti silicates. As Ni^{2+} is a common cation in clays, a Ni-containing substrate broadens the suite of competing structures upon silica deposition to include Ni silicates in addition to silica monolayers and 2D VDW silica bilayers.

In this chapter, it will be shown, based on experiment and theory, that silica deposition onto Ni-Pd(111) followed by high temperature annealing in oxygen can drive substrate Ni atoms into a 2D silicate with a non-bulk structure. Scanning tunneling microscopy (STM) imaging reveals a honeycomb structure consistent with six-membered rings of corner-sharing SiO_4 tetrahedra, superimposed on a larger moiré pattern due to a lattice mismatch between the 2D layer and the substrate. Meanwhile, surface spectroscopies indicate Ni segregation towards the surface where it can oxidize and a vibrational mode consistent with a Si–O bonding. Density functional theory calculations identify an energetically favorable Ni silicate structure with six-membered rings of corner-shared SiO_4 tetrahedra on top of a dioctahedral sheet of NiO_6 octahedra, in contrast to the trioctahedral phase observed in the bulk. Simulated polarization modulation reflection-absorption infrared spectroscopy (RAIRS) peaks coincided with the experimental spectrum. Further, simulated STM images with different overlayer registries explain observed local contrast variations across the moiré pattern. The 2D silicate layer forms through a self-limiting oxidation process which does not require precise control over the co-deposition of silica and the transition metal to form a uniform layer, highlighting the potential to create complex 2D materials through reactions with appropriate alloy substrates.

5.2 Methods

5.2.1 Experimental

Silica-containing layers were grown and characterized in an ultrahigh vacuum (UHV) system [123] equipped with an ion gun for argon ion (Ar^+) sputtering, an effusion cell holding SiO powder, a quartz crystal microbalance (QCM) deposition rate monitor, a double-pass cylindrical mirror analyzer for Auger electron spectroscopy (AES) measurements, reverse-view low-energy electron diffraction (LEED) optics, and a high-speed variable temperature STM [124]. A type-K thermocouple pressed against the sample surface with a ceramic bar was used to measure temperature. The temperature reading was cross-checked with an optical pyrometer.

The growth substrate was an approximately 50 nm thick Ni-Pd(111) film prepared through molecular beam epitaxy (MBE) on a $Cr_2O_3(0001)/Al_2O_3(0001)$ substrate in a separate UHV chamber, as described previously [93, 125]. The lattice constant of the film was measured through X-ray diffraction (XRD) recorded on a Rigaku SmartLab diffractometer with parallel beam Ge(220)×2 optics and a rotating Cu Kα anode (45 kV, 200 mA). The bulk film composition was derived from the measured lattice constant through a fit of published lattice constant versus composition data as detailed previously [93]. The film used in this study had a 3.82 Å lattice constant which corresponds to $Ni_{0.26}Pd_{0.74}$; for the remainder of this paper this material will be referred to as Ni-Pd. After reintroduction into UHV, cycles of Ar^+ sputtering and annealing at 850 K in UHV were employed to clean the film until surface contaminants were not detectable by AES and clear hexagonal patterns were observed by LEED. One monolayer equivalent (MLE) SiO (8.22×10^{14} Si atoms/cm^2) sufficient to form a single layer of six-membered rings of corner-sharing SiO_4 tetrahedra, was deposited onto the alloy substrate in 2×10^{-6} Torr background O_2 at room temperature with subsequent annealing at 950 K in the same oxygen atmosphere. Scanning tunneling microscopy measurements were performed with Pt/Ir tips made by the cut-and-pull method. The tunneling current was set between 0.05 and 1.0 nA during scanning. There were no observable changes in image contrast or detectable tip-induced surface modification over this current range. Core-level X-ray photoelectron spectra (XPS) were recorded after transferring the sample through air to a PHI VersaProbe II XPS system with a monochromatic 1486.6 eV Al Kα X-ray source. Polarization modulation reflection-absorption infrared spectroscopy (RAIRS) data were recorded using a Thermo Fisher Nicolet iS50 FTIR Spectrometer with p-polarized light at a grazing angle of 82 in a dry nitrogen environment. Following the ex situ measurements, the sample was returned to the UHV system where the sample was grown and initially characterized; after heating at 770 K in 2×10^{-6} Torr

O_2 no observable changes in the film composition or structure could be detected by AES, LEED or STM.

5.2.2 Computational

Density functional theory (DFT) [3, 4] with the Perdew-Burke-Ernzerhof generalized gradient approximation (PBE GGA) exchange-correlation functional [13] was used to study silica and Ni silicate structures on Ni-Pd alloy substrates. The numerical simulations were performed using the Quantum Espresso software package with plane wave basis with an energy cutoff of 952.40 eV, periodic boundary conditions, and norm-conserving pseudopotentials [14,15,17,126]. Due to the metallic nature of the alloy substrates in our simulations, thermal smearing by 0.14 eV of the Kohn-Sham states' occupancies is employed together with dense enough k point sampling of the Brillouin zone to achieve convergence. Two types of simulation cells were used in this work: monolayer and bilayer silica were simulated using (2×2) surface unit cell and were equipped with $(6 \times 6 \times 1)$ k point grid, while Ni silicate used $(2 \times 2\sqrt{3})$ surface unit cell and $(6 \times 4 \times 1)$ k point grid. Because of the presence of Ni atoms in the simulation, spin polarization was also included in the electronic structure calculation. Both of the substrate atoms and the Ni atoms in the overlayer were found to have non-zero local magnetic moments. The computational parameters used converged the total energies within 2 meV/atom.

The Ni-Pd random alloy substrate was modeled using the virtual crystal approximation (VCA) [94]. In the VCA model, the Ni-Pd alloy is composed of artificial "virtual" atoms whose pseudopotential is the superposition of pseudopotentials of Ni and Pd. The key formula in making the pseudopotential for the Ni_xPd_{1-x} "virtual" atom is the linear interpolation between pseudopotentials of Ni and Pd atoms:

$$V_{\mathrm{VCA}}(\mathbf{r},\mathbf{r}') = x \cdot V_{\mathrm{Ni}}(\mathbf{r},\mathbf{r}') + (1-x) \cdot V_{\mathrm{Pd}}(\mathbf{r},\mathbf{r}')$$

In our calculations, the thin film plus metallic substrate slab system was separated from its periodic images by at least 15 Å of vacuum. The semi-empirical "DFT-D" van der Waals correction [31] was also included in the structural relaxation to account for the dispersion forces. The structural relaxation was performed until every force component on every atom was less than 2.6×10^{-3} eV/Å.

Simulated RAIRS spectra were achieved by employing the "frozen phonon" method to compute the phonon modes at the Γ point, which means that each atom in the unit cell was displaced from its equilibrium position along the x, y, and z directions by 0.01 Å and the dynamical matrix was subsequently assembled from the restoring forces due to the displacement. The change in the dipole moment caused by the lattice vibrations was calculated based on the obtained zone-center phonon modes. Since RAIRS on a metal surface is only sensitive to the lattice vibrations that can induce dipole change perpendicular to the surface, the IR intensity is taken as proportional to the square of the change in dipole moments along z-axis caused by the phonon modes.

5.3 Results

5.3.1 Experimental

Auger Electron Spectroscopy was employed to track the surface stoichiometry at each processing step as shown in Figure 5.1a. Curve (i) in the figure shows only Pd and Ni Auger features after applying cleaning cycles; as described previously, the Ni/Pd peak ratio indicates that the clean Ni-Pd alloy surface is enriched in Pd [93]. After 1 MLE SiO deposition in 2×10^{-6} Torr O_2 at room temperature, curve (ii), an oxygen peak appeared at 503 eV and a silicon LVV peak appeared at 78 eV consistent with Si^{4+} [127]. At this stage, no change in the Ni/Pd peak ratio could be detected. After annealing at 950 K in 2×10^{-6} Torr O_2 for 10 min, no change in the position or intensity of the Si LVV peak could be detected in curve (iii); however, the O/Pd and Ni/Pd peak intensities increased from 0.130 to 0.698 and 0.049 to 0.252, respectively. These spectra indicate that the initial deposition does not alter the alloy surface composition, but that the high temperature oxygen annealing causes Ni migration towards the surface where it may be oxidized. The higher Ni surface energy compared to Pd can explain the initial Pd enrichment while the subsequent reversal after the oxygen anneal can be associated with Ni's higher oxygen adsorption energy [128, 129]. No further change in AES spectra were observed upon more prolonged (up to 20 min) oxygen

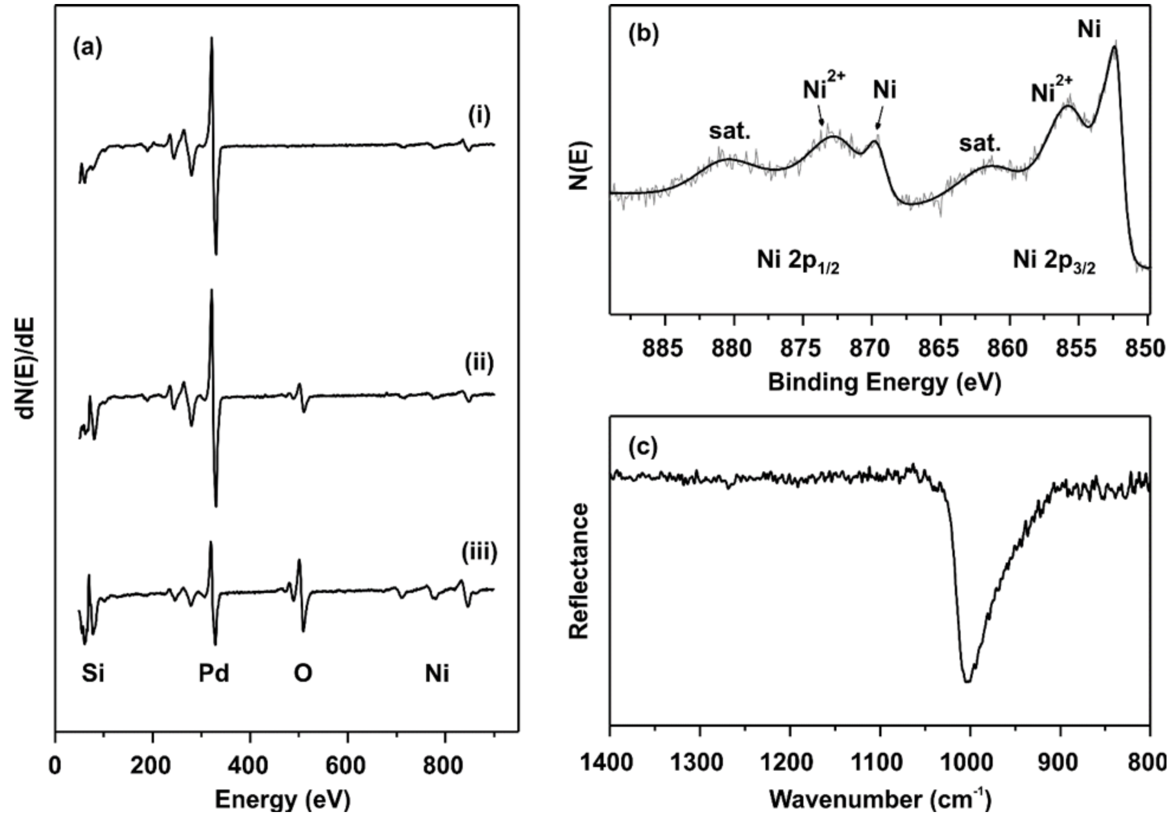

Figure 5.1: (a) Auger electron spectra recorded for: (i) bare Ni-Pd(111) substrate; (ii) after depositing enough SiO in $2{\times}10^{-6}$ Torr O_2 to form 1 MLE SiO_2; and (iii) after SiO deposition and annealing at 950 K in $2{\times}10^{-6}$ Torr O_2. Curves (i) and (ii) are normalized such that the Pd MVV peak at 330 eV has the same intensity. The same normalization factor applied to curve (ii) to match the Pd MVV intensity in curve (i) was applied to curve (iii). (b) Nickel 2p X-ray photoelectron and (c) RAIRS spectra obtained after SiO deposition and O2 annealing.

annealing at 950 K, indicating that the surface reached either an equilibrium or kinetically trapped state.

The simultaneous increase in the O and Ni AES peak intensities after oxygen annealing suggests that the Ni segregating towards the surface may have been oxidized. Possible Ni oxidation was studied using XPS. As shown in Ni 2p core level spectrum in Figure 5.1b, a Ni $2p_{3/2}$ feature at 855.4 eV consistent with Ni^{2+} confirms the formation of Ni-O bonds [130–132]. The more intense signal at 852.6 eV can be assigned to elemental Ni in the alloy substrate. Further deconvolution of the features and quantification, however, was complicated by the broad emission which could be due to Ni in bulk NiO and surface oxides in addition to a Ni silicate and metallic Ni, as well as the dependence of the relaxation processes that lead to the satellite features on the Ni environment [132, 133]. It should be noted that samples transferred through air before the high temperature annealing showed an increase in the O AES peak (O/Si peak ratio increased by a factor of 1.32, further annealing lead to another increase by a factor of 1.16) and some evidence of Ni oxidation but no increase in the overall Ni AES peak intensity; after the high temperature oxidation the peaks due to oxidized Ni intensified in tandem with the O AES peak, while neither Pd nor Si showed evidence of further oxidation in XPS.

Reflection absorption infrared spectroscopy was used to gain further insight into the bonding in the oxide layer. The absorption peak centered near 1000 cm^{-1} in Figure 1c is characteristic of Si–O stretching modes perpendicular to the surface in Si–O–metal linkages, as has been reported for silica monolayers on Mo(112) [87] and Ru(0001) [70] as well as for Ti and Fe silicates on Ru(0001) [109, 110, 120, 122]. Notably, absorption features near 1300 cm^{-1} that have been attributed to stretches of co-linear Si–O–Si bonds in 2D VDW bilayer silica were absent [70, 74]. Further, no three-dimensional quartz-like vibrational modes were detected between 1100 cm^{-1} and 1200 cm^{-1} [70, 74]. Considering the Ni oxidation state and the characteristic monolayer stretch, we propose that Ni incorporates into the film to form Ni silicate; theoretical support for this assignment is provided in the following section.

The periodicity of the surface layer was investigated using LEED. Figures 5.2a,b show the patterns obtained after silica deposition and annealing; patterns at two energies are provided to give a more complete view of the surface reciprocal unit cell. The clusters of

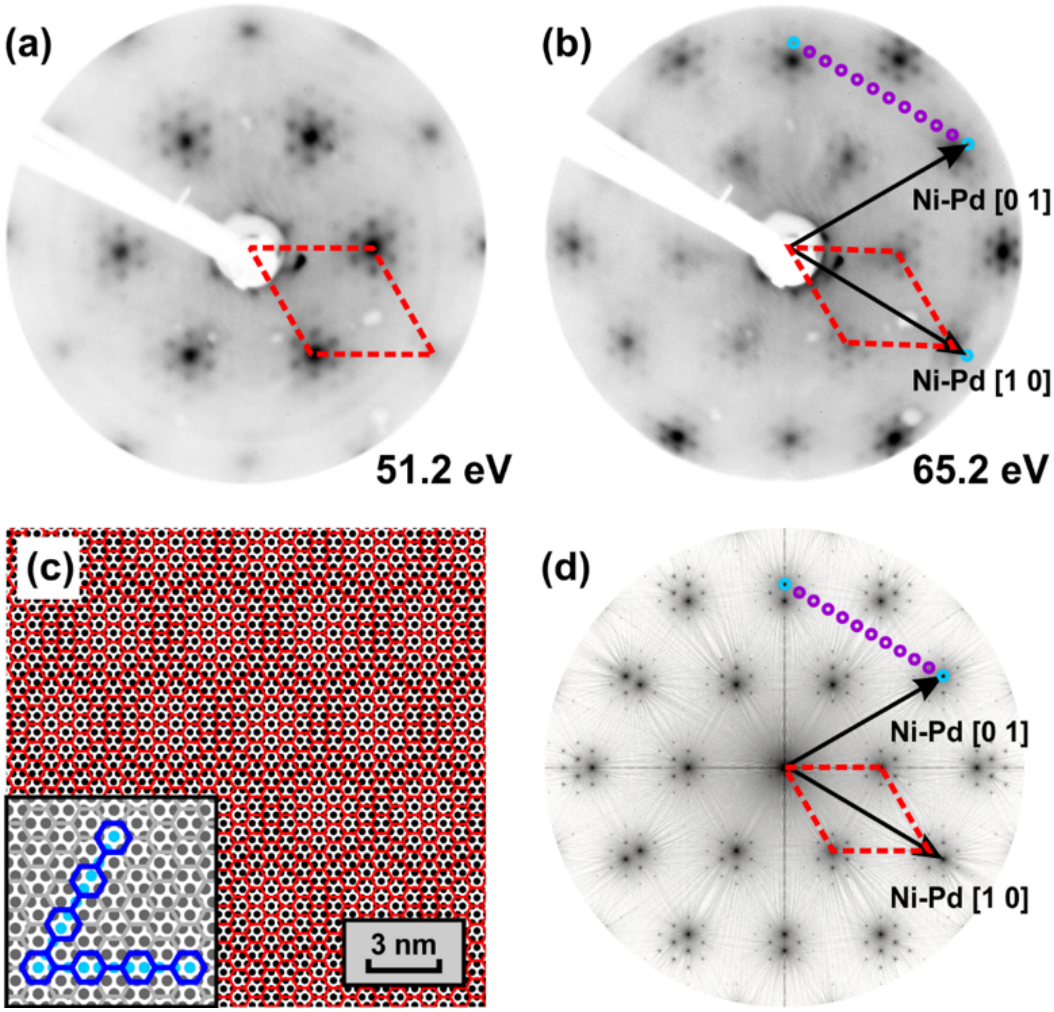

Figure 5.2: (a)(b) Low energy electron diffraction patterns obtained following silica deposition and annealing in oxygen. (c) Schematic representation of the moiré pattern achieved by rotating the overlayer [1 1] direction to align with the Ni-Pd$[\bar{1}10]$. The black dots denote the Ni-Pd substrate atom positions and the red hexagons represent the ring structure of corner-sharing SiO_4 tetrahedra found in 2D silica and silicates. In the inset, the integer multiple relation between the lattice constants of the overlayer and Ni-Pd substrate are highlighted. (d) Reciprocal space image generated by applying fast Fourier transforming the model in (c). The red dashed lines in (a), (b) and (d) highlight the overlayer reciprocal unit cell and the circles in (b) and (d) show the integer relationship between the overlayer and substrate.

satellite spots surrounding the most intense spots indicate a long-range periodicity similar to the moir patterns observed for many incommensurate thin films with a small lattice mismatch with the substrates [29,134]. By applying a similar schematic representation of the moiré pattern observed for 2D silica on Pd(111) [1], the salient features of the experimental LEED patterns could be reproduced by Fourier transforming a real space representation of the surface structure. The real space model in Figure 5.2c was constructed by rotating the [1 1] direction of a hexagonal overlayer to align with the Ni-Pd[$\bar{1}$10] direction. Based on the periodicity seen in Figures 5.2a,b and prior assignments of similar patterns seen for Fe and Ti 2D silicates on Ru(0001) [109, 110, 120], a (10×10) coincidence lattice was the starting point for the real space model. In an exact (10×10) coincidence lattice with the overlayer [1 1] direction aligned with Ni-Pd[$\bar{1}$10], $3\sqrt{3}$ times the overlayer lattice constant would equal 10 times the substrate surface lattice constant, implying an overlayer repeat length of 5.19 Å. We found a better match to the experimental LEED pattern when the overlayer repeat length was slightly smaller, 5.15 Å in Figure 5.2c. The lines of purple spots in Figures 5.2b,d demonstrate the near integer multiple relation between the reciprocal lattice constants of the Ni-Pd substrate and the overlayer.

Scanning tunneling microscopy imaging confirmed the general surface features expected from the macroscopic characterization. Figure 5.3a reveals the long-range periodicity consistent with a moiré pattern due to a small lattice mismatch between the substrate and overlayer. Meanwhile the atomic-scale images in Figure 5.3b-d show the honeycomb structure anticipated for a surface terminated by six-membered rings of corner-sharing SiO_4 tetrahedra. The images indicate a 5.35±0.10 Å repeat distance for the honeycomb, within the 5.270–5.325 Å range observed for bulk trioctahedral Ni clays, which is typical of layered silicate clays [135,136]. These lattice constants, however, are larger than the 5.15 Å implied from the LEED measurements. The moiré period determined from the STM measurements was 31±1 Å, or 9% larger than anticipated from a $(3\sqrt{3} \times 3\sqrt{3})$ repeat of the local honeycomb pattern. An exact (10×10) coincidence would still leave only 1/9 of the overlayer atoms in their favored sites; therefore, the driving force to form the (10×10) matching would be expected to be small compared to the strain energy penalty.

Closer analysis of the STM images reveals additional features inconsistent with a (10×10)

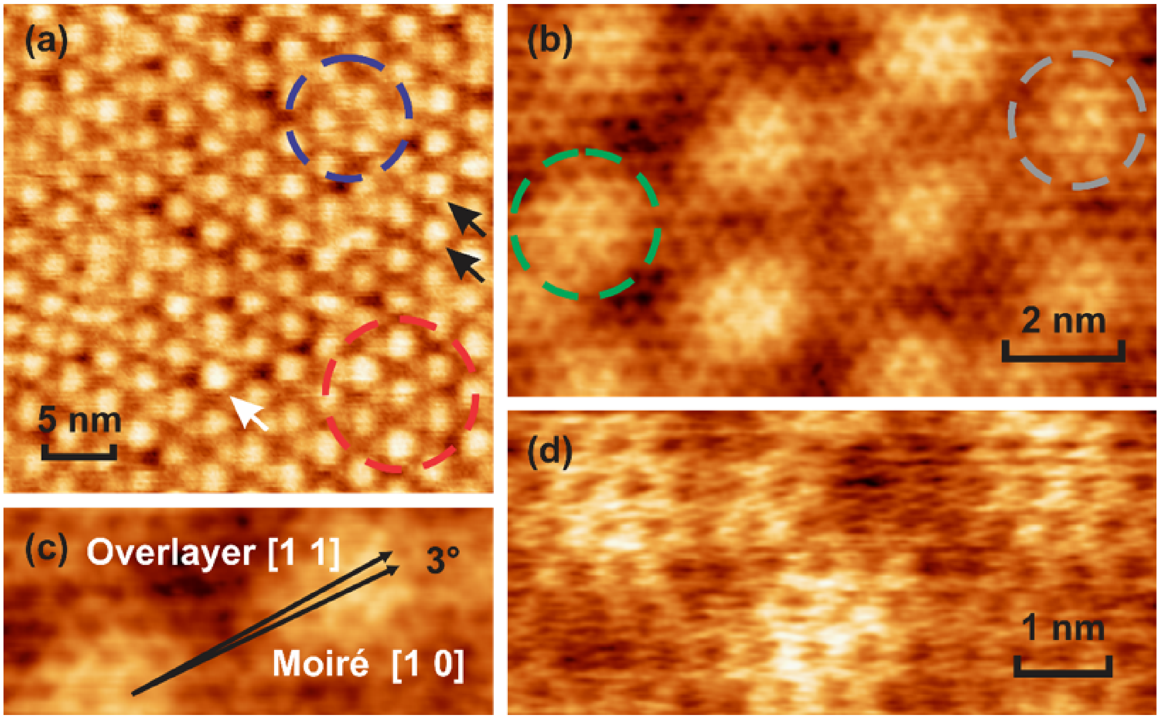

Figure 5.3: (a) Large-scale STM images obtained after silica deposition and annealing in oxygen. The blue dashed circle outlines a region with a honeycomb arrangement and the red dashed line circles a hexagonal pattern. The white arrow in the lower center points to a brighter maximum and the black arrows at the right show the appearance of secondary maxima that intensify from the bottom to the top of the image. (b)-(d) Atomic-scale images of the same surface shown in (a). (b) The hexagonal ring structures in the green dashed circle show uniform contrast while within the gray dashed circle the contrast varies around the central dark spots. (c) Zoom-in of (b) which indicates a 3° offset between the long-range and short-range periodicities; i.e. the line joining the brightest spots in the long-range periodicity is rotated from the high symmetry direction of the atomic structure by 3°. The corrugation of the long-range moiré pattern ranges from 0.55 to 0.65 Å and the local corrugation of the ring structures from 0.20 to 0.25 Å. Sample biases were (a) 0.8 V (b), (c) 1.25 V (d) 0.85 V.

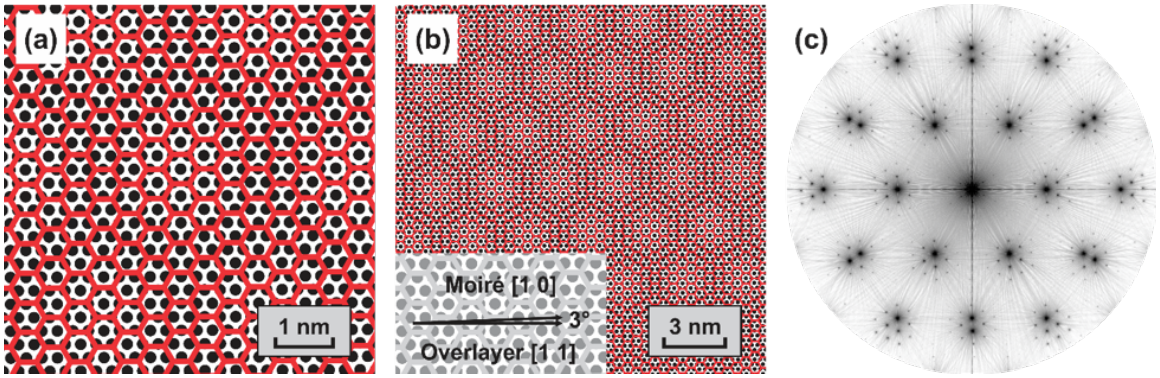

Figure 5.4: Schematic representation of the moiré pattern achieved by rotating the substrate atoms in Figure 5.2c counterclockwise by 0.3° to reproduce the rotation experimentally observed in Figure 5.3 between the moiré pattern and the high symmetry direction of the atomic structure. (a) Relative arrangement of the overlayer ring structure and substrate atoms. (b) The rotation of the moiré pattern with respect to overlayer. The arrows in the inset indicate the 3° angle between moiré [1 0] and overlayer [1 1]. (c) Reciprocal space image generated by applying fast Fourier transforming the model in (b).

coincidence lattice. Looking at Figure 5.3a, it becomes apparent that the arrangement is more complex than a simple hexagonal pattern: the bright spots in the moiré vary in intensity; the local arrangement of the bright spots appears to change from hexagonal to more of a honeycomb and; going from the lower right to the upper right of the image reveals the systematic appearance of a second maximum pointed to by the black arrows. These features are indicative of the longer-ranged periodicity expected for a film that does not relax to a structure that fits within a simple integer number of substrate lattice constants. The atomic-scale images also reveal deviations from expectations for a (10×10) coincidence lattice. Namely, the moiré [1 0] direction and local honeycomb [1 1] direction are not perfectly aligned; rather there is a small angle close to 3° between them. As has been noted for graphene on Ir(111), the angle between the moiré pattern close-packed direction and that of the substrate will be far larger than the angle between the close-packed directions of the overlayer and substrate atomic lattices [137]. Thus, the 3° mismatch can be generated by rotating the 2D silicate [1 1] direction by 0.3° with respect to Ni-Pd$[\bar{1}10]$ direction. For easier visualization, in Figure 5.4a the overlayer is fixed while the substrate atoms are rotated counterclockwise by 0.3°, which leads to a 3° angle between the moiré [1 0] and the overlayer [1 1] directions shown in Figure 5.4b. The resulting Fourier transform, Figure 5.4c is difficult to distinguish from Figure 5.2d as the angle is quite small. Since the incommensurate nature of the overlayer leaves few of the atoms in their most favored site, the energy penalty for small rotations should be modest and so small deviations from an exact (10×10) coincidence are not surprising. Finally, Figures 5.3b,d shows that the local contrast associated with the atomic-scale surface structure varies across the superstructure, even from brighter region to brighter region as highlighted by the green and grey circles, suggesting that the overlayer/substrate alignment is not identical atop neighboring moiré maxima.

5.3.2 Computational

Alloy substrates

The construction of a slab simulating the Ni-Pd alloy substrates was the starting point of the theoretical investigation. As indicated by the AES results, Ni atoms from the alloy diffuse from the bulk and segregate at the interface between the substrate and the thin film after annealing in oxygen. Therefore, we used a slab consisting of one layer of Ni atoms on top of four layers of VCA Ni_xPd_{1-x} atoms to model the metallic substrates in current work. Atoms in the two bottom layers were fixed to their bulk positions during the structural relaxation. The VCA approximation is suitable here as it reflects the random nature of the alloy system, i.e., each fcc site in the alloy is occupied by either Ni or Pd with probability x and $1 - x$.

The accuracy of employing VCA to model the alloy substrate can be exemplified through two aspects: the bulk Ni-Pd alloy lattice constant determined using the VCA method is in quantitative agreement with both experiments and explicit alloy calculations using DFT (in Table 5.1); and the one layer of Ni plus four layers of VCA slab structure yields nearly the same surface interactions as an explicit $Ni_{0.5}Pd_{0.5}$ alloy as detailed below. The previously studied silica monolayer [70] was used as a tool to probe the surface chemistry of the slab. This choice is appropriate because the silica overlayer directly forms chemical bonds with the alloy substrate. The alloy substrate was modeled as a five-layer slab of eight metal atoms in a rectangular $(2\times2\sqrt{3})$ unit cell. To construct the explicit random alloy, half of the atoms

Lattice constant	Bulk $Ni_{0.5}Pd_{0.5}$ (Å)	Bulk $Ni_{0.3}Pd_{0.7}$ (Å)
Experimental [93, 138]	3.74	3.81
VCA	3.79	3.87
Explicit alloy	3.77±0.01	

Table 5.1: Comparison between the lattice constants of Ni-Pd alloy calculated using VCA and explicit random alloys with experimental data. For $Ni_{0.5}Pd_{0.5}$, 10 random atomic configurations were sampled in 36-atom cells; the reported numbers are the average values of the 10 runs. The lattice constant of the $Ni_{0.3}Pd_{0.7}$ alloy was not computed using explicit random alloy systems, since it is very difficult to set up a simulation cell with reasonable number of atoms with the exact same chemical composition.

in the bottom four layers were randomly assigned to be Ni and the other half to be Pd. Five different random assignments were made to sample different configurations; the resulting monolayer silica binding energies were computed and compared to a $Ni_{0.5}Pd_{0.5}$ VCA alloy slab. For the VCA alloy slab, the monolayer silica binding energy was 3.41 eV/Si versus 3.22±0.02 eV/Si on explicit alloy slabs. Hence, the VCA binding energy shows only about a 6% deviation from explicit alloy calculations. In addition, the interface and overlayer geometries following the relaxations were similar in VCA and explicit alloy calculations: the Si–O–substrate bond length agrees within 0.02 Å and the bond angle agrees within 1. Both energetics and geometries confirm that the VCA method employed here is able to capture the surface chemistry of this alloy substrate.

Structural model for alloy-supported Ni silicate

With the accuracy of the VCA model for the substrate established, the next step was to investigate the structure of Ni silicate layers that may form on top of it. Two alloy compositions, $Ni_{0.5}Pd_{0.5}$ and $Ni_{0.3}Pd_{0.7}$, were studied as representative systems. These compositions were selected based on: 1) the ability to compare the $Ni_{0.5}Pd_{0.5}$ system to explicit alloys as detailed above; 2) the good lattice match between 2D SiO_2 and layered clay silicates (≈5.30 Å) with twice the calculated lattice constant of $Ni_{0.5}Pd_{0.5}$(111) (5.29 Å); and 3) the match to the experimentally studied $Ni_{0.26}Pd_{0.74}$ with a lattice constant of 3.84 Å, which splits the difference between the experimental and VCA-calculated lattice constants of $Ni_{0.3}Pd_{0.7}$. The previously studied Ru-supported Fe silicate system [109] was taken as the starting point for Ni silicate layers. Every Fe atom in the 2D Fe silicate was replaced

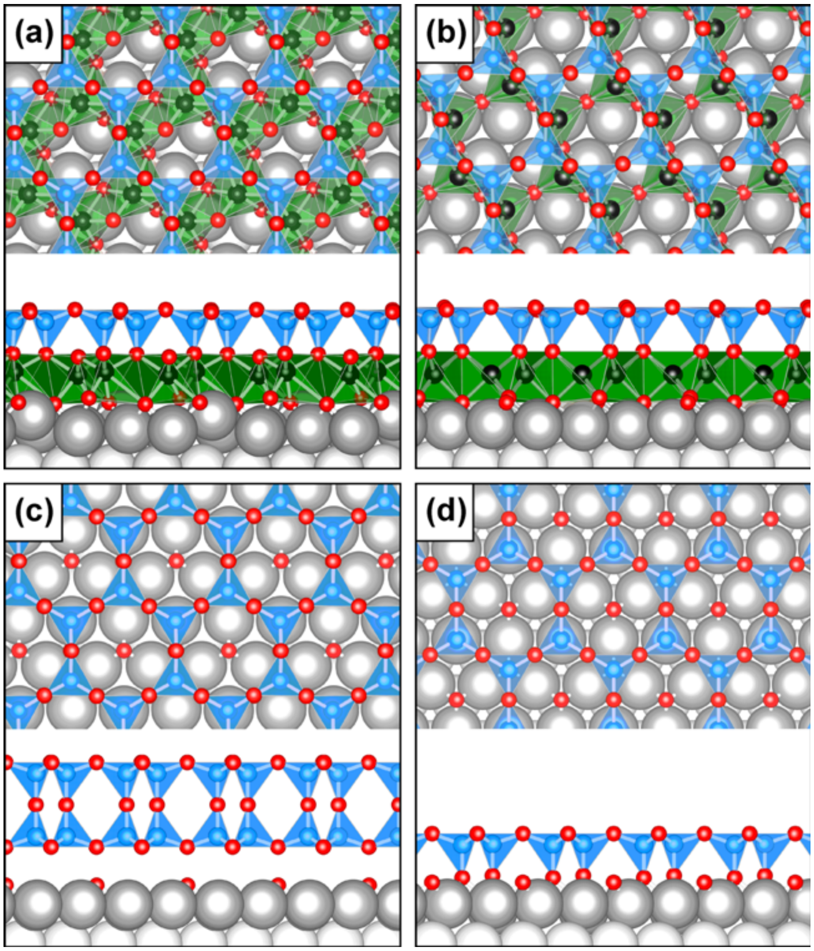

Figure 5.5: Top and side views of the most stable structures of the Ni silicate and silica thin layers on $Ni_{0.5}Pd_{0.5}$ alloy substrate (chemical formulas are shown per $(2 \times 2\sqrt{3})$ surface unit cell): (a) Ni silicate with chemisorbed oxygens on the substrate $Ni_4Si_4O_{16}{\cdot}2O/Ni_{0.5}Pd_{0.5}$. (b) Ni silicate on the clean substrate surface $Ni_4Si_4O_{16}/Ni_{0.5}Pd_{0.5}$. (c) Bilayer silica with chemisorbed oxygens on the substrate $Si_8O_{16}{\cdot}2O/Ni_{0.5}Pd_{0.5}$. (d) Monolayer silica with chemisorbed oxygens on the substrate $Si_4O_{10}{\cdot}2O/Ni_{0.5}Pd_{0.5}$. Color scheme: Si cyan, O red, Ni (in the overlayer) black, Ni (on the substrate surface) grey, Ni-Pd VCA atom white.

by Ni and the resulting Ni silicate was placed on top of a layer of Ni atoms terminating $Ni_{0.5}Pd_{0.5}$ and $Ni_{0.3}Pd_{0.7}$ alloy substrates. Chemisorbed oxygen atoms were added at the same positions seen for Fe silicate/Ru(0001) and then the structure was allowed to relax. The total chemical composition was $Ni_4Si_4O_{16}\cdot 2O$/Substrate, i.e., a Ni silicate layer with two chemisorbed oxygen atoms on the metallic substrate with $(2 \times 2\sqrt{3})$ periodicity. Such a unit cell enforces an epitaxial commensurate lattice between the Ni silicate and the substrate while in the experiment, an incommensurate overlayer on the alloy is observed. Modeling the incommensurate structure, however, would require at least 500 metal atoms (five layers of a (10×10) unit cell) making the computation intractable. Separately, the $(2 \times 2\sqrt{3})$ unit cell is compatible with monolayer and bilayer silica on metal substrates [70, 74, 95, 113, 114].

Despite the different lattice constants of the two Ni-Pd substrates, the simulation returned similar Ni silicate structures. As shown in Figure 5.5a, the most stable structure found is a top sheet of silica lying on a bottom sheet of nickel and oxygen. The top silicon oxide layer consists of corner-sharing SiO_4 tetrahedra as the building blocks, while in the nickel layer each Ni atom is locally octahedrally coordinated with six nearby oxygen atoms. The Si atoms and Ni atoms both form hexagonal six-membered rings within their sheets, but unlike in the bilayer silica where the six-membered rings in the top and bottom layers are aligned (shown in Figure 5.5c), the Si and Ni six-membered rings have a rigid shift in the x-y plane. The chemical coupling between the Ni silicate layer and the alloy substrate is also intrinsically different from the coupling between bilayer silica and the substrate. As opposed to bilayer silica which interacts weakly with the substrate through VDW dispersion forces, the Ni silicate is chemically bonded to the substrate. In the fully relaxed system, the oxygen atoms in the bottom layer of the Ni silicate are chemically coupled to the substrate. The oxygen atoms that are chemisorbed on the substrate surface in the starting atomic configuration also participate in the chemical bonding between the overlayer and the substrate after structural relaxation. Thereby these two types of oxygen atoms become indistinguishable in the final atomic configuration. The alloy substrates were found to be ferromagnetic including the Ni layer terminating their surfaces. The sheet of nickel atoms in the overlayer were also found to be ferromagnetic within this sheet but antiferromagnetically coupled to the alloy.

A structural variant of the previously described Ni silicate, i.e. the silicate thin film on the bare Ni-Pd surface without any chemisorbed oxygen, was also considered in our study. The total chemical composition for such a slab in the $(2 \times 2\sqrt{3})$ unit cell was $Ni_4Si_4O_{16}$/Substrate, with two fewer oxygen atoms per unit cell than the silicate with chemisorbed oxygen. As shown in Figure 5.5b, the Ni silicate thin film on the bare substrate also consists of a top sheet of silica stacked onto a sheet of nickel and oxygen, just like the silicate depicted in Figure 5.5a. The feature of two sheets of hexagonal six-membered rings formed by Si and Ni is also shared between the two kinds of silicate systems (see the top view in Figures 5.5a,b). Since silicate film in Figure 5.5b is missing some coordinating oxygens supplied by the substrate surface, compared to Figure 5.5a, each Ni atom in the silicate layer only has five neighboring oxygen atoms. It should also be noticed that in the fully relaxed structure shown in Figure 5.5b, the oxygen atoms participating O-Ni-O linkage in the silicate thin film move closer and become bonded to the metal surface.

Because of the chemical bonds between the Ni silicate and the substrate, the silicate cannot be treated as a separate entity in terms of its electronic structure. By projecting the electronic bands onto the Ni $3d$ orbitals of the overlayer (where the orbitals for each Ni are aligned along the local octahedral directions), the majority spin channel was found to be filled while in the minority spin channel only the t_{2g} orbitals were filled and the e_g orbitals were empty. Hence, the Ni $3d$ orbital occupations of the overlayer Ni were in accord with rock salt-structured bulk NiO where nickel is 2+ and high spin. Thus, the overlayer Ni atoms can be considered to be in a 2+ oxidation state as opposed to the value 4+ which is suggested by formal charge counting using the chemical formula of the overlayer $Ni_4Si_4O_{16}$.

There are minor differences in the atomic structures of Ni silicate on $Ni_{0.5}Pd_{0.5}$ and $Ni_{0.3}Pd_{0.7}$. The $Ni_{0.3}Pd_{0.7}$ alloy has a lattice constant about 2% large than the $Ni_{0.5}Pd_{0.5}$ alloy. As a result of the tensile strain on the system, the Ni silicate layer moves closer to the $Ni_{0.3}Pd_{0.7}$ substrate than the $Ni_{0.5}Pd_{0.5}$ substrate. For the structure with chemisorbed oxygen, the distance between the Ni silicate thin film and the Ni-Pd alloy substrates decreases from 6.03 Å for $Ni_{0.5}Pd_{0.5}$ to 5.88 Å for $Ni_{0.3}Pd_{0.7}$. The distance of the overlayer to the substrate is defined as the vertical distance between the top-most layer oxygen atoms (see Figures 5.5a,b) and the clean substrate surface (simulated separately with no overlayer placed on top).

Energetics of Ni silicate versus monolayer and bilayer silica formation

To address the question of the energetic favorability of the surface bound Ni silicate structure detailed above and monolayer and bilayer silica layers on top of the alloy substrates, the energy of the following chemical reactions were computed:

- $Si_8O_{16}\cdot 2O$/Substrate (bilayer silica) + 4NiO + $O_2 \rightarrow Ni_4Si_4O_{16}$/Sub + $4SiO_2$ (α-quartz)

  $\Delta E = -1.51$ eV per Ni atom on $Ni_{0.5}Pd_{0.5}$ alloy substrate.

  $\Delta E = -1.18$ eV per Ni atom on $Ni_{0.3}Pd_{0.7}$ alloy substrate.

- $Si_8O_{16}\cdot 2O$/Substrate (bilayer silica) + 4NiO + $2O_2 \rightarrow Ni_4Si_4O_{16}\cdot 2O$/Sub + $4SiO_2$ (α-quartz)

  $\Delta E = -1.31$ eV per Ni atom on $Ni_{0.5}Pd_{0.5}$ alloy substrate.

  $\Delta E = -1.70$ eV per Ni atom on $Ni_{0.3}Pd_{0.7}$ alloy substrate.

In the chemical reactions shown above, the two kinds of Ni silicates are both energetically favored over silica in bilayer form. We also considered reactions starting with a dispersed silica monolayer (Fig. 5.5d) which can be more relevant to the situation at hand since the experiments involved deposition of 1 MLE Si. These reactions are as follows:

- $Si_4O_{10}\cdot 2O$/Substrate (monolayer silica) + 4NiO $\rightarrow Ni_4Si_4O_{16}$/Sub

  $\Delta E = -0.05$ eV per Ni atom on $Ni_{0.5}Pd_{0.5}$ alloy substrate.

  $\Delta E = 0.25$ eV per Ni atom on $Ni_{0.3}Pd_{0.7}$ alloy substrate.

- $Si_4O_{10}\cdot 2O$/Substrate (monolayer silica) + 4NiO + $O_2 \rightarrow Ni_4Si_4O_{16}\cdot 2O$/Sub

  $\Delta E = 0.16$ eV per Ni atom on $Ni_{0.5}Pd_{0.5}$ alloy substrate.

  $\Delta E = -0.27$ eV per Ni atom on $Ni_{0.3}Pd_{0.7}$ alloy substrate.

These results indicate the energetic favorability between the two kinds of Ni silicate and monolayer silica depends on the substrate's chemical composition. Higher Ni concentration in the substrate favors the Ni silicate on the clean surface more while higher Pd concentration favors the Ni silicate on the surface with chemisorbed oxygens more. *First-principles atomistic thermodynamics* [139] were also used to compute the surface free energies of the structures displayed in Figure 5.5 in order to shine some light on their relative energetics under the experimental conditions. The Ni silicate on the bare surface was found to be the most stable structure under the typical growth conditions in this work ($T = 950$ K, oxygen partial pressure $\sim 10^{-6}$ Torr).

Though the exact product of the experimental growth should be further examined using DFT simulated IR spectroscopies, a simple conclusion can be drawn: the energetic favorability of the Ni silicate structure together with the experiments showing Ni segregation to the interface, Ni oxidation at the interface, formation of Si–O–Ni bonds, and a local honeycomb structure all support the formation of a 2D Ni silicate surface layer.

Hydrated Ni silicate in its bulk trioctahedral clay form has a layered structure with VDW inter-layer interactions. One layer of the bulk Ni silicate clay structure with various levels of dehydration was considered as another structural candidate for the overlayer. All were found to be less stable than the Ni silicate structure proposed above using the DFT simulations.

Simulated RAIRS spectra

To further help identify the structure of the overlayer, simulated IR spectra were computed for the structural models on the $Ni_{0.5}Pd_{0.5}$ substrate depicted in Figure 5.5. Figure 5.6 shows that the monolayer and bilayer silica (Figures 5.5c,d) have primary IR peaks near 1100 cm^{-1} and 1250 cm^{-1}, respectively, both deviating from the peak around 1000 cm^{-1} found in the experiment. The only structure with computed peaks near 1000 cm^{-1} was the Ni silicate on bare $Ni_{0.5}Pd_{0.5}$ which agrees with the experiments much closer than the silicate thin film on the oxygen saturated metal surface. However, the broadness of the peak near 1000 cm^{-1} seen in the experiments could be explained by Ni silicate with and without chemisorbed oxygen coexisting on the surface, or by the incommensuration in the experiment creating a distribution of vibrational frequencies that could not be addressed in our calculation. Therefore, the simulated IR spectra confirms that we have a silicate, but

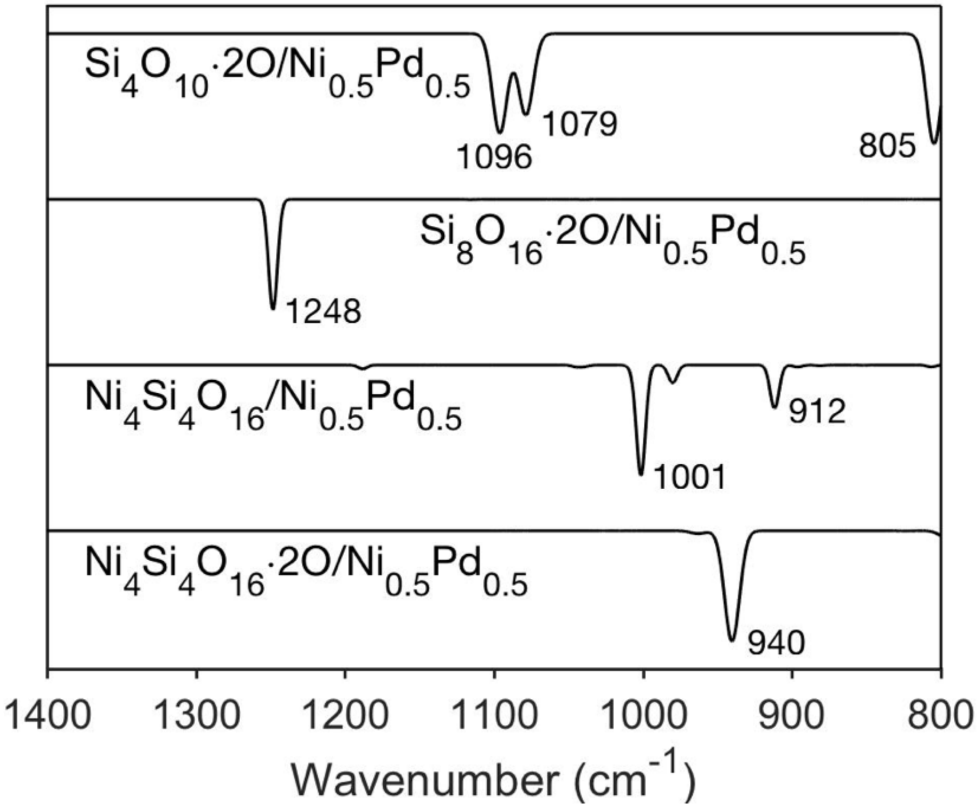

Figure 5.6: RAIRS spectra simulated for the structures depicted in Figure 5.5. The simulated IR peaks are broadened by a 3.0 cm^{-1} Gaussian smearing with the largest peak scaled to 1 (in arbitrary unit) for each structure.

it cannot differentiate between the two silicates with/without interfacial oxygens.

Simulated STM Contrast

Scanning tunneling microscopy images of Ni silicate layers on alloy substrates were simulated using the Tersoff-Hamann approximation [140]. The tunneling current in STM at low bias is proportional to the projected local density of states (LDOS) at the location of the tip in the Tersoff-Hamann approximation. We used the computed LDOS above the surface to represent the STM images. To be consistent with experiment, constant-density images are provided here. A 0.8 V bias voltage was applied to the sample to match the typical bias voltage in experiments. Hence, the STM images probe unoccupied states within the energy window between E_F and $E_F + 0.8$ eV, where E_F is the Fermi level. While it is difficult to determine the exact height of the tip in the experiments, tip heights in Tersoff-Hamann models are typically considered to be smaller than experimental heights [141]. The theoretical reduction of the surface-tip distance stems from the difficulty in computing the exponentially small LDOS as it decays away from the surface; numerical noise in the computed LDOS overshadow the images at large heights. A range of different setpoint densities (and corresponding mean tip heights) were considered and the results were qualitatively similar until numerical noise became substantial. The setpoint density in this paper was chosen to produce the simulated STM images with reasonable quality (see figures below). Tip heights are defined as the vertical distance above the top layer of metal atoms of the bare alloy surface.

Due to the similarities in the atomic structures of Ni silicate thin films on the $Ni_{0.5}Pd_{0.5}$ and $Ni_{0.3}Pd_{0.7}$ substrates, STM calculations were only performed for the former. We looked at the Ni silicate surface layer with and without chemisorbed oxygen. Figure 5.7a shows the simulated STM images corresponding to the silicate film shown in Figure 5.5b, while Figure 5.7b corresponds to Figure 5.5a. They both display the six-membered ring structures with the brighter spot located on the positions of the oxygen atoms in the top sheet of the silica layer. It should be noticed that the interfacial oxygen atoms affected the magnitude of the tunneling current. Figures 5.7a,b were calculated using different setpoint densities in the LDOS which corresponds to different tunneling current. We also tried to use the same setpoint density to probe the STM image for structure in Figures 5.5a,b and found that the resulting mean tip height was different by ∼2 Å between the two systems. Since no big tip height changes were seen in the experimental STM images, there was no evidence supporting distinct phases of silicate with and without interfacial oxygen coexisting on the alloy surface. Therefore, again we cannot make a conclusive statement about the extent of interfacial oxygen.

The moiré pattern observed in the experiments indicates that the Ni silicate layer is incommensurate with respect to the alloy substrate. The incommensuration results in different local registries with the substrate which can cause topographic, electronic and contrast changes. Disentangling these different effects was of particular interest for the theoretical simulations. We used the Ni silicate on the alloy surface with chemisorbed oxy-

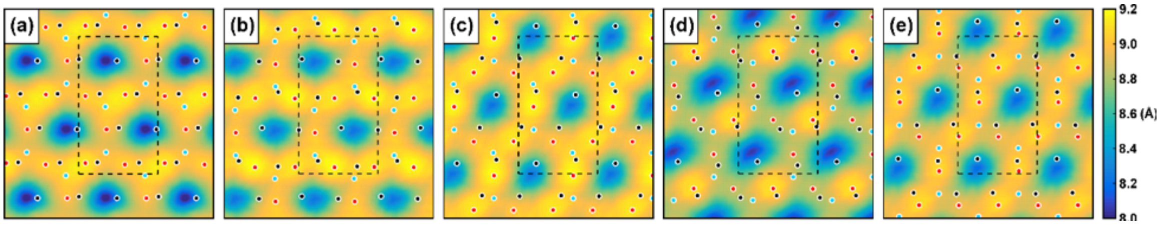

Figure 5.7: Simulated STM images of Ni silicate on $Ni_{0.5}Pd_{0.5}$ alloy substrates. (a) Ni silicate on $Ni_{0.5}Pd_{0.5}$ without interfacial oxygen. (b)-(e) Ni silicate with chemisorbed oxygens initialized at different sites on the surface: (b) on the hcp hollow site; (c) on the fcc hollow site; (d) on top of one substrate atom (e) on the bridge site. The color bar maps the color from the simulated images to the tip height in STM. The locations of top layer Si and O atoms are marked here relative to the metal atoms in the top layer of the alloy substrate so that the different registries of the thin film can be visually identified. Color scheme of the atoms: Si cyan; O red; top layer of the alloy substrate black. The dashed boxes highlight the computational unit cells.

	Registry (b) hcp hollow site	Registry (c) fcc hollow site	Registry (d) top site	Registry (e) bridge site
Energy (meV/Ni)	0.0	4.9	79.8	78.3
Layer thickness (Å)	6.03	6.04	5.94	5.97
Mean tip height (Å)	8.91	8.91	8.74	8.84
Image corrugation (Å)	0.96	0.96	1.07	0.91

Table 5.2: Summaries of the key features (energy, atomic structure and simulated STM images) of different registries. The energy of Ni silicate thin film in registry (b) is set to be zero as a reference. The layer thickness is defined as the vertical distance between the top-most oxygen atoms (see Figure 5.5a) and the clean substrate surface with no silicate layer on top. The mean tip height is computed by averaging every data point for each individual registry. The image corrugation is measured by taking the difference in the tip height between highest and lowest positions in each simulated image.

gens to exemplify the registry effect on the STM images since it was easier to define the registries with the interfacial oxygens. In the DFT simulations, the different local registries were examined by fixing the chemisorbed oxygen atoms at different high symmetry sites on the substrate surface, which caused the Ni silicate layer to dutifully follow through the structural relaxation process. Figures 5.7b-e show results for four Ni silicate registries on the $Ni_{0.5}Pd_{0.5}$ alloy substrate. Notice that the images in Figure 5.7b-e were generated using the same setpoint density in the LDOS. The configuration in Figure 5.7b (corresponding to the model in Figure 5.5a) is the energetically most favorable registry and starts with the chemisorbed oxygen in hcp sites. Table 5.2 summarizes the key features of the different registries appearing in Figure 5.7. A few things become apparent from the Table: the energy differences between the two hollow configurations is small but the on-top and bridge configurations are significantly less favorable; topography accounts for any observed height differences between bridge and hollow sites; and electronic and topographic differences contribute roughly equally to observed height differences between hollow and on-top sites. The computed atomic corrugation of 1.07 Å is significantly larger than the 0.06 Å observed experimentally which may be due to factors such as differences in tip–sample separation and neglect of the impact of the tip in the simulations. In Figure 5.7 we can see that the most prominent feature for all of the registries is the depression at the center of the six-membered rings as was observed in the experimental STM images in Figures 5.3b,d. The distorted, non-hexagonal six-membered rings in the simulated images have bright spots overlapping with the hexagonal rings of silicon oxides in the outermost layer of the sample. In accord with the data in Table 5.2, the image in Figure 5.7d for the on-top starting configuration appears to be overall dimmer than the other three registries. The other distinction of note is the much more obvious contrast around the bright ring in Figure 5.7d where every other oxygen atom appears considerably brighter. This can be seen in the experimental image in Figure 5.3b where in the region circled by the green dashed line the six-membered ring appears uniform while in the region circled out by grey dashed lines there are brighter and dimmer spots around the ring. Taken together, the results support a relaxed surface layer, not constrained to a small integer repeat of the substrate lattice constant.

5.4 Discussion

The combined experimental and computational results indicate that depositing 1 MLE silica onto Ni-Pd alloy substrates and annealing in an oxygen-rich environment produces a thermodynamically stable, two-dimensional, non-bulk structured nickel silicate. In contrast to previously studied silicate thin film growth and 2D substrate bound non-bulk oxides on elemental metal substrates [107, 108], Ni atoms from the alloy segregate to the interface and incorporate into the silicate structure. This formation route has several advantages. The self-limiting nature of the process makes the 2D silicate formation insensitive to the annealing time. In addition, the calculations indicate that nickel silicate formation is energetically favored over a range of alloy compositions. Therefore, using an alloy substrate with a reactive component can alleviate the need to carefully control the atomic ratios during deposition to achieve desired structures. There are structural similarities between the 2D Ni silicate on the Ni-Pd alloy substrate reported here and previous studies on 2D Fe and Ti silicates on Ru(0001) [109, 110]. In all cases, LEED patterns that are close to (10×10) are observed. For the 2D Ni silicate on the alloy substrate, however, it is shown that the STM images cannot be explained by the relatively small coincidence lattice. Further, straining to match a (10×10) superstructure would compress the silicate overlayer by 2.4% but still leave few of the atoms in their favored binding sites, which raises questions about the driving force to form the relatively small coincidence lattice. Lastly, Figure 5.4 shows that it can be challenging to distinguish closely related coincidence lattices with LEED. Given the challenge in distinguishing similar coincidence lattices with LEED and the expectation that the driving force to form structures with few atoms in preferred sites would be small, caution should be exercised in determining overlayer lattice constants from LEED coincidence patterns alone.

Interestingly, the metal-supported 2D Ti, Fe and Ni silicates all display structures that can be classified as dioctahedral clays despite differences in the structures of bulk layered silicates containing these transition metal ions. Charge balancing plays a key role in how cations fill octahedral sites in clay layers. With 2+ the preferred valence state of Ni in oxides, the structure of bulk Ni silicate is similar to lizardite, $Mg_3Si_2O_5(OH)_4$, where divalent cations fill all of the octahedral sites below the Si2O5 tetrahedral sheet creating a trioctahedral 1:1 clay (1:1 refers to one tetrahedral sheet per octahedral sheet). In contrast, dioctahedral clays with Fe^{3+} filling two thirds of the octahedral sites are common [119,121]. The important distinction between the metal-supported 2D Ni silicate structure and unsupported bulk compounds can be attributed to the interaction with the metal substrate and chemisorbed oxygen at its surface, which serve as a reservoir to balance the otherwise excess positive charge on the silicate Ni. The calculations show that this electron donation from the substrate leaves a positive charge on the 2D silicate Ni characteristic of bulk oxides. The nominal compositions (excluding the substrate and adsorbed oxygen) of all of the metal-supported silicates are $M_4Si_4O_{16}$, where M = Ti, Fe, Ni. This implies that the metal substrate can flexibly donate between nominally zero electrons for Ti^{4+} to two electrons for Ni^{2+} to stabilize the 2D silicate.

Chapter 6

Tuning two-dimensional silica and silicate growth on $\mathbf{Ni}_x\mathbf{Pd}_{1-x}$(111) alloy substrates through epitaxial strain and growth conditions

Note: This chapter is adopted from a paper manuscript that we have submitted to *Nanoscale*. The experimental work was done by our collaborators Chao Zhou and Gregory S. Hutchings from Altman's group at Yale. The computational work was done by me.

6.1 Introduction

Two-dimensional (2D) van der Waals (VDW) heterostructures realized by stacking layers of 2D materials have attracted intense interest in recent years. Two popular methods are broadly employed to construct 2D VDW heterostructures. One is the direct mechanical assembly method involving delamination of individual layers followed by alignment and stacking of 2D layers [29,134,142]. The other is an epitaxial approach, which follows bottom-up methodology and potentially benefits from larger 2D materials domains [143, 144] and fewer contaminants at the interface between layers [103–105]. A challenge with the epitaxial approach, however, is that the 2D layers of interest often exhibit multiple phases close in energy but with different properties [145–147]. Substrate interactions, lattice mismatch, and growth conditions all potentially play decisive roles in the phase that forms. In this research, the effect of growth conditions and epitaxial strain on the structure and formation of 2D silica and silicates on a series of $\mathrm{Ni}_x\mathrm{Pd}_{1-x}(111)$ substrates was systematically studied. It will be shown that adjusting the growth conditions can allow selection between 2D VDW silica and 2D Ni silicate phases and that the maximum epitaxial strain that can be imparted on the latter can be determined by varying the alloy substrate composition.

Epitaxial strain engineering has long been a tool to adjust the properties of three-dimensional (3D) materials [147]. While many 2D VDW materials also exhibit strain-dependent properties [148–150], using substrate lattice mismatch to apply the strain may be limited because 2D materials interactions are often dominated by weak VDW forces. An important question is thus how much strain can a substrate impart on a 2D material. The case of graphene as a canonical 2D VDW material is instructive to consider in this context. Free-standing graphene layers display a six-membered ring structure with different sized rings at domain boundaries [151]. Graphene layers grown on substrates show the same atomic structure; however, it is typically superimposed on top of a longer range moiré pattern and the graphene lattice constant does not change more than 1.2% [152, 153]. The moiré pattern is due to incommensuration between the graphene and the substrate, indicating that the graphene layer relaxes to its favored free-standing lattice constant and is not strained to match the substrate. Theoretical investigations of the impact of strain on graphene, however predict that a Haeckelite structure composed of four- to eight-membered rings can become favored at large tensile strains, estimated to be in the vicinity of 10% [154, 155]. Meanwhile, molecular dynamics simulations indicate that Haeckelite structures may also be trapped as a metastable intermediate during graphene formation on metal substrates [156]. Since the ≈10% strain required to favor Haeckelite formation is well in excess of what can be applied through epitaxy, metastability would appear to be the only viable route to achieving non-ground state 2D carbon structures. On the other hand, the recently discovered 2D form of silica is predicted to have experimentally accessible strain-induced phase transitions, making it an attractive system for investigating methods to induce phase transitions and defects in honeycomb-structured 2D layers [77].

Two-dimensional silica bilayer can be considered an analog of graphene with SiO_4 tetrahedra replacing C atoms in the graphene structure [88,90,112,157,158]. The dangling bonds in a single plane of corner-sharing SiO_4 tetrahedra can be tied up by bonding to a metal substrate or through connections to a mirror-image plane of corner-sharing SiO_4 tetrahedra to form a 2D VDW bilayer [73, 74]. Similar to graphene, six-membered ring structures are favored; however, an amorphous phase composed of four- through nine-membered rings is also observed [75, 89–92, 159]. Consistent with experimental observations, theory indicates that structures incorporating different-sized rings are close in energy to the favored six-membered ring structure [73, 77, 91, 92]. Further, a modest 2.5% tensile strain is predicted to induce a phase transition to a structure incorporating four- and eight-membered rings [77]. Experimental results for single component metal surfaces are encouraging. On Ru(0001) with a tensile lattice mismatch of 2.1%, commensurate crystalline 2D silica is observed together with an amorphous phase [89]. On Pt(111) with a 4.7% tensile mismatch, only the amorphous phase has been seen [70]. An incommensurate crystalline phase has been seen on Pd(111) with 3.8% tensile mismatch [1]. Meanwhile on Pd(100), the growth is commensurate along [011] and incommensurate along $[01\bar{1}]$ with nearly regular defects observed along the commensurate direction that were attributed to the 3.8% uniaxial strain [71]. Together the experimental results suggest that the substrate can impart at least close to the biaxial tensile strain needed to induce a phase transition, making 2D VDW silica growth on alloys where the strain can tuned through the range predicted to induce phase transitions appealing. In this research the recently developed $Ni_xPd_{1-x}(111)$ epitaxial alloy system was chosen as the substrate because it forms a continuous solid solution with lattice constants that vary the strain from compressive to tensile [93, 138].

The above discussion focuses on the impact of the substrate lattice constant, but the chemical nature of the metal substrate and the growth conditions also play roles in determining the structures that form. Prior results on pure metals highlight the relative strengths of Si–O and substrate metal–O bonds, and the Si coverage as key factors in determining the structures that form. For second and third row transition metals, Ru is at the dividing line for forming 2D VDW silica. When the amount of deposited silicon atoms are precisely controlled to form only one sheet of SiO_4 tetrahedra, a 2D monolayer structure can form on Ru(0001) which connects to the substrate through Si-O-Ru linkages [73]. The amount of silicon in this case is denoted as 1 monolayer equivalent (MLE). When 2 MLE silicon atoms are deposited, only the bilayer VDW structure can be detected. There is a coexistence of monolayer and bilayer structures when the coverage falls between 1 – 2 MLE; above 2 MLE, bulk 3D silica forms. To the left of Ru on the periodic table, only the 2D monolayer is seen on Mo, and Si deposition in excess of 1 MLE leads to 3D silica [87,116,160]. To the right of Ru, only the bilayer has been seen on Pd and Pt. The first row transition metals introduce the additional complication of the ability to form 2D silicates [121,161]. When Fe and Ti were co-deposited with Si onto Ru(0001) and processed in oxygen, clay-like structures were observed in which a layer of six-membered rings of corner-sharing SiO_4 tetrahedra is stacked over a hexagonal layer of FeO_6 and TiO_6 octahedra; the octahedral sheet is connected to the alloy substrate through chemical bonds [109,110,120]. When 1 MLE Si was deposited onto an $Ni_xPd_{1-x}(111)$ alloy substrate, Ni segregated to the interface and formed a 2D Ni silicate similar to the Fe and Ti silicates [2].

Two-dimensional monolayer, bilayer, and Fe and Ti silicates are all formed through a high temperature annealing process in oxygen. The quenching process is thought to influence the crystallinity of the overlayer. Both monolayer and bilayer silica show planar crystallinity when annealed in oxygen followed by slow cool; however, amorphous bilayer silica was observed under an increased cooling rate [89,159]. The impact of the oxygen pressure during annealing has not been investigated but can be intriguing for growth on Ni_xPd_{1-x}. While Ni is easier to oxidize than Pd, it is more difficult to oxidize than Ti or Fe and thus it may be possible to find an oxygen chemical potential where silica remains stable but Ni does not oxidize, thereby making it possible to form 2D VDW silica.

In this paper, it will be shown that an amorphous 2D VDW silica phase can be achieved on $Ni_xPd_{1-x}(111)$ substrate by limiting the oxygen pressure during the high temperature annealing step. Density functional theory (DFT) calculations indicate that by varying the oxygen partial pressure and increasing the silicon supply, both 2D VDW silica and Ni silicate can be thermodynamically stable. For the Ni silicate, the structure was studied systematically as a function of alloy composition and thus strain. A commensurate to incommensurate transition was observed between 1.12% and 1.40% tensile mismatch, experimentally pinpointing the maximum epitaxial strain.

6.2 Experimental Method

Following a previously reported recipe, 20 – 50 nm thick $Ni_xPd_{1-x}(111)$ films were grown in ultra-high vacuum (UHV) by molecular beam epitaxial (MBE) films on 15 nm thick $Cr_2O_3(0001)$ films grown on $Al_2O_3(0001)$ [93]. The lattice constants and thicknesses of the alloy films were determined by X-ray Diffraction and X-ray Reflectivity data collected on a Rigaku SmartLab diffractometer. The alloy compositions were calculated from the measured lattice constant based on a quadratic approximation of Vegard's law [93, 162].

Following growth, the $Ni_xPd_{1-x}(111)$ films were transferred through air to another UHV system where silica-containing films were prepared and characterized. This UHV system was equipped with a double-pass cylindrical mirror analyzer for Auger electron spectroscopy (AES) measurements, reverse-view low-energy electron diffraction (LEED) optics, and a high-speed variable temperature scanning tunneling microscope (STM) [124]. The sample temperature was measured with a type-K thermocouple pressed against sample surface and was cross checked with a pyrometer.

After exposure to air, the $Ni_xPd_{1-x}(111)$ films were cleaned by repeated cycles of Ar ion sputtering and post-annealing at 850 K in UHV. The Si source for the films was SiO deposited onto the substrates at room temperature [2]. The SiO thickness and the oxygen pressure during deposition and during annealing were varied to target specific surface structures as detailed in the Results section.

Cut-and-pulled Pt/Ir tips were used for STM measurements. The tunneling current was set between 0.05 and 1.0 nA during scanning; no observable effects on the images were detected over this current range. Polarization modulation reflection-absorption infrared spectroscopy (RAIRS) data were recorded in a dry nitrogen environment using a ThermoFisher Nicolet iS50 FTIR Spectrometer with the light incident at a grazing angle of 82°. LEED patterns taken down to lower energies were recorded within an Elmitec LEEM-III low energy electron microscope (LEEM). Prior work in our lab has demonstrated that exposing silica-covered Pd and $\mathrm{Ni}_x\mathrm{Pd}_{1-x}$ alloy samples to ambient conditions has no effect on the structure of the silica-containing layer [2, 71].

6.3 Computational Method

Density functional theory (DFT) [3,4] with the Perdew-Burke-Ernzerhof generalized gradient approximation (PBE GGA) [13] exchange-correlation functional was used for the computational work. Various phases of silica and Ni silicate on the Ni-Pd(111) alloy substrate were considered in the simulation. The parameters for the first principles calculations and the construction of $\mathrm{Ni}_x\mathrm{Pd}_{1-x}$ alloy substrate using virtual crystal approximation (VCA) [94] in this work have been detailed in a prior paper [2]. The computational parameters were sufficient to converge the total energy within 2 meV per atom. In the calculations, the slab systems were separated from their periodic images by at least 15 Å of vacuum to reduce artifacts introduced by slab-slab interactions. The structural relaxations were performed until the all force components on all atoms were below 2.6×10^{-3} eV/Å (10^{-4} Ry/a_0 where a_0 is the Bohr radius).

Density functional theory calculations were carried out to understand the observed 2D silica/Ni silicate phase separation on $\mathrm{Ni}_x\mathrm{Pd}_{1-x}(111)$. As detailed below, a series of 2D silica and Ni silicate phases on $\mathrm{Ni}_{0.5}\mathrm{Pd}_{0.5}(111)$ were considered [2]. The DFT calculations yielded the minimum energy structures for each phase at 0 K and zero oxygen partial pressure. Understanding and predicting the phases that form, however, requires theoretical methods that take into account the experimental conditions. *First-principles atomistic thermodynamics* developed by Reuter and Scheffler was employed to tackle this task [139]. The method in the context of our study is briefly described below.

6.3.1 First-principles atomistic thermodynamics

The model slab for 2D silica and silicate phases can be thought of as in equilibrium with "reservoirs" of Si, O, and Ni with chemical potentials μ_i (i = Si, O, and Ni) that are defined by reference gas or bulk crystal phases. By allowing the slab to exchange atoms with the reservoirs at different chemical potentials, relative energies between phases can be compared at experimental conditions (e.g. the temperature and oxygen partial pressure that determine the value of μ_{O}). The thermodynamically most stable 2D phase on the surface can be determined by the one with the lowest surface free energy (per unit area) for the slab system, which is defined as

$$\gamma(\{\mu_i\}) = \frac{1}{A} \cdot \left[G - \sum_i N_i \cdot \mu_i \right] \tag{6.1}$$

where G is the Gibbs free energy of the solid with the surface. Since only the relative energies are of interest, N_i is taken as the excess number of atoms of the i^{th} species in the system relative to the clean $\mathrm{Ni_{0.5}Pd_{0.5}}$ surface which is deemed to be the baseline structure for comparison. As a result, the chemical potential term corresponding to the $\mathrm{Ni_{0.5}Pd_{0.5}}$ virtual atoms in the bulk drops out. The bottom surface of the slab was held fixed to the corresponding bulk configuration in the simulations, hence, the surface area A in Eq. (6.1) is equal to the area of one side of the surface unit cell. For example, for the clean $\mathrm{Ni_{0.5}Pd_{0.5}}$ surface phase, $N_{\mathrm{Si}} = N_{\mathrm{O}} = N_{\mathrm{Ni}} = 0$ in Eq. (6.1). For other phases, the changes in the surface free energy which eliminates the influence of the bottom surface and alloy bulk were examined, and the phase that yields the lowest surface energy as a function of μ_i (i = Si, O, and Ni) were selected to map the phase diagram. The gap between the ground state energy and the Gibbs free energy is bridged by approximating G with the DFT total energy E_{DFT} [163]. Therefore, replacing G with E_{DFT} gives the following equation used to evaluate the surface free energy in this work:

$$\gamma(\{\mu_i\}) = \frac{1}{A} \cdot \left[E_{\mathrm{DFT}} - \sum_i N_i \cdot \mu_i \right] \tag{6.2}$$

6.3.2 Chemical potentials

The chemical potentials μ_i (i = Si, O, and Ni) in Eq. (6.2) can be determined using the conditions under which the experiments are carried out. The oxygen chemical potential is referenced to the total energy of an isolated O_2 molecule (per atom) at zero temperature. It is well known that the PBE functional overestimates the binding energy of O_2 [164]. Thus, instead of using the DFT total energy of O_2, the oxygen chemical potential was referred to the DFT total energy of an oxygen atom plus one half of the experimental O_2 atomization energy to provide a better comparison between theory and experiment. Experimental temperature and oxygen partial pressure was mapped to μ_{O} using standard thermochemical tables [165]. The determination of the Si chemical potential is more challenging: in principle, it can be approximated using the DFT total energy of crystalline Si at 0 K plus the integral of its heat capacity from 0 K to the temperature T of interest for bulk phase Si. However, this number would be of limited utility for comparison to the experiments where the supply of Si is in the form of a one-time fixed amount deposition rather than in the form of a constant vapor pressure under constant temperature (which leads to constant chemical potentials). Nonetheless, the relationship μ_{Si} increasing with increased Si availability still holds. μ_{Si} in this paper is referenced by the DFT total energy of bulk, diamond cubic Si per atom $E_{\mathrm{DFT}}^{\mathrm{Si}}$. Nickel atoms participating in the formation of the 2D surface phases are supplied by the alloy substrate. The alloy substrate is treated as an ideal binary solution in equilibrium with its constituent metals, making μ_{Ni} equal to the Gibbs free energy of bulk Ni per atom, which is later approximated by the DFT total energy of bulk Ni per atom $E_{\mathrm{DFT}}^{\mathrm{Ni}}$.

6.4 Experimental results

6.4.1 Impact of growth conditions

It was shown in the previous chapter that a 2D Ni silicate forms on $\mathrm{Ni}_x\mathrm{Pd}_{1-x}(111)$ when 1 MLE SiO is deposited in 2×10^{-6} Torr oxygen at 300 K and then annealed at 950 K in the same oxygen rich environment [2]. Under such preparation condition, 2D Ni silicate formation is a self-limited process and does not strongly depend on the substrate alloy composition. In the following context, substrates with compositions ranging from 52% to 93% Pd are referred as Ni-Pd(111) without loss of generality. Here the objective was to determine if the Si-O-Ni bonding in the 2D Ni silicate could be avoided by varying the silica coverage, the oxygen partial pressure, and the annealing temperature, thereby producing 2D VDW silica. RAIRS is an effective technique to distinguish 2D Ni silicate from 2D VDW silica. Both experiment and theory have shown that the signature absorption peak of Si–O

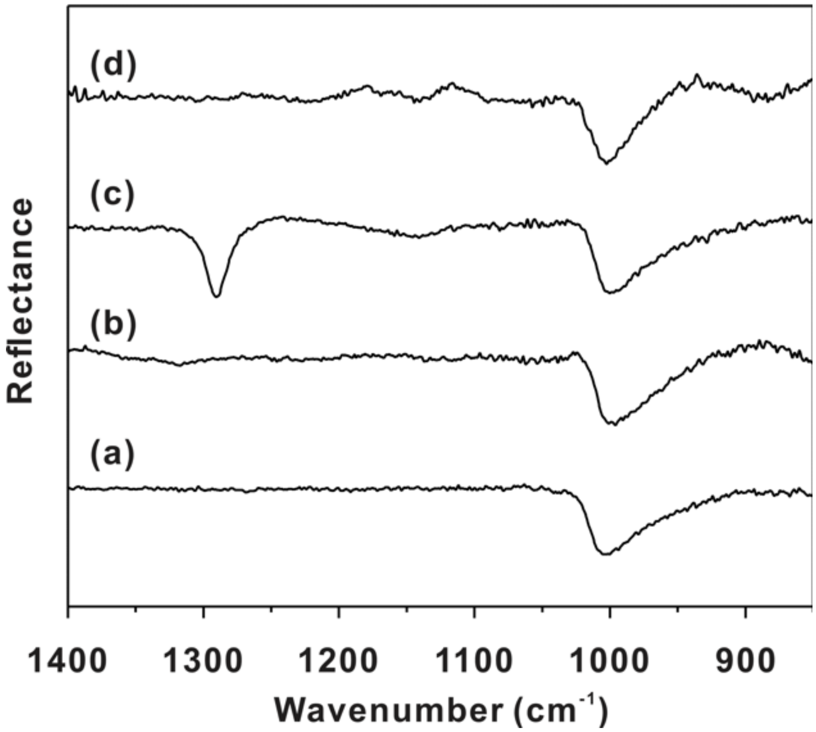

Figure 6.1: Reflection-absorption infrared spectra recorded following SiO deposition onto $Ni_xPd_{1-x}(111)$ under different preparation conditions. (a) After annealing at 950 K in 2×10^{-6} Torr oxygen for 10 minutes with 1 MLE SiO deposited on $Ni_{0.32}Pd_{0.68}(111)$, (b) After annealing at 950 K in 2×10^{-6} Torr oxygen for 10 minutes with 2 MLE SiO deposited on $Ni_{0.32}Pd_{0.68}(111)$, (c) After annealing at 950 K in 4×10^{-8} Torr oxygen for 5 minutes with 2 MLE SiO deposited on $Ni_{0.48}Pd_{0.52}(111)$ in UHV, and (d) After further annealing the sample shown in Curve (c) at 1000 K in 4×10^{-8} Torr oxygen for 10 minutes.

stretches in Si–O–Ni linkage lies near 1000 cm^{-1} [2], while stretching the Si–O–Si bonds that connect the two halves of the bilayer features an absorption peak near 1300 cm^{-1}, with a small substrate-dependent shift [70, 73, 74]. Thus RAIRS was employed to determine the structure of silica-containing overlayers prepared under various conditions.

Figure 6.1 compares the RAIRS spectra for a series of silica overlayers prepared under different conditions. Curve (a) in Figure 6.1 shows a typical RAIRS spectrum of 2D Ni silicate prepared by 1 MLE SiO deposition and annealing at 950 K in 2×10^{-6} Torr O_2 with a peak at 1000 cm^{-1}. For these growth conditions, no detectable change could be observed in the RAIRS spectrum within the alloy composition range studied (deposition onto pure Pd yields only the characteristic bilayer peak under these conditions [1]). As shown by Curve (b), increasing the amount of SiO deposited to 2 MLE while keeping the other growth conditions the same still produces the prominent 1000 cm^{-1} peak characteristic of 2D Ni silicate, with no evidence of the bilayer-associated peak near 1300 cm^{-1}. In this case, the excessive silica forms clusters on top of Ni silicate monolayer which can be observed in STM. Those bulk silica clusters may have a smaller IR cross-section or no preferred orientation for RAIRS, which would preclude their detection by RAIRS. The high reactivity of Ni towards O compared to the metals on which 2D VDW silica has been observed (Cu [166], Ru [157], Pd [1,71,92], and Pt [70]) suggests that Ni oxidation is the impediment to forming 2D VDW silica. Therefore, reducing the oxygen pressure to attempt avoid Ni silicate formation was investigated. It was found that 4×10^{-8} Torr was the lowest O_2 pressure at which silica on Ni-Pd alloy substrates could be annealed above 900 K and remain on the surface without decomposition as determined by AES. Therefore, 2 MLE SiO was deposited onto Ni-Pd(111) substrates in UHV (background pressure less than 5×10^{-9} Torr) and then annealed in 4×10^{-8} Torr O_2 at 950 K for 5 minutes. Over the Pd composition range studied, no distinct differences could be observed in AES, RAIRS and LEED measurements. Taking the film grown on $Ni_{0.48}Pd_{0.52}(111)$ substrate as a representative example, both the 2D VDW bilayer silica feature near 1300 cm^{-1} and the 2D Ni silicate feature near 1000 cm^{-1} could now be detected as shown in Figure 6.1 curve (c) which indicates that reducing the oxygen pressure can inhibit Ni silicate formation. AES indicates that Si is fully oxidized to Si^{4+} state despite of the low oxygen partial pressure.

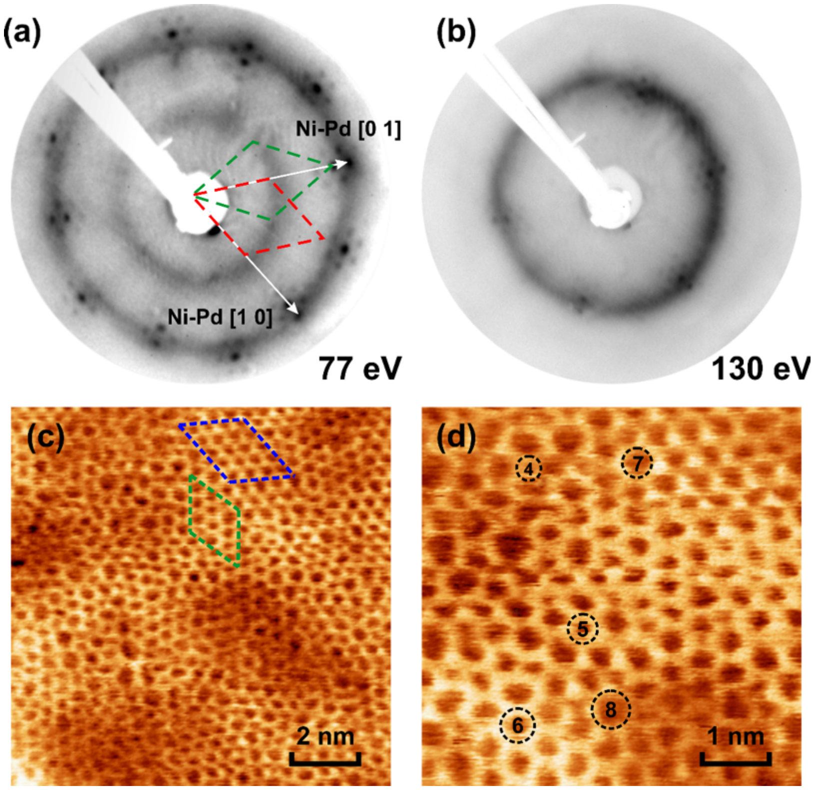

Figure 6.2: LEED and STM taken on the sample where Ni silicate and bilayer silica coexist. (a)(b) LEED pattern taken at different electron energies. The red dashed line and green dashed line in (a) indicate the unit cells of commensurate and incommensurate Ni silicate phases in reciprocal space. The arrows show the primary directions of the substrate cells. (c)(d) STM images taken at different scales. The green and blue dashed lines in (c) enclose two crystalline regions with different orientation. The circles and numbers in (d) indicate representative 4- to 8-member silica rings.

The surface covered by co-existing 2D VDW silica and Ni silicate was further characterized by LEED and STM. As shown in Figures 6.2a,b, , LEED patterns revealed both a diffraction ring and discrete spots with a spacing indicative of a long-range periodicity. Previous studies on metal-supported 2D Ni, Ti and Fe silicates have shown similar long-range periodicity that originates from moiré features due to an incommensurate crystalline silicate phase [2,109,110,120,122]. Meanwhile, similar ring features have been seen for amorphous 2D VDW silica on Pd(100) [92], Pt(111) [70], and Ru(0001) [89,159]. No amorphous transition metal silicate phases have been reported for either bulk or single layer materials [119]. Thus, the ring features in the LEED patterns can be attributed to amorphous 2D VDW silica.

The corresponding STM images of the surface that gave the LEED patterns in Figures 6.2a,b show the coexistence of amorphous and crystalline regions. As shown in the wide range image in Figure 6.2c, the amorphous phase appears to cover most of the surface. Two small crystalline domains encompassing 12 and 16 unit cells are enclosed by green and blue dashed lines, respectively. The orientation of the two crystalline regions differ by 30 °, matching the observation of two crystalline domains in LEED. Due to the limited extent of the crystalline regions, no moiré pattern could be seen with STM. As highlighted in the higher resolution image in Figure 6.2d, the amorphous region is composed of four- through eight- membered rings which is typical of previous reports on 2D amorphous silica [89,111].

As noted above, the expectation is that the amorphous region corresponds to 2D VDW silica implying that Ni silicate is responsible for the crystalline regions. Silica, however, can exist in both amorphous and crystalline forms and it is difficult to distinguish crystalline silica from silicate as both show honeycomb patterns in STM images [109,110,120]. DFT calculations described in detail below indicate that the weaker VDW interaction of the 2D silica with the substrate is predicted to move the top honeycomb silica sheet 1.31 Å further from the metal surface; however, the chemical bonding of the Ni silicate to the substrate creates a stronger film-substrate electronic coupling which can offset the topographic height difference in STM images. In addition, the registry of the overlayer with respect to the substrate also induces contrast variations [2]. The image in Figure 6.2c does not show uniform contrast with the crystalline domains tending to appear brighter or higher, but not

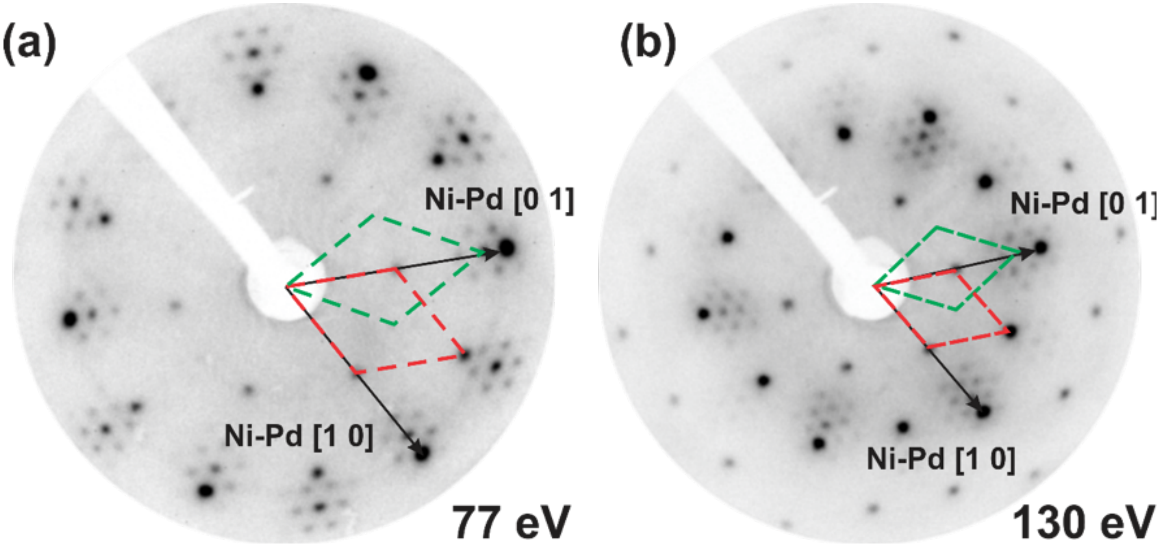

Figure 6.3: LEED pattern after annealing the sample shown in Figure 6.2 at 1000 K in 4×10^{-8} Torr oxygen for 10 minutes. The red dashed line and green dashed line indicate the unit cells of commensurate and incommensurate (rotated 30° overlayer in reciprocal space. The arrows show the substrate $\langle 1\ 0 \rangle$ directions.

uniformly so. Therefore, crystalline domains in the STM images cannot be unambiguously assigned to Ni silicate.

In addition to silicon coverage and oxygen pressure, the effects of annealing time and temperature on the phases that form were also explored while holding the oxygen pressure at 4×10^{-8} Torr. Taking the mixed 2D silica/Ni silicate on $Ni_{0.48}Pd_{0.52}(111)$ system shown in Figure 6.2 as the starting point, the LEED patterns in Figure 6.3 show that another annealing with the temperature increased to 1000 K for 10 min caused the amorphous ring to disappear and the crystalline spots to become more prominent. This observation could be explained by the crystallization of amorphous 2D silica, the decomposition of 2D silica into volatile SiO and oxygen at high temperature and low oxygen pressure [167], or the disproportionation of 2D silica into 2D Ni silicate plus 3D silica. The RAIRS data in Curve (d) Figure 6.1 recorded after the additional annealing shows only the vibration associated with Ni silicate, eliminating 2D silica crystallization as a possibility. Increasing the oxygen pressure to 2×10^{-6} Torr while fixing the annealing temperature at 950 K also eliminated 2D silica vibrational features from a surface initially supporting co-existing 2D silica and Ni silicate, implying that 2D VDW silica can disproportionate into 2D Ni silicate plus 3D

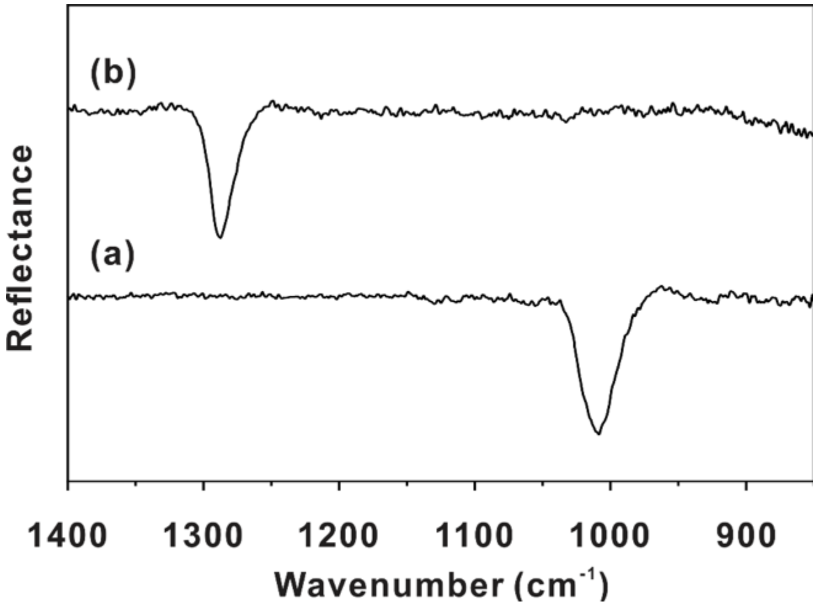

Figure 6.4: Comparison of RAIRS spectra for (a) SiO deposited onto $Ni_{0.07}Pd_{0.93}(111)$ and annealed at 1000 K in 2×10^{-6} Torr O_2 and (b) 2D VDW silica on Pd(111). The peak position in (a) is indicative of 2D Ni silicate formation.

silica clusters.

6.4.2 Strain effects on 2D Ni silicate formation

Previously it was shown that 1 MLE silica on $Ni_xPd_{1-x}(111)$ can lead to a 2D Ni silicate over a range of Ni concentrations [2]. However, the previous chapter also suggests the formation of a commensurate phase on $Ni_{0.55}Pd_{0.45}(111)$ with a surface lattice constant of 3.72 Å and an incommensurate phase on $Ni_{0.26}Pd_{0.74}(111)$ with a surface lattice constant 3.82 Å [93]. To find the maximum mismatch strain that could be imparted, the structure of a series of overlayers was characterized as a function of alloy substrate composition. The annealing conditions, 1000 K in 2×10^{-6} Torr O_2 for 10 min, were selected to produce only the 2D Ni silicate as indicated by the representative RAIRS data in Figure 6.1. In addition, Figure 6.4 shows that very little Ni in the alloy can lead to Ni silicate formation: the RAIRS spectrum in Figure 6.4a for 7% Ni shows the characteristic Ni silicate feature near 1000 cm^{-1} while the spectrum in Figure 6.4b for elemental Pd(111) shows the characteristic 2D VDW silica peak near 1300 cm^{-1}. Thus any structural changes induced by increasing the Pd concentration in the alloy can be attributed to increased lattice mismatch.

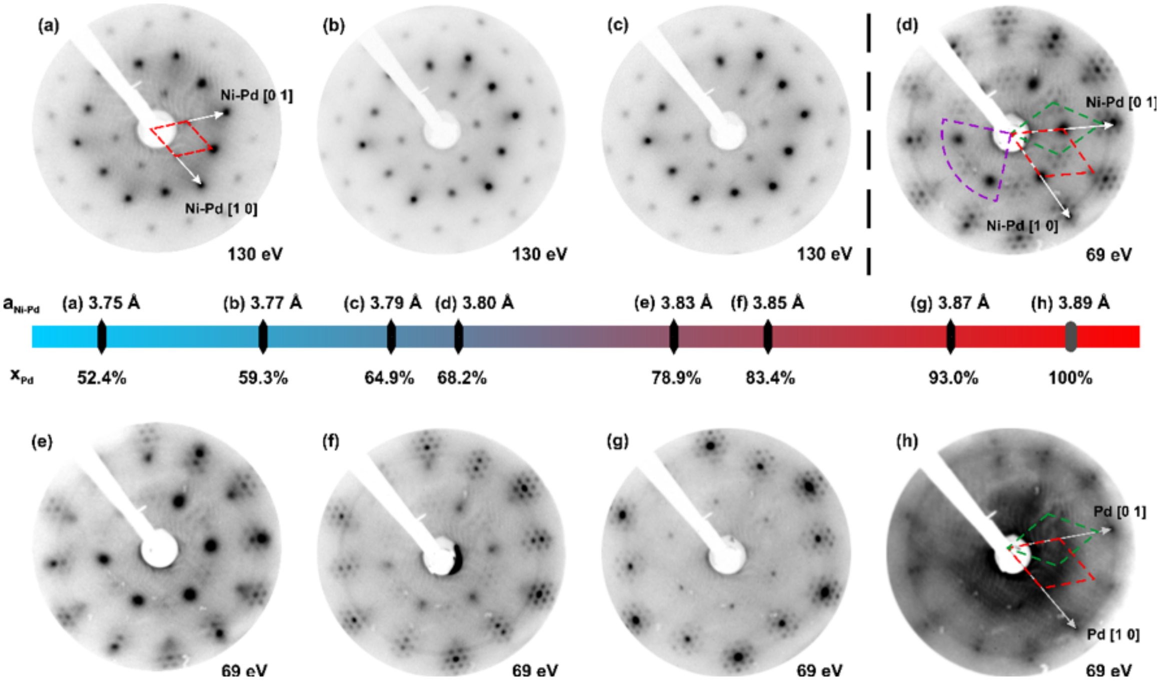

Figure 6.5: Commensurate-incommensurate transition of Ni silicate with respect to Ni-Pd(111) composition shown by LEED results. (a)-(c) Ni silicate films with only commensurate crystalline phase. (d)-(g) Ni silicate films with the coexistence of incommensurate and commensurate crystalline phase. (h) 2D VDW silica with commensurate and incommensurate crystalline phases. In (a), (d) and (h), the red dashed line and green dashed line indicate the unit cells of non-rotated and rotated overlayer phases in reciprocal space and the arrows show the primary directions of the substrates. The region enclosed by purple dashed line in (d) is better resolved by a LEEM system and is shown in Figure 6.6. The lattice constant of Ni-Pd substrates and corresponding Pd composition is labeled on the color bar.

Figure 6.6 shows a series of LEED patterns recorded as the substrate Pd concentration was varied between 52.4% – 100%. The patterns in Figures 6.5a-c, indicate a commensurate (2×2) structure and thus an epitaxially strained 2D Ni silicate layer. At larger mismatches, clusters of satellite spots appear in the LEED patterns which indicates longer range periodicities typical of an unstrained, incommensurate surface phase. Focusing on the pattern for $Ni_{0.32}Pd_{0.68}(111)$ in Figure 6.5d, two sets of spots can be seen that are rotated 30 ° with respect to one another. In the figure, the green dashed lines highlight a reciprocal primitive unit cell of an overlayer rotated 30 ° with respect to the alloy substrate, and the red dashed lines an overlayer with its [1 0] direction aligned with that of the substrate. Satellite spots clearly surround the former, as would be expected since there is no small integer match between the expected 5.30 Å lattice constant of the silicate and $\sqrt{3}$ times the substrate surface lattice constant, 4.65 Å. Compared to Figure 6.5a-c, the spots for the non-rotated domain appear more diffuse, suggesting that the spots corresponding to this domain may also be composed of closely spaced spots that could not be resolved. Better-resolved LEED patterns corresponding to the region enclosed by the purple dashed line in Figure 6.5d were recorded down to lower energies within a LEEM system; the results are shown in Figure 6.6 for a beam energy of 15.7 eV. Here satellite spots can be seen surrounding the (10) spots of both overlayer domains. The tighter spacing of the non-rotated domain is consistent with the small 1.40% mismatch which leads to a longer-range moiré periodicity than the 30 rotated domain. The implication is that the 2D silicate has relaxed to its favored lattice constant in both domains. The coexistence of the rotated and non-rotated phases can be observed in Figures 6.5d-f; however, the spots of the non-rotated phase became dimmer as the substrate lattice constant increased and in Figure 6.5g it is difficult to distinguish the non-rotated phase. Thus the results indicate an increasing preference for the rotated phase as the mismatch increases. For completeness, LEED data for pure Pd(111) are shown in Figure 6.5h. In this case the LEED pattern is much more diffuse with comparatively blurry satellite spots, but the data still indicate a crystalline incommensurate phase, which matches previously reported results [1]. Taken together, the data indicate that the transition from strained commensurate to relaxed incommensurate 2D Ni silicate lies between substrate lattice constants of 3.79 Å (2.68 Å surface lattice constant) and 3.80 Å (2.69 Å

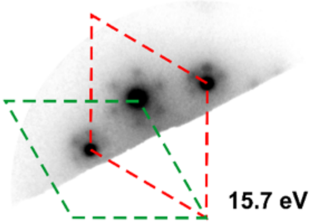

Figure 6.6: High-resolution LEED patterns corresponding to the region enclosed by purple dashed line in Figure 6.4d. The red dashed line and green dashed line indicate the unit cells of two crystalline regions. The red dashed line corresponds to the non-rotated phase. The green dashed line corresponds to the phase rotated by 30.

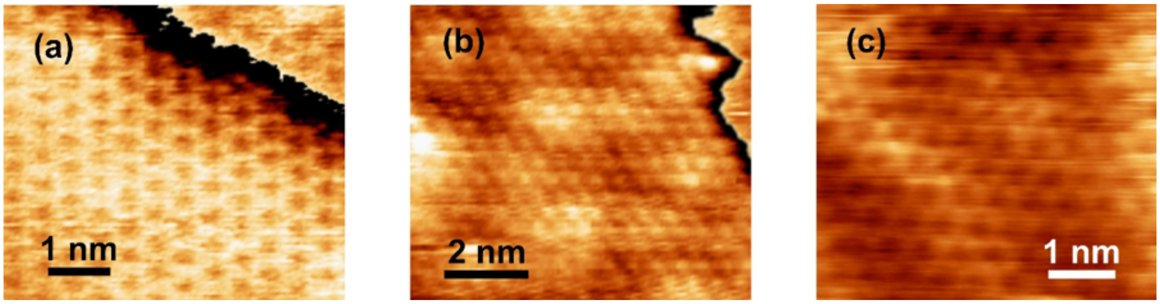

Figure 6.7: Scanning tunneling microscopy images taken on (a) commensurate crystalline Ni silicate on $\mathrm{Ni_{0.48}Pd_{0.52}(111)}$, (b) incommensurate crystalline Ni silicate on $\mathrm{Ni_{0.26}Pd_{0.74}(111)}$, and (c) incommensurate crystalline 2D VDW silica on Pd(111).

surface lattice constant), which corresponds to Pd concentrations of 64.9% and 68.2%, respectively. Presuming a typical single sheet layered silicate lattice constant of 5.30 Å, this corresponds to a tensile lattice strain between 1.12% and 1.40%.

Scanning tunneling microscopy data reinforce the conclusions drawn from the LEED data. Representative STM images recorded above and below the phase transition are provided in Figure 6.7. Figure 6.7a shows a honeycomb structure with no long-range structure, consistent with a commensurate (2×2) structure. Meanwhile, Figure 6.7b shows a moiré pattern superimposed on a hexagonal atomic-scale structure. The image in Figure 6.7c shows the six-membered ring structure of crystalline 2D VDW silica on Pd(111) which also shows contrast variations due to lattice mismatch.

It should be noted that the 2D Ni silicate formed directly on $\mathrm{Ni_{0.48}Pd_{0.52}(111)}$ in oxygen rich environments only shows commensurate (2×2) domains (Figure 6.5a) while the LEED patterns shown in Figures 6.2 and 6.3 reveal the presence of the rotated incommensurate phase when the surface passes through a state in which 2D VDW silica and 2D Ni silicate coexist. The potential reasons for these differences will be addressed in the Discussion section.

6.5 Computational results

6.5.1 Competition between 2D silica and silicate phases on Ni-Pd(111)

The thrust of the theoretical effort was to understand how the growth conditions influence whether 2D silica or Ni silicate forms on the alloy surface, and thus only 2D surface phases were considered. Though evidence presented suggests that 2D VDW silica can disproportionate into 2D Ni silicate plus 3D SiO_2, modeling this situation would require detailed knowledge of the exposed 3D cluster facets and their surface and interfacial energies, which is beyond the scope of the current paper. The alloy composition chosen was $Ni_{0.5}Pd_{0.5}$ because twice its computed (111) surface lattice (5.29 Å) is a good match to twice that of theoretical free-standing 2D silica (5.27 Å) and 2D layered Ni silicate in the trioctahedral clay form (5.30 Å). The computed alloy lattice constant matches the experimental value within a few thousandths of an Ångstrom [2, 93]. As shown in Figure 6.5, in this alloy composition range, the 2D Ni silicate forms a commensurate (2×2) structure. Consistent with this observation, the 2D phases were modeled using either the rectangular $(2 \times 2\sqrt{3})$ surface unit cell or the hexagonal (2×2) surface unit cell. Enforcing the epitaxial match imposes only a tiny strain on the 2D layers, e.g. only 0.3% tensile strain on the 2D VDW silica. Although 2D VDW silica was observed in its amorphous form, prior work indicates that the amorphous phase is only slightly higher in energy than the crystalline form [77]. Structures selected for the 2D phase diagram calculation included: the bare alloy surface, a Si_2O_5 monolayer, bilayer VDW SiO2, and Ni silicate, all with and without an additional chemisorbed oxygen atom per (2×2) surface unit cell (Figure 6.8). All overlayers are assumed to sit on a Ni layer atop the alloy substrate because AES data show Ni segregation to the interface following SiO deposition and high temperature annealing. Structural models for monolayer and bilayer silica (Figures 6.8c-f) were taken from the previous results [73,74]. The atomic structure of Ni silicate thin film has been the subject of the previous chapter [2]. In the fully relaxed Ni silicate thin film (Figures 6.8g,h), a sheet of Si tetrahedra is stacked over a nickel oxide sheet which couples to the alloy substrate through the Ni–O–Substrate chemical bonds. The Si and Ni atoms both form hexagonal six-membered rings within their own sheet, but the two sets of the six-membered rings have a rigid shift in the x-y plane, unlike the bilayer silica where the six-membered rings in the top and bottom sheets are aligned (Figures 6.8e,f).

6.5.2 The phase diagram

The DFT predictions of the stable 2D phases on the $Ni_{0.5}Pd_{0.5}$ alloy are compiled in the 2D surface phase diagram shown in Figure 6.9. The axes of the chemical potentials of Si and O were centered around the references discussed above using the following transformation:

$$\Delta\mu_{\mathrm{Si}} = \mu_{\mathrm{Si}} - E_{\mathrm{DFT}}^{\mathrm{Si}} \tag{6.3}$$

$$\Delta\mu_{\mathrm{O}} = \mu_{\mathrm{O}} - E_{\mathrm{DFT}}^{\mathrm{O\ atom}} - E_{\mathrm{Exp}}^{\mathrm{O_2\ atomization}}/2 \tag{6.4}$$

The color in the phase diagram corresponds to the most stable phase at any given pair of $\Delta\mu_{\mathrm{Si}}, \Delta\mu_{\mathrm{O}}$ while μ_{Ni} was fixed at the DFT total energy of bulk Ni per atom as described above. The experiments were done under ultrahigh vacuum (UHV) and high annealing temperature (∼1000 K), making the range of the oxygen chemical potential of interest negative, i.e., $\Delta\mu_{\mathrm{O}} < 0$. The values of $\Delta\mu_{\mathrm{O}}$ relevant to the typical experimental conditions (e.g., annealing temperature between 900 K and 1100 K and oxygen partial pressure between 4×10^{-8} Torr and 2×10^{-6} Torr) in this work ranges from –1.80 eV to –2.20 eV. Since zero valence Si was never experimentally observed, the regime of interest is $\Delta\mu_{\mathrm{Si}} < 0$. In fact, the Si AES peak remained consistent with SiO_2 in the lower oxygen pressure annealing experiments. Experimental conditions where 2D free-standing VDW bilayer silica can be stabilized over the Si and O atoms in the reservoir were also defined; thus, μ_{O} and μ_{Si} should obey:

$$\mu_{\mathrm{Si}} + 2\mu_{\mathrm{O}} > E_{\mathrm{DFT}}^{\mathrm{fs\ SiO_2}} \tag{6.5}$$

where $E_{\mathrm{DFT}}^{\mathrm{fs\ SiO_2}}$ is the DFT total energy of 2D free-standing VDW SiO_2 per Si atom. The region above the dashed line in Figure 6.9 corresponds to the combination of μ_{O} and μ_{Si}

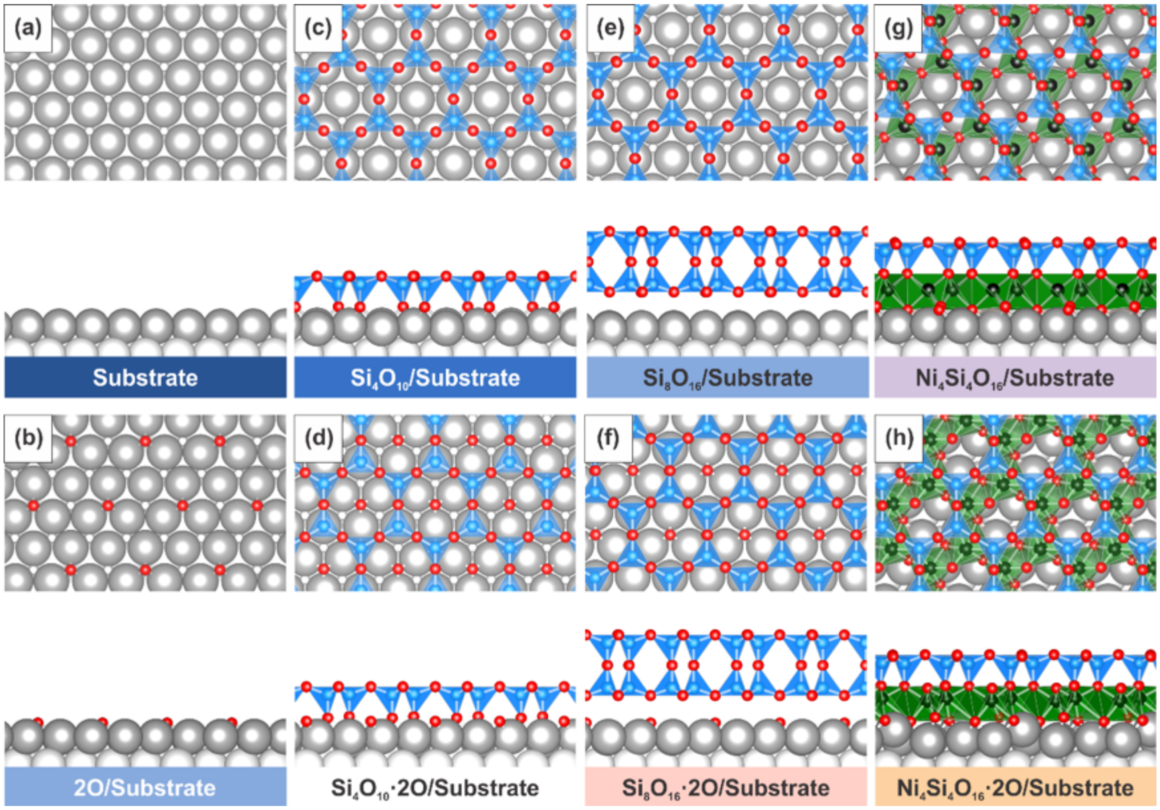

Figure 6.8: Atomic structures of 2D surface phases on the $Ni_{0.5}Pd_{0.5}$ alloy substrate (chemical formulae are defined per $(2 \times 2\sqrt{3})$ surface unit cell): (a) Substrate (clean surface), (b) 2O/Substrate (one chemisorbed oxygen on the hollow site), (c) Si_4O_{10}/Substrate (monolayer silica), (d) $Si_4O_{10}\cdot 2O$/Substrate (monolayer silica with one chemisorbed oxygen), (e) Si_8O_{16}/Substrate (bilayer silica), (f) $Si_8O_{16}\cdot 2O$/Substrate (bilayer silica with one chemisorbed oxygen), (g) $Ni_4Si_4O_{16}$/Substrate (Ni silicate), (h) $Ni_4Si_4O_{16}\cdot 2O$/Substrate (Ni silicate with one chemisorbed oxygen). Oxygen polyhedrons are drawn to emphasize the neighboring oxygen atoms surrounding the Si and Ni atoms in the 2D thin film. Color scheme: Si cyan, O red, Ni (in the overlayer) black, Ni (on the substrate surface) grey, $Ni_{0.5}Pd_{0.5}$ VCA atom white. Background color under each chemical formula corresponds to the color of region in the phase diagram in Figure 6.9.

that satisfies Eq. (6.5). All the constraints on μ_O and μ_Si discussed above define the experimentally accessible region in the phase diagram, shown as the area encompassed by the solid line in Figure (6.9). The main conclusion drawn from the phase diagram is that the thermodynamically stable phase on $\mathrm{Ni_{0.5}Pd_{0.5}}$ is either bilayer $\mathrm{SiO_2}$ with surface chemisorbed oxygen or Ni silicate, depending on the Si supply, i.e., a larger amount of Si favors 2D VDW silica phase more. However, the system might be kinetically trapped in other phases. This section concludes with pointing out another route to achieve 2D VDW silica on the surface. Other than just increasing the silicon supply, one can decrease $\Delta\mu_\mathrm{O}$ to –3.50 eV (by, for example, increasing the annealing temperature of the system to 1500 K while keeping the oxygen partial pressure at 4×10^{-8} Torr) where the Ni silicate can no longer be stable during the growing procedure.

6.6 Discussion

Growth on the single crystal, solid solution alloy substrate enabled the systematic experimental determination of how much strain could be imparted to an atomically thin 2D layer without appreciably changing the chemistry of the interfacial interactions. Despite chemical bonds between 2D Ni silicate and the alloy substrate, the results reveal that 2D Ni silicate overlayers can only be tensilely strained between 1.12 – 1.40% before the material relaxes to its favored lattice constant. This strain is actually less than the 2.1% tensile strain that Ru(0001) can impart to 2D silica bilayers despite much weaker VDW film-substrate interactions. Therefore, the overall strength of the film-substrate interaction cannot be the decisive factor in determining how much epitaxial strain can be applied to a 2D material. Rather the results highlight the importance of the 2D modulus of the layer, the energy penalty for incommensuration, and the accessibility of other phases that can relieve the strain; for 2D Ni silicate all three appear to limit the strain that can be applied. Regarding the 2D modulus, tetrahedral 2D bilayers can be relatively easily distorted by increasing tetrahedral bond angles, a low energy distortion which is limited by connections to the octahedrally coordinated Ni–O layer in 2D Ni silicate [71, 77, 168]. Meanwhile, prior theoretical study on the 2D Ni silicate structure revealed only a maximum 80 meV energy penalty to shift

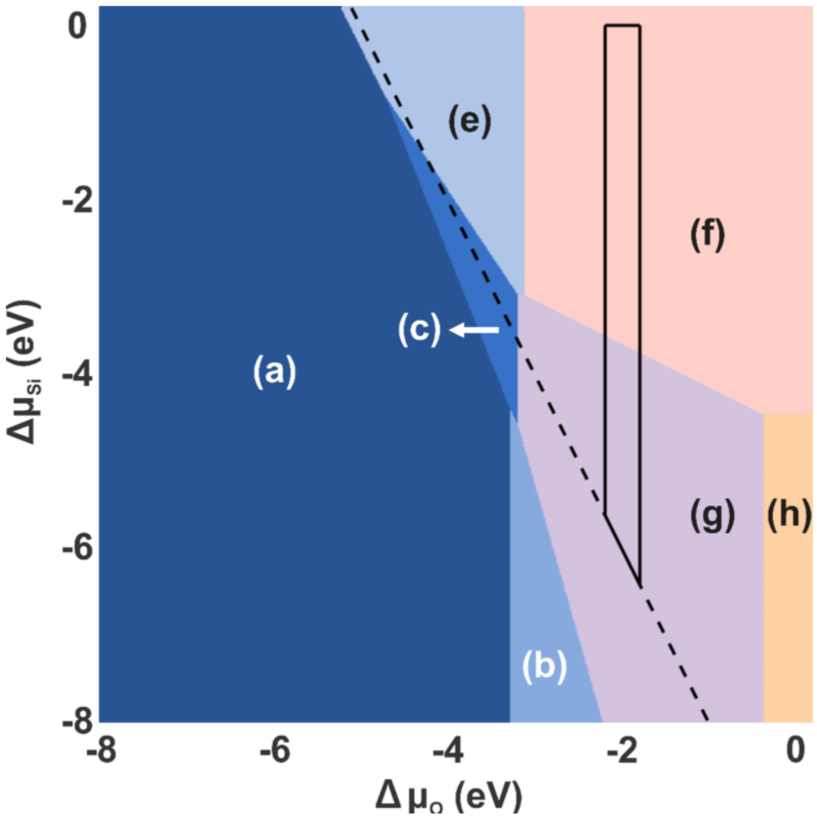

Figure 6.9: Phase diagram for the silica/silicate 2D surface phases on the $Ni_{0.5}Pd_{0.5}$ alloy substrate. Each colored region corresponds to the thermodynamically stable surface phase based on the surface free energy as a function of the Si and O chemical potentials. Letters denoting different phases follow the same notation as Figure 6.8. The bilayer silica can be stabilized above the blue dashed line on the surface. The experimentally accessible region of the chemical potentials in this study is inside of the blue solid line.

the silicate away from its favored registry with the substrate [2]. Finally, while SiO_2 can easily access a range of structures with varying ring sizes [77], the clay family to which 2D Ni silicate belongs are solely based on a sheet of six-membered rings or corner sharing SiO_4 tetrahedra.

A curious aspect of the results was that it was experimentally found that reducing the oxygen pressure during annealing could facilitate the formation of 2D VDW silica, but even at lower oxygen pressures the 2D VDW silica eventually completely converted to 2D Ni silicate. This is at odds with the expectations from the theoretical phase diagram which suggests that under the experimental conditions only 2D VDW silica should form, provided there is sufficient Si which the initial observation of 2D VDW silica suggests there clearly was. This apparent discrepancy may be due to limitations of the thermodynamic model. In particular, the model assumes a uniform surface that can freely exchange species with reservoirs of atoms. While this may accurately reflect the situation for oxygen, for silicon it is clearly not the case. Rather the surface contains a fixed amount of Si, the experimental conditions were limited to those where Si was not lost from the surface, with some degree of mobility at the high annealing temperatures. At the high temperatures, density fluctuations can lead to regions of locally low Si concentrations where the 2D Ni silicate is favored and will form and locally higher Si concentrations where bulk three-dimensional (3D) silica forms [71, 157], which was not included in the model. If either of these transformations is kinetically irreversible, then the 2D Ni silicate decorated by 3D silica clusters will eventually cover the entire surface.

The experimental and theoretical results point to a couple of directions to avoid Ni silicate formation. The first is to simply reduce the annealing time from minutes to seconds; unfortunately, the thermal mass of the sample assembly and limitations to the heater dictated relatively slow heating and cooling and thus at least minutes near the ultimate annealing temperature. As pointed out in the preceding section, a more robust way to avoid Ni silicate formation would be to reduce the oxygen chemical potential to the region where the Ni silicate is not favored regardless of the Si chemical potential. Although the dashed line in the phase diagram in Figure 6.9 suggests that these oxygen chemical potentials overlap regions where silica will not decompose, experiments suggest that this will be challenging as it was found that the lowest oxygen pressure at which Si remained at the surface at the relevant temperatures was 4×10^{-8} Torr. This discrepancy is likely due to theory only considering silica decomposition to Si and oxygen and not considering reduced Si oxides, Si dissolution into the bulk metal [169, 170], or the influence of reducing CO and H_2 typically found in UHV systems. Nonetheless, experiments at higher temperatures in a SiO flux that can replenish Si lost from the surface can potentially access this region of the phase diagram where Ni silicate formation can be avoided.

There are also curious aspects of the structures that form at lower oxygen partial pressures. First, only amorphous 2D VDW silica formed despite near zero lattice mismatch, apparently at odds with reports for Pt(111) and Pd(111) which suggested that large mismatch favors amorphous structures [70, 171]. Previous research, however, also highlight the roles of sample cooling rate after high-temperature annealing, the initial amount of silicon, and the oxygen partial pressure in determining crystallinity [89, 92, 159]. The results presented here indicate that these factors are at least as important as the lattice match in determining the competition between the crystalline and amorphous phases. Perhaps more interestingly, it was found that the 2D Ni silicate that formed at lower oxygen pressures where its formation proceeds at least in part through 2D VDW silica aligns differently with the substrate than 2D Ni silicate formed directly at higher oxygen partial pressures: the former is rotated 30 and is incommensurate while the latter is commensurate. This difference is likely due to a combination of a small driving force for commensuration and a different Ni silicate nucleation process at the different oxygen pressures. Regarding the former, the prior theoretical study on the 2D Ni silicate structure revealed that the energy cost of incommensuration is modest [2], consistent with the observed relaxation above just 1.12% tensile strain. Meanwhile, the initial silica deposition near room temperature produces a three-dimensionally disordered structure that is presumably defect rich. The annealing temperature is insufficient to melt bulk silica but apparently allows enough mobility to access lower energy states. At higher oxygen pressures, the results suggest that the 2D Ni silicate nucleates from the 3D disordered state which appears to allow sufficient fluidity, or reversibility of small cluster formation, to access the lower energy commensurate state (for small lattice mismatch). On the other hand, the 2D VDW bilayer silica structure removes all dangling bonds, reducing the system energy and presumably increasing the barrier to motion and bond rearrangement. As a result, nucleation of the Ni silicate from 2D VDW silica may be limited to weak points in the structure such as at large rings or crystalline domain boundaries with the consequence that the Ni silicate forms where it can with a high probability of incommensuration as opposed to sampling many sites in a more defective three-dimensionally disordered network. Finally, the incommensurate Ni silicate did not disappear after longer annealing times at a higher temperature, indicating that once it forms, it cannot convert back to 2D VDW silica or transit into the commensurate phase under the experimentally accessible conditions.

6.7 Summary

Combining STM, LEED, RAIRS, DFT, and ab initio thermodynamics, the competition between the formation of multiple 2D VDW silica and 2D Ni silicate phases on Ni-Pd solid solution alloy substrates was systematically investigated. While only 2D Ni silicate was observed under oxygen-rich conditions during high temperature annealing, suppressing the oxygen pressure during each film growth step suppressed silicate formation allowed amorphous 2D VDW silica to form. DFT was employed to explain the experimental findings from a thermodynamic perspective. The ab initio phase diagram highlighted the preference for 2D VDW silica under silicon-rich, oxygen-lean conditions. Despite the theoretical implication that a surface exposing only 2D VDW silica phase can be thermodynamically favored, the 2D VDW silica phase was found to eventually disproportionate into 3D SiO_2 and 2D Ni silicate at high temperatures. Theory suggests that the disproportionation reaction may be avoided by decreasing the oxygen chemical potential during annealing (through a combination of increasing the temperature and decreasing the oxygen pressure) while replenishing any silica lost from the surface. Varying the solid solution alloy substrate composition allowed the effect of strain on the structure of the 2D Ni silicate that formed to be studied without significantly changing the interfacial chemistry. A commensurate to incommensurate transition was observed 1.12% and 1.40% tensile mismatch, pinpointing the maximum epitaxial tensile strain within ±0.14%. The relaxation at relatively small strains despite the presence overlayer–substrate chemical bonds highlights the importance of the stiffness of the 2D layer and the driving force for commensuration in determining the maximum epitaxial strain rather than just the strength of the overlayer–substrate interaction. This research demonstrates several pathways to engineer the phase and structure of 2D silica and silicates that can be potentially employed to other 2D materials systems.

Chapter 7

Outlook

In this thesis, we have studied three solid state problems using first principles calculations: (i) the photoelastic responses of bulk insulators and semiconductors (Chapter 3), (ii) 2D SiO_2 on metal substrates (Chapter 4), and (iii) 2D Ni silicate on the Ni_xPd_{1-x} alloy substrate (Chapter 5 and 6). While much has been learned during these research efforts, there are more questions that can be answered. We conclude the thesis by describing possible future paths and further investigations for each project.

7.1 Photoelastic responses in solids

In this work, we have developed a method to calculate the dielectric and elasto-optic response of solids within the RPA using a Maximally Localized Wannier Function basis. We have revealed the relatively long-ranged nature for photoelasticity when described in real space using Wannier functions. The questions of whether the elasto-optic effect is intrinsically a relatively long-ranged phenomenon for all materials regardless of basis set (and whether an alternative *ab initio* real-space basis will compactify its description) remain open. However, at this point, an alternative choice of orthonormal real-space basis set (other than Maximally Localized Wannier Functions) that can make photoelastic response even localized in real space does not seem obvious. One might argue that since a non-orthonormal basis (e.g., non-orthogonalized atomic orbitals) allows for more locality in the basis set, the elasto-optic response in such a basis will be more localized. However, at present, our physical intuition argues against this: the fact that dipole transitions between third neighboring shells of atoms are non-negligible does not seem to be an artifact from the *degree* of locality of the atom or bond-centered Wannier orbitals used in this thesis. Future work can verify whether this intuition is correct or flawed.

In addition, some material-specific questions can be answered using methodologies developed in this work. For example, we may investigate the detailed differences between the first three shells of near-neighbored dipole transitions in NaCl and MgO that lead to their opposite photoelastic responses.

7.2 2D SiO_2 on metal substrates

Though the creation of 2D SiO_2 was originally intended to aid the study of 3D (bulk) zeolite materials, to the best of our knowledge, there has not been a quantitative comparison of the chemical properties between the two. We recommend starting such an investigation by comparing the binding of nitric oxide (NO) molecules to Co-exchanged silicates in both 2D and 3D forms using first principles simulations.

Nitric oxide (NO) reduction is an important chemical reaction in the treatment of diesel or power plant exhaust. Current industrial scale catalyst for this reaction uses Cu-exchanged zeolites which catalyze a reaction with ammonia to produce molecular nitrogen and water, i.e., $NO + NH_3 \longrightarrow N_2 + H_2O$. Another avenue for NO reduction is through reaction with methane, i.e., $NO + CH_4 \longrightarrow N_2 + CO_2 + H_2O$. The methane reaction is more economic than the one with ammonia because methane is much cheaper, but there is no suitable industrial scale catalyst to aid the NO reduction using methane. One promising candidate for such a catalyst is a Co-exchanged zeolite. We suggest a study the NO reduction on the Co-exchanged 2D silicate system to shed some light on the reaction mechanism of the same reaction in zeolites and potentially lead to improved industrial catalysis.

For the 3D zeolite case, one can consider the chabazite structure as a simple representative of the zeolite family [84]. For the 2D case, we can choose the hexagonal bilayer structure to mimic the chabazite's interior surface. This research project has two consecutive parts. First, one needs to determine the structure of the Co-exchanged 2D silicate by doping the 2D hexagonal bilayer silica. Catalytically active 2D silicates can be achieved by replacement of Si by Al atoms: two Al^{3+} replace two Si^{4+} and the charge deficit is met by adding one Co^{2+} to the system. Even the Löwenstein rule states that two Al cations cannot form a $\cdots$–Al–O–Al–$\cdots$ chemical bond linkage, there are remaining degrees of freedom in a search for possible patterns for Al insertion. We can use DFT to generate multiple Co-exchanged 2D silicate configurations with different Al insertions. They should be selected as candidates for the study of chemical binding, because, empirically, less stable (i.e., higher in energy) structures are usually more chemically reactive; hence structures with slightly higher energy than the ground state should be considered as well since they may bind NO molecules more strongly. Second, we can compute the binding energies of the NO molecules on different sites for the above generated set of candidate configurations under different conditions (with and without the presence of methane). We can then compare the results between 2D silicates and 3D zeolites. This should allow us to determine the extent to which 2D silicates imitate the chemical properties of 3D zeolites.

7.3 2D Ni Silicate on the Ni_xPd_{1-x} alloy substrate

The advantage of having a tunable lattice constant of the Ni_xPd_{1-x} alloy substrate for structural engineering of 2D silica is overshadowed by its ability to form Ni silicate thin films on the surface during the growth of 2D SiO_2. Though theoretical calculations suggest that increasing the quantity of deposited Si favors the 2D SiO_2 phase over the Ni silicate phase, experiments indicate the formation of Ni silicate is self-limited, i.e., once the nickel silicate is formed, continued exposure to oxidizing conditions does not alter its structure.

As a continued effort to grow 2D SiO_2 on alloy substrates, we propose the deposition of one monolayer equivalent amount of Ru atoms on the alloy to serve as a buffer layer between the Ni_xPd_{1-x} substrate and the deposited SiO_x. The Ru layer may aid the formation of 2D SiO_2 on the substrate since crystalline 2D SiO_2 is known to be able to form on Ru(0001). We can use first principles calculations to verify whether Ru atoms can be stabilized on the alloy substrate (instead of diffusing into the bulk) as well as the the energy barrier for Ru atom diffusion. We can collaborate with experiments to employ such system if the preliminary computational results show promise.

Bibliography

[1] J.-H. Jhang, C. Zhou, O. E. Dagdeviren, G. S. Hutchings, U. D. Schwarz, and E. I. Altman. Growth of two dimensional silica and aluminosilicate bilayers on Pd(111): from incommensurate to commensurate crystalline. *Physical Chemistry Chemical Physics*, 19(21):14001–14011, May 2017.

[2] C. Zhou, X. Liang, G. S. Hutchings, Z. S. Fishman, J.-H. Jhang, M. Li, U. D. Schwarz, S. Ismail-Beigi, and E. I. Altman. Structure of a Two-Dimensional Silicate Layer Formed by Reaction with an Alloy Substrate. *Chemistry of Materials*, January 2019.

[3] P. Hohenberg and W. Kohn. Inhomogeneous Electron Gas. *Physical Review*, 136(3B):B864–B871, November 1964.

[4] L. J. Sham and W. Kohn. Self-Consistent Equations Including Exchange and Correlation Effects. *Physical Review*, 140(4A):A1133–A1138, November 1965.

[5] J. F. Janak. Proof that $\frac{\partial E}{\partial n_i} = \epsilon$ in density-functional theory. *Physical Review B*, 18(12):7165–7168, December 1978.

[6] J. P. Perdew and A. Zunger. Self-interaction correction to density-functional approximations for many-electron systems. *Physical Review B*, 23(10):5048–5079, May 1981.

[7] J. P. Perdew and Y. Wang. Accurate and simple analytic representation of the electron-gas correlation energy. *Physical Review B*, 45(23):13244–13249, June 1992.

[8] D. M. Ceperley and B. J. Alder. Ground State of the Electron Gas by a Stochastic Method. *Physical Review Letters*, 45(7):566, 1980.

[9] R. O. Jones and O. Gunnarsson. The density functional formalism, its applications and prospects. *Reviews of Modern Physics*, 61(3):689–746, July 1989.

[10] L. J. Sham and M. Schlter. Density-Functional Theory of the Energy Gap. *Physical Review Letters*, 51(20):1888–1891, November 1983.

[11] J. P. Perdew and M. Levy. Physical Content of the Exact Kohn-Sham Orbital Energies: Band Gaps and Derivative Discontinuities. *Physical Review Letters*, 51(20):1884–1887, November 1983.

[12] J. P. Perdew and W. Yue. Accurate and simple density functional for the electronic exchange energy: Generalized gradient approximation. *Physical Review B*, 33(12):8800–8802, June 1986.

[13] J. P. Perdew, K. Burke, and M. Ernzerhof. Generalized Gradient Approximation Made Simple. *Physical Review Letters*, 77(18):3865–3868, October 1996.

[14] N. Troullier and J. L. Martins. Efficient pseudopotentials for plane-wave calculations. *Physical Review B*, 43(3):1993–2006, January 1991.

[15] A. M. Rappe, K. M. Rabe, E. Kaxiras, and J. D. Joannopoulos. Optimized pseudopotentials. *Physical Review B*, 41(2):1227–1230, January 1990.

[16] D. R. Hamann. Optimized norm-conserving Vanderbilt pseudopotentials. *Physical Review B*, 88(8):085117, August 2013.

[17] P. Giannozzi, S. Baroni, N. Bonini, M. Calandra, R. Car, C. Cavazzoni, Davide Ceresoli, G. L. Chiarotti, M. Cococcioni, I. Dabo, A. D. Corso, S. d. Gironcoli, S. Fabris, G. Fratesi, R. Gebauer, U. Gerstmann, C. Gougoussis, Anton Kokalj, M. Lazzeri, L. Martin-Samos, N. Marzari, F. Mauri, R. Mazzarello, Stefano Paolini, A. Pasquarello, L. Paulatto, C. Sbraccia, S. Scandolo, G. Sclauzero, A. P. Seitsonen, A. Smogunov, P. Umari, and R. M. Wentzcovitch. QUANTUM ESPRESSO: a modular and open-source software project for quantum simulations of materials. *Journal of Physics: Condensed Matter*, 21(39):395502, 2009.

[18] S. Baroni, S. de Gironcoli, A. Dal Corso, and P. Giannozzi. Phonons and related crystal properties from density-functional perturbation theory. *Reviews of Modern Physics*, 73(2):515–562, July 2001.

[19] N. Marzari and D. Vanderbilt. Maximally localized generalized Wannier functions for composite energy bands. *Physical Review B*, 56(20):12847–12865, November 1997.

[20] N. Marzari, A. A. Mostofi, J. R. Yates, I. Souza, and D. Vanderbilt. Maximally localized Wannier functions: Theory and applications. *Reviews of Modern Physics*, 84(4):1419–1475, October 2012.

[21] E. I. Blount. Formalisms of Band Theory. In F. Seitz and D. Turnbull, editors, *Solid State Physics*, volume 13, pages 305–373. Academic Press, January 1962.

[22] A. A. Mostofi, J. R. Yates, Y.-S. Lee, I. Souza, D. Vanderbilt, and N. Marzari. wannier90: A tool for obtaining maximally-localised Wannier functions. *Computer Physics Communications*, 178(9):685–699, May 2008.

[23] A. A. Mostofi, J. R. Yates, G. Pizzi, Y.-S. Lee, I. Souza, D. Vanderbilt, and N. Marzari. An updated version of wannier90: A tool for obtaining maximally-localised Wannier functions. *Computer Physics Communications*, 185(8):2309–2310, August 2014.

[24] C. Brouder, G. Panati, M. Calandra, C. Mourougane, and N. Marzari. Exponential Localization of Wannier Functions in Insulators. *Physical Review Letters*, 98(4):046402, January 2007.

[25] S. Ismail-Beigi and T. A. Arias. Locality of the Density Matrix in Metals, Semiconductors, and Insulators. *Physical Review Letters*, 82(10):2127–2130, March 1999.

[26] R. Resta. Macroscopic polarization in crystalline dielectrics: the geometric phase approach. *Reviews of Modern Physics*, 66(3):899–915, July 1994.

[27] I. Souza, N. Marzari, and D. Vanderbilt. Maximally localized Wannier functions for entangled energy bands. *Physical Review B*, 65(3):035109, December 2001.

[28] K. Berland, V. R. Cooper, K. Lee, E. Schrder, T. Thonhauser, P. Hyldgaard, and B. I. Lundqvist. van der Waals forces in density functional theory: a review of the vdW-DF method. *Reports on Progress in Physics*, 78(6):066501, May 2015.

[29] K. S. Novoselov, A. Mishchenko, A. Carvalho, and A. H. C. Neto. 2d materials and van der Waals heterostructures. *Science*, 353(6298):aac9439, July 2016.

[30] Y. Andersson, D. C. Langreth, and B. I. Lundqvist. van der Waals Interactions in Density-Functional Theory. *Physical Review Letters*, 76(1):102–105, January 1996.

[31] S. Grimme. Semiempirical GGA-type density functional constructed with a long-range dispersion correction. *Journal of Computational Chemistry*, 27(15):1787–1799, November 2006.

[32] A. Tkatchenko and M. Scheffler. Accurate Molecular Van Der Waals Interactions from Ground-State Electron Density and Free-Atom Reference Data. *Physical Review Letters*, 102(7):073005, February 2009.

[33] V. G. Ruiz, W. Liu, E. Zojer, M. Scheffler, and A. Tkatchenko. Density-Functional Theory with Screened van der Waals Interactions for the Modeling of Hybrid Inorganic-Organic Systems. *Physical Review Letters*, 108(14):146103, April 2012.

[34] H. G. Limberger, P. Fonjallaz, R. P. Salath, and F. Cochet. Compaction and photoelasticinduced index changes in fiber Bragg gratings. *Applied Physics Letters*, 68(22):3069–3071, May 1996.

[35] H. J. Peng, S. P. Wong, Y. W. Lai, X. H. Liu, H. P. Ho, and S. Zhao. Simplified system based on photoelastic modulation technique for low-level birefringence measurement. *Review of Scientific Instruments*, 74(11):4745–4749, October 2003.

[36] P. T. Rakich, P. Davids, and Z. Wang. Tailoring optical forces in waveguides through radiation pressure and electrostrictive forces. *Optics Express*, 18(14):14439–14453, July 2010.

[37] M. Li, W. H. P. Pernice, C. Xiong, T. Baehr-Jones, M. Hochberg, and H. X. Tang. Harnessing optical forces in integrated photonic circuits. *Nature*, 456(7221):480–484, November 2008.

[38] I. El-Kady, R. H. Olsson, and J. G. Fleming. Phononic band-gap crystals for radio frequency communications. *Applied Physics Letters*, 92(23):233504, June 2008.

[39] M. Eichenfield, R. Camacho, J. Chan, K. J. Vahala, and O. Painter. A picogram- and nanometre-scale photonic-crystal optomechanical cavity. *Nature*, 459(7246):550–555, May 2009.

[40] M. Eichenfield, C. P. Michael, R. Perahia, and O. Painter. Actuation of micro-optomechanical systems via cavity-enhanced optical dipole forces. *Nature Photonics*, 1(7):416–422, July 2007.

[41] J. Chan, M. Eichenfield, R. Camacho, and O. Painter. Optical and mechanical design of a zipper photonic crystal optomechanical cavity. *Optics Express*, 17(5):3802–3817, March 2009.

[42] A. Erba and R. Dovesi. Photoelasticity of crystals from theoretical simulations. *Physical Review B*, 88(4):045121, July 2013.

[43] Z. H. Levine, H. Zhong, S. Wei, D. C. Allan, and J. W. Wilkins. Strained silicon: A dielectric-response calculation. *Physical Review B*, 45(8):4131–4140, February 1992.

[44] J. E. Raynolds, Z. H. Levine, and J. W. Wilkins. Strain-induced birefringence in GaAs. *Physical Review B*, 51(16):10477–10488, April 1995.

[45] Z. H. Levine, J. H. Burnett, and E. L. Shirley. Photoelastic and elastic properties of the fluorite structure materials, LiF, and Si. *Physical Review B*, 68(15):155120, October 2003.

[46] D. Donadio, M. Bernasconi, and F. Tassone. Photoelasticity of crystalline and amorphous silica from first principles. *Physical Review B*, 68(13):134202, October 2003.

[47] D. Donadio, M. Bernasconi, and F. Tassone. Photoelasticity of sodium silicate glass from first principles. *Physical Review B*, 70(21):214205, December 2004.

[48] P. Damas, D. Marris-Morini, E. Cassan, and L. Vivien. Bond orbital description of the strain-induced second-order optical susceptibility in silicon. *Physical Review B*, 93(16):165208, April 2016.

[49] W. A. Harrison. Bond-Orbital Model and the Properties of Tetrahedrally Coordinated Solids. *Physical Review B*, 8(10):4487–4498, November 1973.

[50] T. S. Narasimhamurty. *Photoelastic and Electro-Optic Properties of Crystals*. Springer Science & Business Media, December 2012. Google-Books-ID: iCsLCAAAQBAJ.

[51] U. von Barth and C. D. Gelatt. Validity of the frozen-core approximation and pseudopotential theory for cohesive energy calculations. *Physical Review B*, 21(6):2222–2228, March 1980.

[52] A. D. Mighell and V. L. Karen. NIST Crystallographic Databases for Research and Analysis. *Journal of Research of the National Institute of Standards and Technology*, 101(3):273–280, 1996.

[53] S. Adler. Quantum Theory of the Dielectric Constant in Real Solids. *Physical Review*, 126(2):413–420, 1962.

[54] N. Wiser. Dielectric Constant with Local Field Effects Included. *Physical Review*, 129(1):62–69, 1963.

[55] D. K. Biegelsen. Photoelastic Tensor of Silicon and the Volume Dependence of the Average Gap. *Physical Review Letters*, 32(21):1196–1199, May 1974.

[56] H. R. Philipp and E. A. Taft. Optical Properties of Diamond in the Vacuum Ultraviolet. *Physical Review*, 127(1):159–161, July 1962.

[57] R. S. Leigh and B. Szigeti. Raman and photoelastic constants and impurity absorption in valency crystals. *Journal of Physics C: Solid State Physics*, 3(4):782, April 1970.

[58] K. G. Aggarwal and B. Szigeti. Photoelastic constants and the Clausius-Mossotti field in the alkali halides. *Journal of Physics C: Solid State Physics*, 3(5):1097–1111, May 1970.

[59] L. Benckert and G. Bckstrm. Determination of the Photoelastic Constants of NaCl, NaF, KCl, and KI by Means of Brillouin Scattering. *Physical Review B*, 8(12):5888–5893, December 1973.

[60] K. Vedam and E. D. D. Schmidt. Variation of Refractive Index of MgO with Pressure to 7 kbar. *Physical Review*, 146(2):548–554, June 1966.

[61] A. A. Giardini and E. Poindexter. Stress-Optical Behavior of Synthetic Periclase (MgO). *JOSA*, 48(8):556–557, August 1958.

[62] K. V. K. Rao and V. G. K. Murty. Photoelastic constants of magnesium oxide. *Acta Crystallographica*, 17(6):788–789, June 1964.

[63] F. Detraux and X. Gonze. Photoelasticity of -quartz from first principles. *Physical Review B*, 63(11):115118, March 2001.

[64] X. Ge and D. Lu. Local representation of the electronic dielectric response function. *Physical Review B*, 92(24):241107, December 2015.

[65] M. E. Lines. Bond-orbital theory of linear and nonlinear electronic response in ionic crystals. I. Linear response. *Physical Review B*, 41(6):3372–3382, February 1990.

[66] D. Geng and H. Y. Yang. Recent Advances in Growth of Novel 2d Materials: Beyond Graphene and Transition Metal Dichalcogenides. *Advanced Materials*, 30(45):1800865, 2018.

[67] K. S. Novoselov. Nobel Lecture: Graphene: Materials in the Flatland. *Reviews of Modern Physics*, 83(3):837–849, August 2011.

[68] R. Mas-Ballest, C. Gmez-Navarro, J. Gmez-Herrero, and F. Zamora. 2d materials: to graphene and beyond. *Nanoscale*, 3(1):20–30, 2011.

[69] C. Bchner and M. Heyde. Two-dimensional silica opens new perspectives. *Progress in Surface Science*, October 2017.

[70] X. Yu, B. Yang, J. Anibal Boscoboinik, S. Shaikhutdinov, and H.-J. Freund. Support effects on the atomic structure of ultrathin silica films on metals. *Applied Physics Letters*, 100(15):151608, April 2012.

[71] E. I. Altman, J. Gtzen, N. Samudrala, and U. D. Schwarz. Growth and Characterization of Crystalline Silica Films on Pd(100). *The Journal of Physical Chemistry C*, 117(49):26144–26155, December 2013.

[72] R. Wodarczyk, M. Sierka, J. Sauer, D. Lffler, J. J. Uhlrich, X. Yu, B. Yang, I. M. N. Groot, S. Shaikhutdinov, and H.-J. Freund. Tuning the electronic structure of ultrathin crystalline silica films on Ru(0001). *Physical Review B*, 85(8):085403, February 2012.

[73] B. Yang, W. E.Kaden, X. Yu, J. AnibalBoscoboinik, Y. Martynova, L. Lichtenstein, M. Heyde, M. Sterrer, R. Wodarczyk, M. Sierka, J. Sauer, S. Shaikhutdinov, and H.-J. Freund. Thin silica films on Ru(0001): monolayer, bilayer and three-dimensional networks of [SiO 4] tetrahedra. *Physical Chemistry Chemical Physics*, 14(32):11344–11351, 2012.

[74] D. Lffler, J. J. Uhlrich, M. Baron, B. Yang, X. Yu, L. Lichtenstein, L. Heinke, C. Bchner, M. Heyde, S. Shaikhutdinov, H.-J. Freund, R. Wodarczyk, M. Sierka, and J. Sauer. Growth and Structure of Crystalline Silica Sheet on Ru(0001). *Physical Review Letters*, 105(14):146104, September 2010.

[75] M. Heyde, S. Shaikhutdinov, and H. J. Freund. Two-dimensional silica: Crystalline and vitreous. *Chemical Physics Letters*, 550:1–7, October 2012.

[76] M. Wang, J.-Q. Zhong, J. Kestell, I. Waluyo, D. J. Stacchiola, J. A. Boscoboinik, and D. Lu. Energy Level Shifts at the Silica/Ru(0001) Heterojunction Driven by Surface and Interface Dipoles. *Topics in Catalysis*, pages 1–11, September 2016.

[77] A. Malashevich, S. Ismail-Beigi, and E. I. Altman. Directing the Structure of Two-Dimensional Silica and Silicates. *The Journal of Physical Chemistry C*, 120(47):26770–26781, December 2016.

[78] B. Yilmaz, U. Mller, B. Tijsebaert, D. D. Vos, B. Xie, F.-S. Xiao, H. Gies, W. Zhang, X. Bao, H. Imai, and T. Tatsumi. Al-RUB-41: a shape-selective zeolite catalyst from a layered silicate. *Chemical Communications*, 47(6):1812–1814, January 2011.

[79] K. Tanabe and W. F. Hlderich. Industrial application of solid acidbase catalysts. *Applied Catalysis A: General*, 181(2):399–434, May 1999.

[80] K. T. Thomson. Handbook of Zeolite Science and Technology Edited by Scott M. Auerbach (University of Massachusetts, Amherst), Kathleen A. Carrado (Argonne National Laboratory), Prabir K. Dutta (The Ohio State University). Marcel Dekker, Inc.: New York, Basel. 2003. xii + 1184 pp. $235.00. ISBN 0-8247-4020-3. *Journal of the American Chemical Society*, 126(28):8858–8859, July 2004.

[81] J. F. Haw. Zeolite acid strength and reaction mechanisms in catalysis. *Physical Chemistry Chemical Physics*, 4(22):5431–5441, November 2002.

[82] F. J. Giessibl. Advances in atomic force microscopy. *Reviews of Modern Physics*, 75(3):949–983, July 2003.

[83] W. A. Hofer, A. S. Foster, and A. L. Shluger. Theories of scanning probe microscopes at the atomic scale. *Reviews of Modern Physics*, 75(4):1287–1331, October 2003.

[84] I. Georgieva, L. Benco, D. Tunega, N. Trendafilova, J. Hafner, and H. Lischka. Multiple adsorption of NO on cobalt-exchanged chabazite, mordenite, and ferrierite zeolites: A periodic density functional theory study. *The Journal of Chemical Physics*, 131(5):054101, August 2009.

[85] E. Emmez, B. Yang, S. Shaikhutdinov, and H.-J. Freund. Permeation of a Single-Layer SiO2 Membrane and Chemistry in Confined Space. *The Journal of Physical Chemistry C*, 118(50):29034–29042, December 2014.

[86] T. Schroeder, M. Adelt, B. Richter, M. Naschitzki, M. Bumer, and H.-J. Freund. EPITAXIAL GROWTH OF SiO2 ON Mo(112). *Surface Review and Letters*, 07(01n02):7–14, February 2000.

[87] J. Weissenrieder, S. Kaya, J.-L. Lu, H.-J. Gao, S. Shaikhutdinov, H.-J. Freund, M. Sierka, T. K. Todorova, and J. Sauer. Atomic Structure of a Thin Silica Film on a Mo(112) Substrate: A Two-Dimensional Network of ${\mathrm{SiO}}_{4}$ Tetrahedra. *Physical Review Letters*, 95(7):076103, August 2005.

[88] T. Bjrkman, S. Kurasch, O. Lehtinen, J. Kotakoski, O. V. Yazyev, A. Srivastava, V. Skakalova, J. H. Smet, U. Kaiser, and A. V. Krasheninnikov. Defects in bilayer silica and graphene: common trends in diverse hexagonal two-dimensional systems. *Scientific Reports*, 3:3482, December 2013.

[89] L. Lichtenstein, M. Heyde, and H.-J. Freund. Crystalline-Vitreous Interface in Two Dimensional Silica. *Physical Review Letters*, 109(10):106101, September 2012.

[90] K. M. Burson, C. Bchner, M. Heyde, and H.-J. Freund. Assessing the amorphousness and periodicity of common domain boundaries in silica bilayers on Ru(0 0 0 1). *Journal of Physics: Condensed Matter*, 29(3):035002, 2017.

[91] L. Lichtenstein, C. Bchner, B. Yang, S. Shaikhutdinov, M. Heyde, M. Sierka, R. Wodarczyk, J. Sauer, and H.-J. Freund. The Atomic Structure of a Metal-Supported Vitreous Thin Silica Film. *Angewandte Chemie International Edition*, 51(2):404–407, January 2012.

[92] E. I. Altman and U. D. Schwarz. Structural and Electronic Heterogeneity of Two Dimensional Amorphous Silica Layers. *Advanced Materials Interfaces*, 1(7):1400108, 2014.

[93] G. S. Hutchings, J.-H. Jhang, C. Zhou, D. Hynek, U. D. Schwarz, and E. I. Altman. Epitaxial NixPd1x (111) Alloy Substrates with Continuously Tunable Lattice Constants for 2d Materials Growth. *ACS Applied Materials & Interfaces*, 9(12):11266–11271, March 2017.

[94] L. Bellaiche and D. Vanderbilt. Virtual crystal approximation revisited: Application to dielectric and piezoelectric properties of perovskites. *Physical Review B*, 61(12):7877–7882, March 2000.

[95] J. A. Boscoboinik, X. Yu, B. Yang, S. Shaikhutdinov, and H.-J. Freund. Building blocks of zeolites on an aluminosilicate ultra-thin film. *Microporous and Mesoporous Materials*, 165:158–162, January 2013.

[96] F. Gltl and J. Hafner. Structure and properties of metal-exchanged zeolites studied using gradient-corrected and hybrid functionals. I. Structure and energetics. *The Journal of Chemical Physics*, 136(6):064501, February 2012.

[97] R. B. Griffiths and W. Chou. Effective Potentials: A New Approach and New Results for One-Dimensional Systems with Competing Length Scales. *Physical Review Letters*, 56(18):1929–1931, May 1986.

[98] W. Chou and R. B. Griffiths. Ground states of one-dimensional systems using effective potentials. *Physical Review B*, 34(9):6219–6234, November 1986.

[99] G. Zheng and E. I. Altman. The oxidation of Pd(111). *Surface Science*, 462(1):151–168, August 2000.

[100] S. Lizzit, A. Baraldi, A. Groso, K. Reuter, M. V. Ganduglia-Pirovano, C. Stampfl, M. Scheffler, M. Stichler, C. Keller, W. Wurth, and D. Menzel. Surface core-level shifts of clean and oxygen-covered Ru(0001). *Physical Review B*, 63(20):205419, May 2001.

[101] C. Stampfl and M. Scheffler. Theoretical study of O adlayers on Ru(0001). *Physical Review B*, 54(4):2868–2872, July 1996.

[102] T. Narusawa, W. M. Gibson, and E. Trnqvist. Relaxation of Ni(111) Surface by Oxygen Adsorption. *Physical Review Letters*, 47(6):417–420, August 1981.

[103] S. Z. Butler, S. M. Hollen, L. Cao, Y. Cui, J. A. Gupta, H. R. Gutirrez, T. F. Heinz, S. S. Hong, J. Huang, A. F. Ismach, E. Johnston-Halperin, M. Kuno, V. V. Plashnitsa, R. D. Robinson, R. S. Ruoff, S. Salahuddin, J. Shan, L. Shi, M. G. Spencer,

M. Terrones, W. Windl, and J. E. Goldberger. Progress, Challenges, and Opportunities in Two-Dimensional Materials Beyond Graphene. *ACS Nano*, 7(4):2898–2926, April 2013.

[104] M. Xu, T. Liang, M. Shi, and H. Chen. Graphene-Like Two-Dimensional Materials. *Chemical Reviews*, 113(5):3766–3798, May 2013.

[105] G. R. Bhimanapati, Z. Lin, V. Meunier, Y. Jung, J. Cha, S. Das, D. Xiao, Y. Son, M. S. Strano, V. R. Cooper, L. Liang, S. G. Louie, E. Ringe, W. Zhou, S. S. Kim, R. R. Naik, B. G. Sumpter, H. Terrones, F. Xia, Y. Wang, J. Zhu, D. Akinwande, N. Alem, J. A. Schuller, R. E. Schaak, M. Terrones, and J. A. Robinson. Recent Advances in Two-Dimensional Materials beyond Graphene. *ACS Nano*, 9(12):11509–11539, December 2015.

[106] G. Zheng and E. I. Altman. The oxidation mechanism of Pd(100). *Surface Science*, 504:253–270, April 2002.

[107] F. P. Netzer and A. Fortunelli, editors. *Oxide Materials at the Two-Dimensional Limit*. Springer Series in Materials Science. Springer International Publishing, 2016.

[108] N. Doudin, D. Kuhness, M. Blatnik, F. P. Netzer, and S. Surnev. Phase behaviour of 2d MnWO x and FeWO x ternary oxide layers on Pd(1\hspace0.167em0\hspace0.167em0). *Journal of Physics: Condensed Matter*, 29(23):234004, May 2017.

[109] R. Wodarczyk, J. Sauer, X. Yu, J. A. Boscoboinik, B. Yang, S. Shaikhutdinov, and H.-J. Freund. Atomic Structure of an Ultrathin Fe-Silicate Film Grown on a Metal: AMonolayer of Clay? *Journal of the American Chemical Society*, 135(51):19222–19228, December 2013.

[110] F. D. Fischer, J. Sauer, X. Yu, J. A. Boscoboinik, S. Shaikhutdinov, and H.-J. Freund. Ultrathin Ti-Silicate Film on a Ru(0001) Surface. *The Journal of Physical Chemistry C*, 119(27):15443–15448, July 2015.

[111] C. Bchner, L. Lichtenstein, M. Heyde, and H.-J. Freund. The Atomic Structure of Two-Dimensional Silica. In S. Morita, F. J. Giessibl, E. Meyer, and R. Wiesendanger, editors, *Noncontact Atomic Force Microscopy: Volume 3*, NanoScience and Technology, pages 327–353. Springer International Publishing, Cham, 2015.

[112] S. Shaikhutdinov and H.-J. Freund. Ultra-thin silicate films on metals. *Journal of Physics: Condensed Matter*, 27(44):443001, October 2015.

[113] J. A. Boscoboinik, X. Yu, B. Yang, F. D. Fischer, R. Wodarczyk, M. Sierka, S. Shaikhutdinov, J. Sauer, and H.-J. Freund. Modeling Zeolites with Metal-Supported Two-Dimensional Aluminosilicate Films. *Angewandte Chemie International Edition*, 51(24):6005–6008, 2012.

[114] J. A. Boscoboinik, X. Yu, S. Shaikhutdinov, and H.-J. Freund. Preparation of an ordered ultra-thin aluminosilicate framework composed of hexagonal prisms forming a percolated network. *Microporous and Mesoporous Materials*, 189:91–96, May 2014.

[115] S. Wendt, E. Ozensoy, T. Wei, M. Frerichs, Y. Cai, M. S. Chen, and D. W. Goodman. Electronic and vibrational properties of ultrathin `$\mathrm{Si}{\mathrm{O}}_{2}$` films grown on Mo(112). *Physical Review B*, 72(11):115409, September 2005.

[116] T. K. Todorova, M. Sierka, J. Sauer, S. Kaya, J. Weissenrieder, J.-L. Lu, H.-J. Gao, S. Shaikhutdinov, and H.-J. Freund. Atomic structure of a thin silica film on a `$\mathrm{Mo}(112)$` substrate: A combined experimental and theoretical study. *Physical Review B*, 73(16):165414, April 2006.

[117] J. C. Vedrine. Isomorphous Substitution in Zeolitic Frameworks Procedures and Characterization. In P. A. Jacobs, N. I. Jaeger, L. Kubelkov, and B. Wichterlov, editors, *Studies in Surface Science and Catalysis*, volume 69 of *Zeolite Chemistry and Catalysis*, pages 25–42. Elsevier, January 1991.

[118] B. M. Weckhuysen, R. R. Rao, J. A. Martens, and R. A. Schoonheydt. Transition Metal Ions in Microporous Crystalline Aluminophosphates: Isomorphous Substitution. *European Journal of Inorganic Chemistry*, 1999(4):565–577, 1999.

[119] M. F. Brigatti, E. Galn, and B. K. G. Theng. Chapter 2 - Structure and Mineralogy of Clay Minerals. In F. Bergaya and G. Lagaly, editors, *Developments in Clay Science*, volume 5 of *Handbook of Clay Science*, pages 21–81. Elsevier, January 2013.

[120] H. Tissot, L. Li, S. Shaikhutdinov, and H.-J. Freund. Preparation and structure of Fe-containing aluminosilicate thin films. *Physical Chemistry Chemical Physics*, 18(36):25027–25035, 2016.

[121] J. W. Anthony. *Handbook of Mineralogy.* Mineral Data Publishing, 1995. Google-Books-ID: PEsSAQAAIAAJ.

[122] L. Li, H. Tissot, S. Shaikhutdinov, and H.-J. Freund. Transition Metal Induced Crystallization of Ultrathin Silica Films. *Chemistry of Materials*, 29(3):931–934, February 2017.

[123] M. Li and E. I. Altman. Formation and interaction of epitaxial Ge structures on Ge(001). *Physical Review B*, 66(11):115313, September 2002.

[124] C. Y. Nakakura, V. M. Phanse, G. Zheng, G. Bannon, E. I. Altman, and K. P. Lee. A high-speed variable-temperature ultrahigh vacuum scanning tunneling microscope. *Review of Scientific Instruments*, 69(9):3251–3258, September 1998.

[125] W. Gao, C. M. Wang, H. Q. Wang, V. E. Henrich, and E. I. Altman. Growth and surface structure of vanadium oxide on anatase (001). *Surface Science*, 559(2):201–213, June 2004.

[126] P. Giannozzi, O. Andreussi, T. Brumme, O. Bunau, M. B. Nardelli, M. Calandra, R. Car, C. Cavazzoni, D. Ceresoli, M. Cococcioni, N. Colonna, I. Carnimeo, A. D. Corso, S. d. Gironcoli, P. Delugas, R. A. DiStasio, A. Ferretti, A. Floris, G. Fratesi, G. Fugallo, R. Gebauer, U. Gerstmann, F. Giustino, T. Gorni, J. Jia, M. Kawamura, H.-Y. Ko, A. Kokalj, E. Kkbenli, M. Lazzeri, M. Marsili, N. Marzari, F. Mauri, N. L. Nguyen, H.-V. Nguyen, A. Otero-de-la Roza, L. Paulatto, S. Ponc, D. Rocca, R. Sabatini, B. Santra, M. Schlipf, A. P. Seitsonen, A. Smogunov, I. Timrov, T. Thonhauser, P. Umari, N. Vast, X. Wu, and S. Baroni. Advanced capabilities for mate-

rials modelling with Quantum ESPRESSO. *Journal of Physics: Condensed Matter*, 29(46):465901, October 2017.

[127] T. Schroeder, M. Adelt, B. Richter, M. Naschitzki, M. Bumer, and H. J. Freund. Growth of well-ordered silicon dioxide films on Mo(112). *Microelectronics Reliability*, 40(4):841–844, April 2000.

[128] Y.-N. Wen and J.-M. Zhang. Surface energy calculation of the fcc metals by using the MAEAM. *Solid State Communications*, 144(3):163–167, October 2007.

[129] A. Eichler, F. Mittendorfer, and J. Hafner. Precursor-mediated adsorption of oxygen on the (111) surfaces of platinum-group metals. *Physical Review B*, 62(7):4744–4755, August 2000.

[130] M. C. Biesinger, B. P. Payne, L. W. M. Lau, A. Gerson, and R. S. C. Smart. X-ray photoelectron spectroscopic chemical state quantification of mixed nickel metal, oxide and hydroxide systems. *Surface and Interface Analysis*, 41(4):324–332, 2009.

[131] M. C. Biesinger, B. P. Payne, A. P. Grosvenor, L. W. M. Lau, A. R. Gerson, and R. S. C. Smart. Resolving surface chemical states in XPS analysis of first row transition metals, oxides and hydroxides: Cr, Mn, Fe, Co and Ni. *Applied Surface Science*, 257(7):2717–2730, January 2011.

[132] A. P. Grosvenor, M. C. Biesinger, R. S. C. Smart, and N. S. McIntyre. New interpretations of XPS spectra of nickel metal and oxides. *Surface Science*, 600(9):1771–1779, May 2006.

[133] S. Hfner. Analysis of the core level satellites in XPS spectra of Ni dihalides. *Solid State Communications*, 49(12):1177–1179, March 1984.

[134] A. K. Geim and I. V. Grigorieva. Van der Waals heterostructures. *Nature*, 499(7459):419–425, July 2013.

[135] P. Bayliss. Unit cell data of serpentine group minerals. *Mineralogical Magazine*, 44(334):153–156, June 1981.

[136] Y. Song, H.-S. Moon, and H.-T. Chon. New occurrence and characterization of Ni-serpentines in the Kwangcheon area, Korea. *Clay Minerals*, 30(3):211–224, September 1995.

[137] A. T. N\textquotesingleDiaye, J. Coraux, T. N. Plasa, C. Busse, and T. Michely. Structure of epitaxial graphene on Ir(111). *New Journal of Physics*, 10(4):043033, April 2008.

[138] G. Ghosh, C. Kantner, and G. B. Olson. Thermodynamic modeling of the Pd-X (X=Ag, Co, Fe, Ni) systems. *Journal of Phase Equilibria*, 20(3):295, May 1999.

[139] K. Reuter and M. Scheffler. First-Principles Atomistic Thermodynamics for Oxidation Catalysis: Surface Phase Diagrams and Catalytically Interesting Regions. *Physical Review Letters*, 90(4):046103, January 2003.

[140] J. Tersoff and D. R. Hamann. Theory and Application for the Scanning Tunneling Microscope. *Physical Review Letters*, 50(25):1998–2001, June 1983.

[141] J. M. Blanco, F. Flores, and R. Prez. STM-theory: Image potential, chemistry and surface relaxation. *Progress in Surface Science*, 81(10):403–443, January 2006.

[142] X. Wang and F. Xia. Van der Waals heterostructures: Stacked 2d materials shed light. *Nature Materials*, 14(3):264–265, March 2015.

[143] S. Jin, M. Huang, Y. Kwon, L. Zhang, B.-W. Li, S. Oh, J. Dong, D. Luo, M. Biswal, B. V. Cunning, P. V. Bakharev, I. Moon, W. J. Yoo, D. C. Camacho-Mojica, Y.-J. Kim, S. H. Lee, B. Wang, W. K. Seong, M. Saxena, F. Ding, H.-J. Shin, and R. S. Ruoff. Colossal grain growth yields single-crystal metal foils by contact-free annealing. *Science*, 362(6418):1021–1025, November 2018.

[144] I. V. Vlassiouk, Y. Stehle, P. R. Pudasaini, R. R. Unocic, P. D. Rack, A. P. Baddorf, I. N. Ivanov, N. V. Lavrik, F. List, N. Gupta, K. V. Bets, B. I. Yakobson, and S. N. Smirnov. Evolutionary selection growth of two-dimensional materials on polycrystalline substrates. *Nature Materials*, 17(4):318, April 2018.

[145] A. Ambrosi, Z. Sofer, and M. Pumera. 2h 1t phase transition and hydrogen evolution activity of MoS2, MoSe2, WS2 and WSe2 strongly depends on the MX2 composition. *Chemical Communications*, 51(40):8450–8453, May 2015.

[146] H. H. Huang, X. Fan, D. J. Singh, H. Chen, Q. Jiang, and W. T. Zheng. Controlling phase transition for single-layer MTe2 (M = Mo and W): modulation of the potential barrier under strain. *Physical Chemistry Chemical Physics*, 18(5):4086–4094, January 2016.

[147] A. J. Mannix, B. Kiraly, M. C. Hersam, and N. P. Guisinger. Synthesis and chemistry of elemental 2d materials. *Nature Reviews Chemistry*, 1(2):0014, February 2017.

[148] S. Yang, F. Liu, C. Wu, and S. Yang. Tuning Surface Properties of Low Dimensional Materials via Strain Engineering. *Small*, 12(30):4028–4047, August 2016.

[149] M. Luo and S. Guo. Strain-controlled electrocatalysis on multimetallic nanomaterials. *Nature Reviews Materials*, 2(11):17059, November 2017.

[150] Z. Dai, L. Liu, and Z. Zhang. Strain Engineering of 2d Materials: Issues and Opportunities at the Interface. *Advanced Materials*, 0(0):1805417.

[151] P. Y. Huang, C. S. Ruiz-Vargas, A. M. van der Zande, W. S. Whitney, M. P. Levendorf, J. W. Kevek, S. Garg, J. S. Alden, C. J. Hustedt, Y. Zhu, J. Park, P. L. McEuen, and D. A. Muller. Grains and grain boundaries in single-layer graphene atomic patchwork quilts. *Nature*, 469(7330):389–392, January 2011.

[152] P. W. Sutter, J.-I. Flege, and E. A. Sutter. Epitaxial graphene on ruthenium. *Nature Materials*, 7(5):406–411, May 2008.

[153] J. Wintterlin and M. L. Bocquet. Graphene on metal surfaces. *Surface Science*, 603(10):1841–1852, June 2009.

[154] H. Terrones, M. Terrones, E. Hernndez, N. Grobert, J.-C. Charlier, and P. M. Ajayan. New Metallic Allotropes of Planar and Tubular Carbon. *Physical Review Letters*, 84(8):1716–1719, February 2000.

[155] Z. G. Fthenakis and N. N. Lathiotakis. Graphene allotropes under extreme uniaxial strain: an ab initio theoretical study. *Physical Chemistry Chemical Physics*, 17(25):16418–16427, June 2015.

[156] Y. Wang, A. J. Page, Y. Nishimoto, H.-J. Qian, K. Morokuma, and S. Irle. Template Effect in the Competition between Haeckelite and Graphene Growth on Ni(111): Quantum Chemical Molecular Dynamics Simulations. *Journal of the American Chemical Society*, 133(46):18837–18842, November 2011.

[157] S. Shaikhutdinov and H.-J. Freund. Ultrathin Silica Films on Metals: The Long and Winding Road to Understanding the Atomic Structure. *Advanced Materials*, 25(1):49–67, 2013.

[158] B. Yang, J. A. Boscoboinik, X. Yu, S. Shaikhutdinov, and H.-J. Freund. Patterned Defect Structures Predicted for Graphene Are Observed on Single-Layer Silica Films. *Nano Letters*, 13(9):4422–4427, September 2013.

[159] L. Lichtenstein, M. Heyde, and H.-J. Freund. Atomic Arrangement in Two-Dimensional Silica: From Crystalline to Vitreous Structures. *The Journal of Physical Chemistry C*, 116(38):20426–20432, September 2012.

[160] M. Chen and D. W. Goodman. The structure of monolayer SiO2 on Mo(112): A 2-D [SiOSi] network or isolated [SiO4] units? *Surface Science*, 600(19):L255–L259, October 2006.

[161] S. M. Auerbach, K. A. Carrado, and P. K. Dutta. *Handbook of Zeolite Science and Technology*. CRC Press, July 2003. Google-Books-ID: iIi08k1iF4gC.

[162] A. Nash and P. Nash. The NiPd (Nickel-Palladium) system. *Bulletin of Alloy Phase Diagrams*, 5(5):446–450, October 1984.

[163] K. Reuter and M. Scheffler. Composition, structure, and stability of ${\mathrm{RuO}}_{2}(110)$ as a function of oxygen pressure. *Physical Review B*, 65(3):035406, December 2001.

[164] J. Paier, R. Hirschl, M. Marsman, and G. Kresse. The PerdewBurkeErnzerhof exchange-correlation functional applied to the G2-1 test set using a plane-wave basis set. *The Journal of Chemical Physics*, 122(23):234102, June 2005.

[165] M. W. Chase. NIST-JANAF Thermochemical Tables, 4th Edition | NIST. *NIST-JANAF Thermochemical Tables 2 Volume-Set (Journal of Physical and Chemical Reference Data Monographs)*, August 1998.

[166] P. Y. Huang, S. Kurasch, A. Srivastava, V. Skakalova, J. Kotakoski, A. V. Krasheninnikov, R. Hovden, Q. Mao, J. C. Meyer, J. Smet, D. A. Muller, and U. Kaiser. Direct Imaging of a Two-Dimensional Silica Glass on Graphene. *Nano Letters*, 12(2):1081–1086, February 2012.

[167] T. Engel. The interaction of molecular and atomic oxygen with Si(100) and Si(111). *Surface Science Reports*, 18(4):93–144, January 1993.

[168] G. S. Hutchings and E. I. Altman. An atomically thin molecular aperture: two-dimensional gallium phosphate. *Nanoscale Horizons*, January 2019.

[169] S. D. Bader, L. Richter, and T. W. Orent. Auger-UPS study of intrinsic and Si-stabilized oxides of palladium. *Surface Science*, 115(3):501–512, March 1982.

[170] T. W. Orent and S. D. Bader. LEED and ELS study of the initial oxidation of Pd(100). *Surface Science*, 115(2):323–334, March 1982.

[171] H. Tissot, X. Weng, P. Schlexer, G. Pacchioni, S. Shaikhutdinov, and H.-J. Freund. Ultrathin silica films on Pd(111): Structure and adsorption properties. *Surface Science*, 678:118–123, December 2018.